Computational Approaches for the Analysis and Modelling of Filamentous Growth and Branching of *Streptomyces coelicolor*

Richard Leggett

Supervisors: Prof. Vincent Moulton
Dr. Gabriella Kelemen
Dr. Richard Morris

April 2010

School of Computing Sciences
University of East Anglia
Norwich, United Kingdom

Declaration

No portion of the work referred to in this thesis has been submitted in support of an application for another degree or qualification at this or any other university or other institute of learning.

Acknowledgements

I am very grateful to my supervisors, Prof Vincent Moulton, Dr Gabriella Kelemen and Dr Richard Morris for giving me the opportunity to study this fascinating area of science, for the time which they have devoted to my work and for their ongoing support and guidance throughout the research. I am also grateful to Dr Scott Grandison, who has been an important collaborator on the project and has been a regular source of ideas, encouragement and enthusiasm.

Thanks are due to Jim Hunter for the training and help he gave me as I began to learn basic microbiology lab skills, and also to Neil Holmes and Michael Gillespie for their subsequent assistance in the lab. I also thank Dr Stuart Cantlay and Dr Paul Thomas for their helpful microscopy advice.

I am grateful to the Norwich Research Park for providing my studentship, without which I would have been unable to undertake the research. I would also like to take this opportunity to thank the Schools of Computing Sciences and Biological Sciences at UEA, and the John Innes Centre, for the excellent facilities they have provided to allow me to carry out my work.

Finally, I would like to thank my wife, Rachel, and my parents, Trevor and Dorothy, for their constant support and encouragement.

Publications

Leggett, R.M., Grandison, S., Morris, R.J., Kelemen, G. and Moulton, V. (2009). Statistical analysis of the growth and morphology of the filamentous microbe Streptomyces coelicolor. In A. Gusnanto, K.V. Mardia and C.J. Fallaize (eds), *Statistical Tools for Challenges in Bioinformatics*, pp.107-110. Leeds, Leeds University Press.

Grandison, S., Leggett, R.M. and Morris, R.J. (2007). Measuring the elastomechanical properties of filamentous organisms with the calculus of variations In S. Barber, P.D. Baxter and K.V.Mardia (eds), *Systems Biology & Statistical Bioinformatics*, pp. 110-113. Leeds, Leeds University Press.

Kelemen, G.H., Walshaw, J., Thibessard, A., Holmes, N., Dalton, K.A., Leggett, R.M., Gillespie, M., Hemmings, A., Gust, B. and Hunter, J. (2010). Scy, a novel bacterial protein scaffold for polarised growth, tip architecture and hyphal geometry. *In preparation.*

Leggett, R.M., Grandison, S., Morris, R.J., Kelemen, G. and Moulton, V. (2010). A comparison of the early stage growth and morphology of *Streptomyces coelicolor* and three cytoskeletal mutants. *In preparation.*

Statement of Originality

I certify that this thesis, and the research to which it refers, are the product of my own work, and that any ideas or quotations from the work of other people, published or otherwise, are fully acknowledged.

Abstract

The bacterium *Streptomyces coelicolor* is a model organism which belongs to a family of bacteria known as Streptomycetes. It is fungal-like in appearance, composed of branching filamentous cells which produce reproductive spores on aerial branches. Streptomycetes are a particularly important family of bacteria because they are the source of a large proportion of natural antibiotics. Yet the type of growth exhibited by them is unusual in the bacterial world and the exact mechanisms are poorly understood.

In this thesis, we outline methods for the analysis and modelling of the early stage growth and morphology of *Streptomyces coelicolor* and three mutant strains which have been created by deactivation of the cytoskeletal genes, *filP* and *scy*. We provide an experimental technique suitable for growing bacteria for analysis and describe the development of a semi-automatic image analysis tool for gathering morphological statistics. Using this, we present a comprehensive analysis of the wild-type and mutant bacteria, highlighting differences between the strains.

We also introduce three new models of *S. coelicolor* growth and use these to help understand our experimental data and to suggest a mechanism which drives the extension of tips and initiation of new branches.

Contents

List of Figures

List of Tables

Chapter 1

Introduction

1.1 *Streptomyces coelicolor*

The bacterium *Streptomyces coelicolor* is a model organism which belongs to a family of bacteria known as Streptomycetes. It is fungal-like in appearance, composed of branching filamentous cells which produce reproductive spores on aerial branches. Streptomycetes are a particularly important family of bacteria because they are the source of a large proportion of natural antibiotics, as well as anti-cancer chemicals and industrially important enzymes.

Figure 1.1 shows a microscope image of early-stage *S. coelicolor* growth. In filamentous organisms such as *Streptomyces*, cells are arranged in hyphae - these are long filaments of cells divided by wall-like structures called septa (not visible in the figure) that form as the filament extends and its DNA is replicated. The septum forms a barrier between one cell and the next, but does not physically divide them in the same way as with organisms that replicate by binary division. Filaments grow only at the tips with growth nutrients carried along the hyphae to the growing ends. At points along the filament, a lateral branch may form and a new filament will begin growing outwards.

Though it is possible to observe the growth and morphology of *Streptomyces* using microscopy, there is currently not a good understanding of the mechanisms of tip extension, septation and branching. *Streptomyces* morphology exhibits a very similar appearance to that of many species of filamentous fungi, but the significant

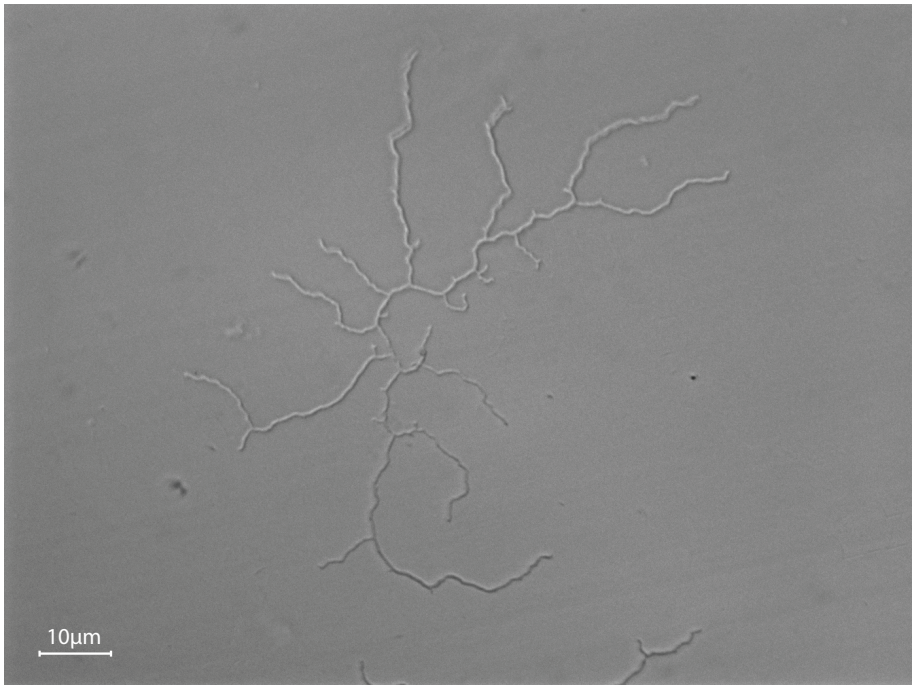

Figure 1.1: Example image of *Streptomyces coelicolor* growth. The bacterium is composed of long strands of branching filaments and growth occurs only at tips.

differences in internal structure between eukaryotic and prokaryotic cells mean that different processes are almost certainly at work.

1.2 Thesis scope

The work presented in this thesis has focussed on trying to gain a better understanding of the early stage growth and morphology of *S. coelicolor*, through experimental work, image processing, statistics gathering and mathematical modelling.

Our work has involved investigating four different strains of *S. coelicolor*: the wild-type, two single mutant strains with a single cytoskeletal gene deactivated, and a fourth double mutant strain with both genes deactivated. One of these genes, known as *scy*, was recently characterised by the Kelemen group at UEA and has been a particular focus of our research.

The experimental work has involved growing cultures of bacteria and taking thousands of microscope images of growth at various stages of development. We have used image processing techniques to develop a semi-automatic analysis tool, which has enabled us to provide a comprehensive quantitative description of the early-stage morphology of the bacteria, something that we believe to be unique.

The modelling work has enabled us to test a number of hypotheses related to the internal mechanisms of growth and branching and to see if these could explain the observed patterns of development. At all times, we have sought to tie together the experimental work with the modelling work and to use one to inform the other.

1.3 Structure of thesis

We now provide a brief overview of the thesis.

Chapter 2. We provide an introduction to the *Streptomyces* lifecycle and explain the current understanding of the processes of tip growth, septation, branching and growth direction. We discuss the similarities and differences to filamentous fungi.

Chapter 3. We describe the laboratory techniques which we developed to grow cultures of *S. coelicolor* suitable for morphological analysis. This includes details of the bacterial strains used, the preparation of growth media, the use of fluorescent staining, microscopy and the structure of the time series experiments carried out. Experiments were carried out using four different bacterial strains and two types of growth medium.

Chapter 4. We provide an overview of previous image processing work associated with filamentous microbes and then describe a number of techniques which we employed in the development of our own semi-automatic tool for the analysis of *Streptomyces* bacteria. We also provide a brief overview of the software structure, including a UML class diagram.

Chapter 5. We present the results of applying our analysis tool to a set of 2,200 images of growing *S. coelicolor* that we gathered using the techniques described in Chapter 3. These results are presented in a series of graphs and tables, which together highlight a number of significant morphological differences between the wild-type and the mutant strains. Understanding these differences provides insights into the function of the deactivated mutant genes.

Chapter 6. We begin with a review of existing models of filamentous growth in *Streptomyces*, as well as some relevant fungal models. We then outline three new models of *Streptomyces* growth that we have developed. The first is formulated as a set of ordinary differential equations which describe the balance of three types of hyphal element. The second model adopts an agent-based approach to provide a probabilistic, spatial, description of developing bacteria. Our final model uses a mechanistic description of the internal filament to describe tip extension and branch iniitation. The first and last models were developed with significant input from Dr. Scott Grandison, UEA.

Chapter 7. We summarise the work presented in this thesis and go on to discuss future directions for the work. These include early work in time-lapse imaging, enhancements to our analysis tool and future directions for development of our models.

Chapter 2

Biology of *Streptomyces*

2.1 Summary

In this chapter, we introduce some basic biology of *Streptomyces* and review current literature concerning growth and branching. The review mainly focuses on research related to the model organism *Streptomyces coelicolor*, which has been the object of our own analysis and modelling work.

Section 2.2 introduces the bacterium by providing a high-level view of its lifecycle from germination of a spore through to growth of vegetative and aerial mycelia and production of new spores. In the sections that follow, there is a more detailed study of the cytoskeleton, growth, branching, septation and growth direction. There is also some discussion of the biology of fungal species, as there are many similarities in the morphological characteristics of filamentous bacteria and fungi and some of the insights obtained from the study of fungi are also applicable to the study of *Streptomyces*.

2.2 The *Streptomyces* lifecycle

The genus *Streptomyces*, part of the Actinomycetes family of bacteria, are commonly occurring soil dwelling organisms. Fungal-like in appearance, they are composed of branching filamentous cells which produce reproductive spores on aerial branches. *Streptomyces* are particularly important bacteria because they are the source of a large proportion of medicinal antibiotics, as well as herbicides, antitumour agents

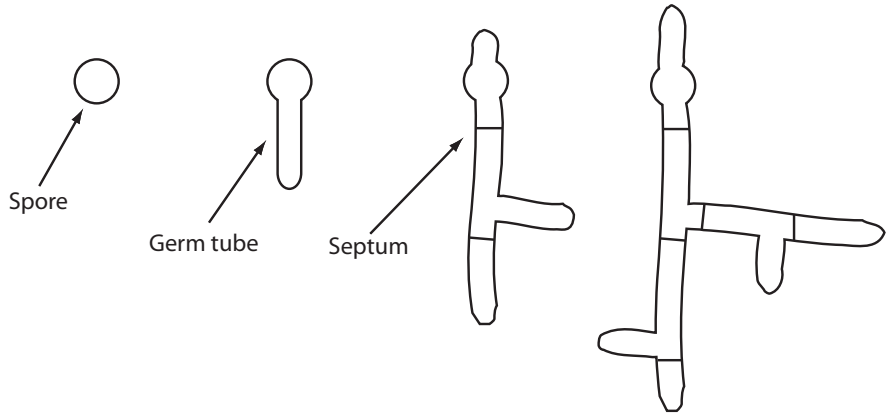

Figure 2.1: Vegetative growth of *Streptomyces*: Growth occurs only at the tips, while behind the tip the formation of occasional septa divides the mycelium into cell compartments. Periodically a branch may begin to form at a non-tip (sub-apical) cell.

and industrially important enzymes [37, 40].

Streptomyces cells are arranged in long filaments called hyphae. These cells are divided by septa and growth occurs only at the tips. Periodic branching results in the production of child filaments which emerge laterally to the parent filament. In most *Streptomyces*, branches only occur at sub-apical cells (that is, away from the tip), although in filamentous fungi and some mutant strains of *Streptomyces*, branching can also take place at the tip [26]. Although the tip extension rate is relatively constant, an exponential increase in the number of growing tips results in an exponential increase in overall biomass, at least in the early stages of colony growth [11].

The lifecycle of *Streptomyces* consists of a vegetative growth phase, involving colonisation of a substrate medium, followed by the growth of aerial mycelium and the production of antibiotics and new spores.

Figure 2.1 illustrates the vegetative growth of a typical *Streptomyces* bacterium. This begins with a spore, from which a single initial germ tube will emerge. Successive rounds of tip extension and septation follow, interspersed with occasional branching activity. Often, after a delay of a few hours, a second germ tube emerges in the opposite direction to the original one and growth then continues on both germ tubes. Some example microscope images of vegetative mycelia are provided in Figure 2.2.

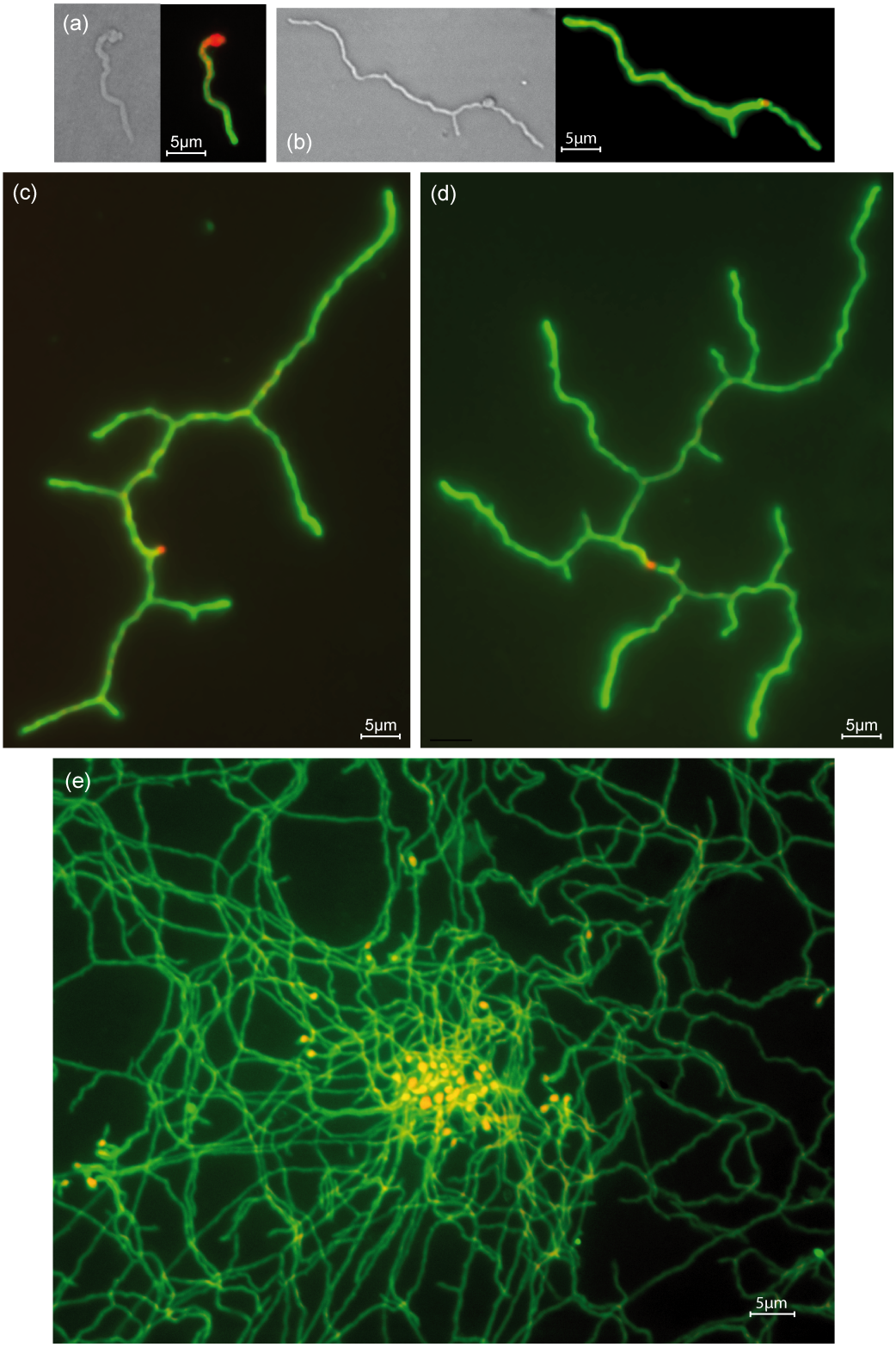

Figure 2.2: Microscope images of *Streptomyces coelicolor* vegetative mycelia, grown on minimal media and stained with Propidium Iodide (red) and Wheat Germ Agglutinin conjugate (green): (a) and (b) Phase contrast and fluorescence images taken 8-10 hours after incubation. (c) and (d) Florescence images taken 12-14 hours after incubation. (e) Eventually a mass of tangled filaments forms. Spores are shown as bright red dots.

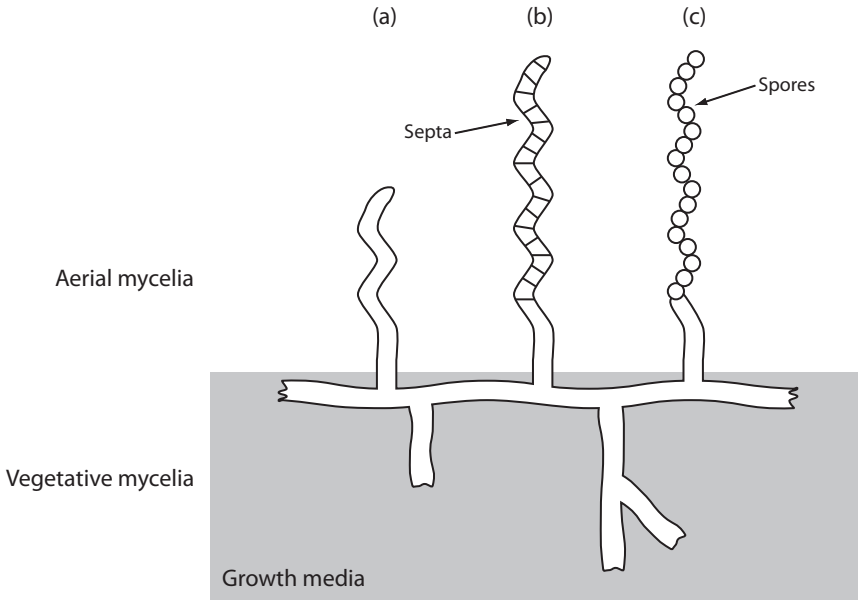

Figure 2.3: Aerial growth of *Streptomyces*: (a) Aerial mycelia begin to emerge perpendicular to plane of growth. (b) Synchronous septation generates the pre-spore compartments. (c) Spores chains are formed.

Nielsen states that in rich media, branching is highly favoured and the hyphal diameter is larger, while in poor media, branching is inhibited and the diameter is smaller [61]. This behaviour in poor media is thought to be because the mycelium extends itself in order to reach an environment better equipped to provide the nutrients needed for growth.

Eventually branching and septation cease completely in the centre of a colony and aerial mycelium may then form (Figures 2.3 and 2.4). This aerial growth phase is thought to be triggered by a sensitivity to nutrient depletion and possibly other signals [19]. At this point, curling aerial hyphae emerge perpendicular to the vegetative mycelia. These hyphae do not branch, but instead transition into chains of spores [74], which are dispersed further afield to begin reproduction at new sites. During this aerial growth phase, secondary metabolite production is initiated and results in the release of antibiotics and other chemicals. The production of antibiotics might have evolved as a defence mechanism against competing bacteria in the soil, and the fact that *Streptomyces* produces such a wide range of antibiotics is thought to be a reflection of its need to compete with a wide range of different bacteria [11].

If left to grow for long enough, eventually the colony originating from a single spore grows to a size visible by the naked eye and has a white, fluffy appearance as

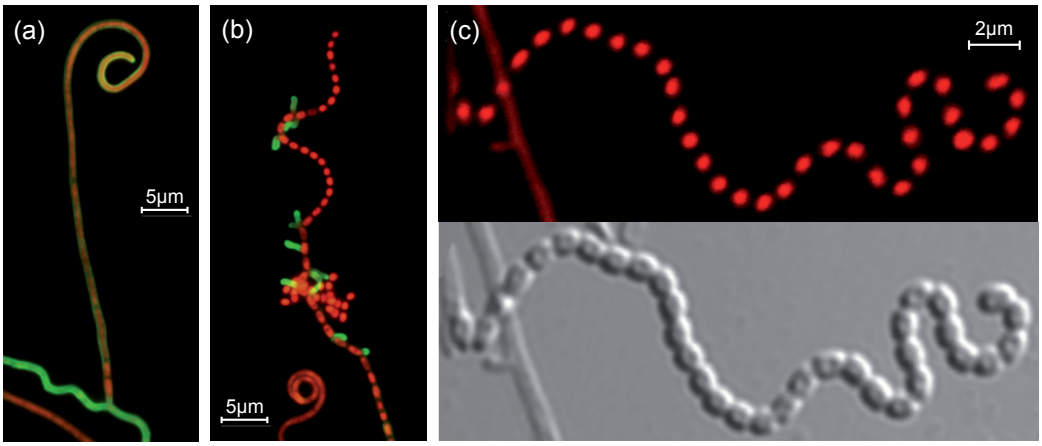

Figure 2.4: Example microscope images of *S. coelicolor* aerial hyphae, stained with Propidium Iodide (red) and Wheat Germ Agglutinin conjugate (green): (a) Curling aerial hypha before septation. (b) Aerial hypha after septation. (c) Spore chain. (Images provided by Neil Holmes and Gabriella Kelemen)

a result of the mass of aerial mycelium protruding from it (Figure 2.5). Later the colony turns grey in colour, indicating that production of mature spores is complete.

2.3 Similarities with filamentous fungi

Because of the very similar appearance and morphology of filamentous fungi to *Streptomyces* bacteria and the lack of knowledge of many of the internal bacterial mechanisms of extension and branching, it can be helpful to consider relevant fungal biology. Filamentous fungi are an order of magnitude larger than *Streptomyces* in terms of hyphal diameter and length. This makes them easier to image and perhaps explains why there is a greater volume of literature describing them. However, Goriely and Tabor point out that there are fundamental differences in the internal structure of fungi and actinomycetes [25].

Fungi are eukaryotic organisms (genetic material is held within a membrane-bound nucleus in the cell), while *Streptomyces* is a prokaryotic organism (genetic material is not membrane-bound). Fungi have a much more complicated internal structure which includes a cytoskeleton and organelles, while the cell wall structure is also different [25]. In fungi, it is thought that the cytoskeleton behaves as stress-bearing internal scaffolding [41]. Although it is now known than many prokaryotes possess a cytoskeleton, organelles are still thought to exist only in eukaryotes.

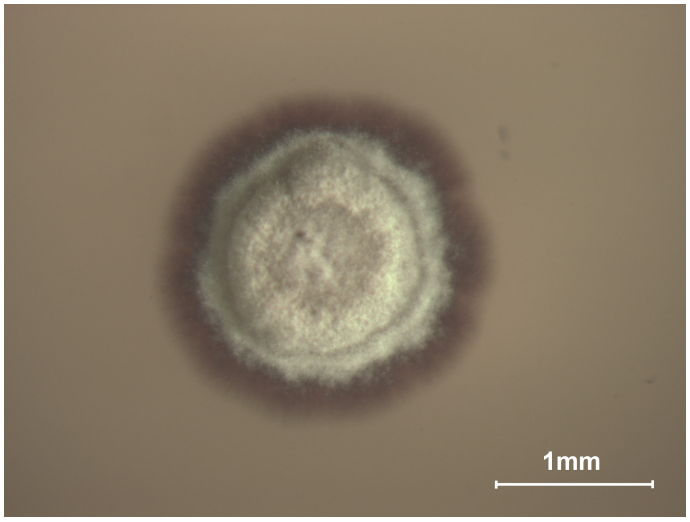

Figure 2.5: Image of a *S. coelicolor* colony after 6 days of growth on MMM media. (Image provided by Neil Holmes)

In fungi, vesicles are the organelles responsible for moving material for tip expansion around the hyphae. Vesicles accumulate at various points in the mycelium, often at the site of septa formation and at tips. The high concentration of vesicles found at the tip of a hypha is termed the Spitzenkörper. It is assumed that vesicles congregate at the Spitzenkörper prior to migrating to and fusing with the cell membrane to produce new cell wall surface [71]. To date, no Spitzenkörper has been observed in *Streptomyces*.

2.4 The genetics of *Streptomyces*

The genome of *S. coelicolor* was sequenced in 2002 and is 8,667,507 base pairs long, with 7,825 predicted protein encoding genes [6]. The production of 'knockout' mutants - bacteria with specific genes disabled - has been instrumental in understanding the genetics of *Streptomyces*. A common technique used to produce mutants is the PCR-targeting procedure [32] and is the method used for the experimental work presented in Chapter 3 of this thesis.

In the sections that follow, some mention is made of particular genes and associated proteins that have been found to be involved with tip growth and branching in *S. coelicolor*. We use the convention of writing gene symbols in italics with lower-case initial letter and proteins in upright text with first letter capitalised - for example *ftsZ* and FtsZ respectively.

2.5 The cytoskeleton

The cytoskeleton is the name given to a lattice of fibres which provide a supporting framework for the cell and help to maintain its shape. A range of cytoskeletal proteins have been identified in bacteria. FtsZ and MreB proteins are structurally and evolutionally related to the eukaryotic proteins tubulin and actin [4]. As is further discussed in Section 2.7, FtsZ is involved in marking the location of septa. MreB controls the shape of rod shaped bacteria such as *Escherichia coli* or *Bacillus subtilis* by generating helical scaffolds for cell wall synthesis. The function of MreB in *Streptomyces* is less clear, but is thought to be linked to the process of sporulation [54]. Growth of a mutant strain of *S. coelicolor* with the *mreB* gene deleted resulted in normal growth of vegetative mycelia, but many aerial hyphae had a swollen, irregular appearance and displayed lysis (cell death) [54].

Within *S. coelicolor*, the FilP protein has been identified as a key component in forming cytoskeletal structures [4]. Removal of the *filP* gene resulted in a distorted morphology and lower biomass when compared to the wild-type, while the use of atomic force microscopy (AFM) showed that the hyphae of *filP* knockout mutants were more deformable and softer than the wild-type [4]. Tip extension is marked by the landmark protein DivIVA [17], which we discuss further in the next section. DivIVA is an essential protein, which means that a knockout mutant of *divIVA* is not viable.

Recent work by Kelemen *et al.* has identified another *Streptomyces* cytoskeletal protein known as Scy [39], which seems to have an important role in the regulation of tip extension and branching and has been the focus of much of the research presented in this thesis.

2.6 Tip growth

A typical *Streptomyces* filament is less than 1 µm in diameter and can grow to lengths of 50-100 µm [25]. Kretschmer states that the extension rate of *S. granaticolor* tips increases exponentially during the first hours, synchronous with periodical rounds of DNA synthesis, and with the lengthening of the supporting hyphae [42]. It reaches a

maximum when the growth rate equals the rate of transport to the tips of nutrients needed for cell construction. Allan and Prosser measured the hyphal extension rate of *S. coelicolor* on solid minimal media to be 10-13 µm h^{-1} [2], while in liquid MEM media, Gray *et al.* found a hyphal extension rate of 8 µm h^{-1} [28].

Goriely *et al.* [24] describe the tip growth mechanism in *Streptomyces* as a complex process whereby wall building materials are incorporated into the tip as it is stretched by turgor pressure (intra-cellular fluid pressure). As the tip is stretched and built, the more distant parts of the hyphal element become rigid. The process by which wall building material and DNA is transported to the tip is unclear and the molecular basis of tip extension is also not well understood [18]. Due to the small diameter of hyphae, it is very difficult to make a detailed study of the internal mechanics of hyphal growth [28].

The bulk of the cell wall is composed of peptidoglycan, a polymer made from amino acids and sugars. Fluorescent conjugates of the antibiotic vancomycin can be used to visualise the location of peptidoglycan which has yet to be fully incorporated into the cell wall. This shows strong signals at hyphal tips and also at locations where lateral branches are about to form [14]. In earlier work, Gray *et al.* were able to label a peptidogyclan precursor known as GlcNAc and found it also localised to tips and, to a lesser extent, sites of lateral branching [28].

In contrast to tip extension, DNA replication appears to happen throughout the hyphal length. Kummer and Kretschmer treated *S. granaticolor* and *S. hygroscopicus* with a chemical which is incorporated exclusively into the DNA. They found no significant difference in the incorporation of the label up to a distance of 80 µm from the tip and concluded that all nucleoids had the same mean replication activity [46].

In *S.coelicolor*, the protein DivIVA has been found to be important in determining tip growth and hyphal shape [17]. DivIVA forms a focus at each growing tip and is found to be present at the site of lateral branches before the branch is visible [33]. Underexpression of the protein results in unusually curling hyphae and apical branching, while overexpression produced shorter, thicker hyphae with swollen ends [17] and increased branching sites [33]. Flärdh and Buttner suggest that DivIVA acts as a 'landmark protein' that recruits cell wall building machinery to its location

[19]. Hempel *et al.* concluded that DivIVA foci form preferentially at curved hyphal walls, after observing a preference for branches to appear on the outer side of bent or slightly curved hyphae. In their experiments, 68% of 120 observed branching events occurred on the outer convex side of curled hyphae [33].

In fungi, the Spitzenkörper is thought to operate as a Vesicle Supply Centre, regulating the supply of cell wall building material held in vesicles [69]. Robson reports that recent research with fungi has shown that tip extension is not strictly linear and may occur as a series of cyclic pulses [72].

In one of the few successful attempts at timelapse imaging of *Streptomyces*, Jyothikumar *et al.* observed the early development of 45 *S. coelicolor* spores [38]. Their experiments found spores formed one or two germ tubes, but never more - in contrast to the work of Noens *et al.* who found up to four germ tubes per spore [63]. Jyothikumar *et al.* found in 15-20% of germ tubes, that the growth of the primary germ tube ceased for a period of 1-5 hours when a lateral branch emerged. In the remaining 80-85% of germ tubes, the growth of the primary filament appeared to be unaffected by the emergence of the branch. The cases where primary germ tube growth was stunted appeared to be where branches happened relatively soon after the emergence of the germ tube. The means by which this pause in growth occurs is not known, but the authors suggest that one explanation is that hyphal extension requires the presence of a nucleoid close to the tip and so it is necessary for chromosome replication to take place before both tips posses an associated nucleioid and can extend.

2.7 Septation

Although not exhibiting the binary cell division often associated with bacteria, the process of septum formation in *Streptomyces* allows the discrimination of mycelial cell compartments. In vegetative mycelia, septa are formed relatively infrequently and tend to be formed far behind the tip. However, during sporulation in aerial mycelia, septa are far more closely spaced and the compartments they create become the spores which are dispersed in order for the organism to reproduce.

In vegetative mycelia, synthesis of new cell wall occurs only at tips, in the apical

compartment. However, it appears that DNA replication occurs in both apical and sub-apical compartments [40], perhaps leading to the formation of branches in the sub-apical compartments.

As has been found in many other types of bacteria, the tubulin-like FtsZ protein is implicated in septum formation in *S. coelicolor*. This forms so-called 'Z-rings' which mark the location of future septation activity and recruit additional proteins to the site [27]. The *ftsZ* gene does not seem to be essential for *Streptomyces* growth. Experiments involving bacteria with the gene removed still result in the growth of a colony, but no septation occurs and a single giant cell is formed [55]. However, because FtsZ is needed to produce cell divisions in aerial hyphae, no spore chains are produced and the bacteria is incapable of reproduction.

Kretschmer [43] examines the length and timing of septation during vegetative growth in *S. granaticolor*. Looking at the mean length of the apical and sub-apical cells (known as $c1$ and $c2$ respectively), the work found that decreased growth rates resulted in decreased mean length of both $c1$ and $c2$. Perhaps surprisingly, septum formation was found to be suppressed to a larger extent in richer media.

Examining the timing of septation, Kretschmer found that in fast growing cultures, the time between successive septations, T, was similar to C, the DNA replication time of the organism. The author concludes that septation timing is determined by the rhythm of DNA replication, if the apical cell has attained a certain length. Below this length, septation is suppressed and, even under optimal conditions, T is never less than C.

2.8 Branching

Kretschmer suggested that a build up of cell wall precursors beyond a point at which they can be used at the tip is what triggers branching [44]. Kretschmer also looked at the location of branches within the apical hyphal region of *Streptomyces granaticolor* and found that branches were not located at the midpoint between the tip and previous branch, but tended to be nearer the previous branch [45]. The distance from a newly formed branch to the tip changed from 12 to 44 μm, while from the new branch to the previous branch from 12 to 27 μm.

Riquelme and Bartnicki-Garcia have studied branching in the fungus *Neurospora crassa* using high resolution light microscopy [70]. Unlike in *Streptomyces*, apical branching does occur, although less commonly than lateral branching. The authors found the Spitzenkörper to be implicated in lateral branch formation, one being clearly visible at the site of each new branch. Lateral branches were found to have no significant disturbance on the growth rate of the parental tip, although the opposite was true with apical branching. The former observation, at least, supports the view that branching does not drain the resources needed to continue tip growth, but occurs because excess resources are available and cannot be efficiently transported to, and used by, the increasingly distant hyphal tip.

Prosser and Tough suggest that branching in fungi occurs at locations where there is an accumulation of vesicles, but that in prokaryotes (such as *Streptomyces*), branching is not related to an accumulation of vesicles [67]. In fungi, vesicles often accumulate at the point of septum formation, so branches are often positioned closed to septa. Kieser *et al.* [40] and Chater and Losick [11] both report that branch points are often close to septa, although neither provide experimental detail or provide an explanation for it. Yang *et al.* also report that experiments indicate *Streptomyces* branches are also often located near septa [85]. However, Prosser and Tough note that the branch closest to the tip is not usually located near a septum [67].

As noted in Section 2.6, DivIVA loci are observed at the sites of new branches in *S. coelicolor* [33].

2.9 Growth direction

There appears to be little published work on the factors determining growth direction in *Streptomyces*.

In fungi, growth direction appears to be determined by Spitzenkörper trajectory. This meanders slightly, but follows a broadly straight line. Riquelme *et al.* describe findings that point to the cytoskeleton being responsible for fixing Spitzenkörper trajectory and hence direction of the growing hypha [71]. By using antimicrotubular agents to attack the cytoskeleton, they were able to produce a marked disturbance in hyphal trajectory.

The hyphae of many fungi and *Streptomyces* bacteria can alter the direction of their growth or cease elongation [36], according to the presence of other hyphae. The avoidance mechanism is known as autotropism and may be due to either a localised reduction in oxygen around hyphae, a higher presence of carbon dioxide, or perhaps a secreted metabolite [72]. Allan and Prosser observed this phenomenon in *S.coelicolor*, stating that hyphae only rarely crossed over. In some media, they were able to observe tips extend until they almost touched another branch, at which point the tip would stop growing and a new branch would form [2].

2.10 Discussion

This chapter has provided an overview of the *Streptomyces* lifecycle and reviewed some of the current thinking of the processes involved in tip extension, septation and branching. A number of genes have been implicated in the regulation and control of hyphal extension and branching in vegetative mycelia and of particular importance are *divIVA*, *scy* and *filP*.

In the next chapter, we describe experiments we have carried out to grow cultures of wild-type *S. coelicolor* and of mutants created by knocking out the *scy* and *filP* genes.

Chapter 3

Experimental Work

3.1 Summary

This chapter describes the experimental work we carried out in order to gather data on the early stage growth and morphology of *Streptomyces coelicolor* and three mutant strains. The work involved growing samples of bacteria, fixing them, staining them and preparing slides for imaging with epifluorescent microscopy. In the following sections, we describe the evolution of our experimental method, the preparation of growth media, the preparation of spores and the microscopy methods used.

3.2 Bacterial strains

Table 3.1 details the four bacterial strains used in the experiments. These were the wild-type (also known as M145), a mutant with the *scy* gene deactivated (Δscy), a mutant with the *filP* gene deactivated ($\Delta filP$) and a double mutant with both *scy* and *filP* deactivated (Δscy-*filP*).

The PCR-targeting procedure, as described in [32], was used for generation of the knockout mutants. This involves combination of the bacterial DNA with a

Strain	Description	Reference or Source
M145	Wild-type SCP1$^-$ SCP2$^-$	Kieser *et al.* 2000 [40]
K111	Δscy (Δ28-1326aa)::*apr* derivative of M145	Kelemen *et al.* 2010 [39]
K113	$\Delta filP$::*apr* derivative of M145	Bagchi *et al.* 2008 [4]
K115	Δscy-*filP*::*apr* derivative of M145	Kelemen *et al.* 2010 [39]

Table 3.1: Bacterial strains used in the experiments.

cassette containing the apramycin resistance gene *aac(3)IV*, attached at either end by adapters designed to bind to the DNA sequence before and after the target gene. If this process is successful, then the cassette will replace the target gene. The successfully modified bacteria can then be identified by exposing to apramycin and selecting for resistance to it.

3.3 Growth media

A common method for growing bacteria in the laboratory is to use a Petri dish (referred to as a 'plate') containing a layer of solid agar-based growth medium onto which is spread a solution of spores.

There are a wide range of recipes for growth media, each containing different ratios of the sugars, salts and minerals which the bacteria requires for growth. Some media are described as minimal media, meaning that they have less of the nutritional components, while those described as complete media tend to have a much richer set of constituents.

For our main experiments, we used two media - Minimal Medium Mannitol (MMM) and Soya Flour Mannitol medium (SFM). As suggested by its name, MMM is not a very rich medium, while SFM is considered much richer. For spore counting experiments (Section 3.4) we also used Lennox Broth (LB) Agar medium, which is richer still than SFM. It is used for spore counting because it results in very rapid growth and produces colonies which are visible very quickly.

Each medium has to be made in the laboratory, but can be kept for a number of months before use. In order to prepare plates, the medium is melted in a microwave until completely liquid and homogeneous. It is then allowed to cool slightly before being poured into a plate to a depth of around 5 mm. The plates are left to cool and the media sets solid. Pouring of plates needs to be carried out under a laminar flow hood in order to prevent contamination with microbes present in the air.

Recipes used to create the media may be found in Appendix A. All are based on those described in [40].

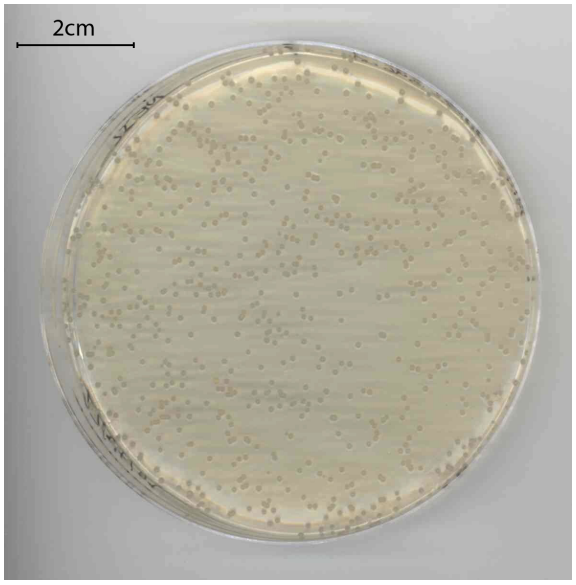

Figure 3.1: Photograph of plate used for spore counting experiments: Image taken after approximately 2 days of growth. The small dots are colonies, each grown from a single spore of *S. coelicolor*.

3.4 Preparation for growth

Suspensions of spores were provided by the Kelemen lab. These had previously been prepared according to the method described in [40]. The process involves scraping spores from a plate containing a fully grown culture of the appropriate strain, mixing with sterile water, centrifuging, vortexing (rapidly swirling the solution with a specially designed machine) and finally mixing with sterile 20% glycerol.

Spores were supplied as a concentrated spore stock suspended in glycerol. For use, these needed to be diluted to the desired concentration with sterile water. In order to calculate how much to dilute the stock for use in the main experimental work, it was necessary to perform some spore counting experiments.

Based on past experience, we made an initial approximate guess at the concentration of the stock and then worked out the ratios of water to spore stock required to dilute down to a few thousand spores per 100 µl. We produced a diluted spore solution at this ratio and also a further 10x and 100x dilution of that stock. We took 60 µl of each new spore solution, spread on a plate of LB media and incubated at 30℃. After 2-3 days, the spores grew into colonies that were visible to the naked eye (Figure 3.1). We were then able to count the number of colonies and, based on our dilution, calculate the original concentration of the spore stock.

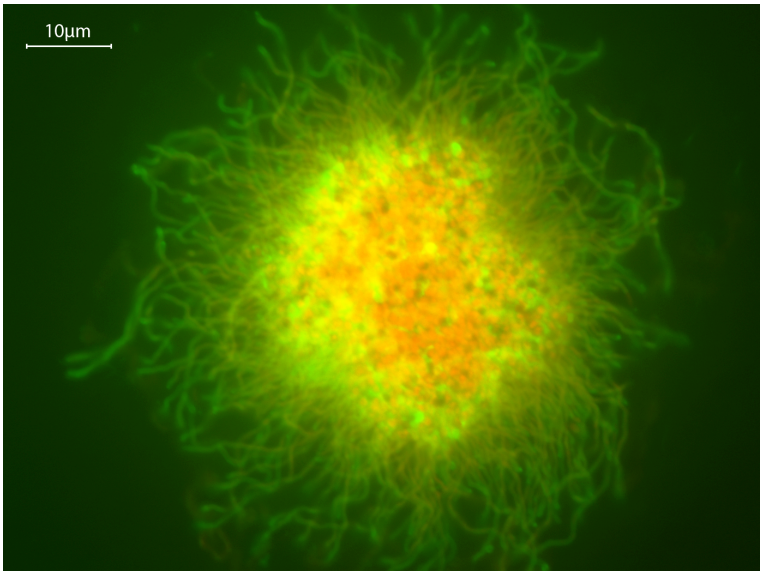

Figure 3.2: An example image of spore clumping: This can create beautiful images, but it is impossible to distinguish an individual spore's filament structure.

For the purposes of microscopy, we want something in the order of a few thousand spores per cm^2. This ensures that there are a large enough number of samples per microscope slide, but that the spores are sufficiently well spaced to avoid interfering with each other. With the results from the spore counting experiments, we were able to calculate the dilution required for the main experiments in order to produce the required spore density on the slide.

In an attempt to synchronise the spores, we heat shocked them. This involves placing the spore solution in a 50°C heat bath for 10 minutes, then placing it on ice [40]. This process is thought to cause the spores to 'reset' with the aim that the point of germination will be reasonably uniform across all spores in the solution.

The final stage of spore preparation involves ultrasound sonication. Initially we didn't carry this out, but we introduced it when we found that we were getting excessive clumping of spores. When spores clump, they stick together and produce a mass of hyphae which are indistinguishable from each other and from the originating spore (Figure 3.2). Sonication involves lowering a sterilised probe into the spore solution and emitting ultrasound for around 30 seconds. The vibration generated by the ultrasound waves causes the spores to shake apart in a more effective manner than vortexing alone does. At least in liquid media, ultrasound treatment is also thought to contribute to synchronicity [58]. Once sonicated, the spore solution must

be rapidly spread onto plates, before the spores have time to reagregate.

3.5 Static imaging

For static imaging, a bacterial culture is grown for a pre-determined time before a sample is taken and fixed to a microscope slide. The process of fixing (preserving and preventing further biochemical reactions) causes the bacteria to die and means that growth is frozen at that point in time. There are standard microbiology laboratory techniques for preparation and imaging of bacteria, but for reasons which we will explain in the following sections, we found it necessary to spend some time developing a method that suited our particular requirements. The requirements were:

- We wanted to encourage 2-dimensional growth of the *Streptomyces* bacteria, as this would allow us to more easily measure the morphological characteristics of the different strains.
- We needed bacteria to be reasonably well spaced, so that the growth from one spore did not interfere or overlap with the growth from another.
- We needed reasonably high contrast images with a strong profile of the bacterial cell wall, so that it was possible to produce software to carry out automatic image analysis.
- We needed the bacteria to be undisturbed, so that their morphology was unaffected by shocks or stresses.

In the sections that follow, we describe the evolution of our experimental technique, beginning with our first attempts at growing *Streptomyces* on microscope cover slips and leading on to the development of our final method.

With one notable exception, the techniques described make use of two fluorescent stains. The first, Propidium Iodide (PI), binds to DNA and appears red on fluorescent microscopy images. The second, a Wheat Germ Agglutinin (WGA) conjugate, binds to the bacterial cell wall, causing it to appear green under fluorescent microscopy. The particular WGA stain we used was AlexaFluor 488, supplied by Molecular Probes.

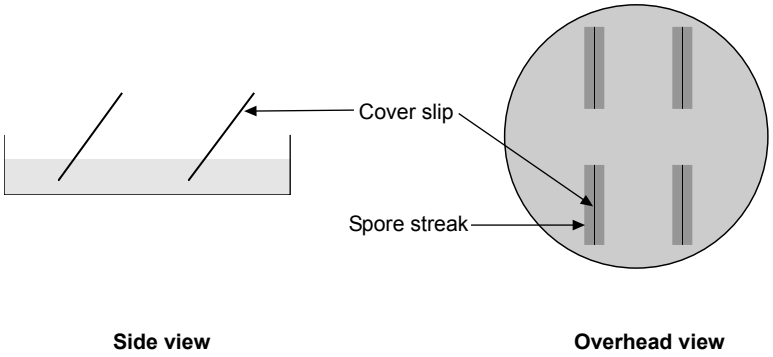

Figure 3.3: Growing *Streptomyces* on a cover slip: spores are streaked across the plate and cover slips inserted into the solid medium at an angle. Bacteria grow along the cover slip.

3.5.1 Growth on a cover slip inserted into media

A well established technique used for imaging *Streptomyces* involves growth on a cover slip inserted at an angle into a solid medium. Figure 3.3 illustrates the experimental setup. A Petri dish is filled with a solid medium such as MMM, which provides the energy source and nutrients needed for growth of the bacteria. Using a sterile tooth pick, an appropriately diluted spore solution is streaked in four lines across the plate. Where each line has been spread, a sterilised cover slip is inserted at an angle into the medium. This process is performed under a laminar flow hood in order to prevent contamination with other microbes.

The Petri dish is covered and placed in an incubator at 30℃. In our experiments, we tended to leave the sample overnight for a period between 10 and 20 hours before fixing. During that time, the spores germinate and the bacteria grow over the medium, including along the cover slip where it is in contact with the medium.

When the pre-determined growth time has elapsed, the plates are removed from the incubator. Each cover slip is carefully slid out of the medium and placed on a piece of paper. While bacterial growth may have occurred on both sides of the slip, it is normal practice to use the side facing toward the medium. A pipette is used to transfer 150 µl of methanol onto the cover slip to fix the bacteria. After waiting for a minute, the methanol is gently tipped off the cover slip. The bacteria are then covered with 30 µl of WGA/PI stain solution (diluted to 50µg/ml WGA conjugate, 25µg/ml PI), the slip is left in the dark (because the fluorescent dyes are sensitive to light) at room temperature for the stain to infuse. After 20-30 minutes, the cover

slip is gently washed in a beaker of water to remove excess stain, then dried as much as possible by tipping excess water off.

A microscope slide is prepared and a drop of 20% glycerol applied to the centre. The cover slip is placed, treated side downwards, onto the slide and the edges are sealed with nail polish. Once the nail polish has dried, the slide may be viewed under a microscope or stored at 4℃.

We found that the technique is capable of producing good quality, high contrast images of *Streptomyces* but we did encounter two significant problems:

- The images tend not to be particularly flat - that is, growth often occurs in 3-dimensions. This makes analysis difficult or impossible because the microscope has a limited depth of focus and the computational problems also increase enormously.

- The action of removing the cover slip from the medium is quite brutal and we can not be certain what damage is occurring to the bacteria during the process. The washing of the cover slip is also potentially traumatic for the bacteria.

These problems led us to consider an alternative method involving growth on cellophane.

3.5.2 An early technique for growth on cellophane

As with the cover slip procedure described in the previous section, a Petri dish is filled with a solid medium such as MMM. Once the medium has set, a thin sterile cellophane disc is taken, washed in sterile distilled water and laid on top of it. The cellophane discs need to be autoclaved prior to use to ensure they are sterile. This results in the cellophane drying and crinkling, so the washing is carried out to loosen them up and return them to their original condition. The damp cellophane clings to the surface of the medium and stays attached as it dries, though care must be taken not to dry it so much that it begins to curl away from the surface.

A spore solution is prepared according to Section 3.4. Once the cellophane surface is dry, the spore solution is spread over the cellophane using a glass spreading

tool or wet cotton bud. The plate is covered and placed in an incubator at 30℃ for a predefined period of time. As with the cover slip method, these initial stages need to be carried out under a laminar flow hood in order to prevent contamination from the air.

The cellophane is porous to the extent that it allows nutrients from the medium to pass through to the bacteria, but the pores are sufficiently small that the bacteria itself is unable to penetrate it. This forces bacterial growth to occur in largely 2-dimensions along the surface of the cellophane.

Once the growth period has elapsed, the plate is removed from the incubator. A razor blade is used to cut a small square of the cellophane (approximately 1.5 cm by 1.5 cm) which should contain a few thousand germinated spores. Using tweezers, the square is laid onto a piece of filter paper. A few drops of methanol are pipetted onto the cellophane to fix the bacteria. After a minute, tweezers are used to gently tip the excess methanol from the cellophane surface. A few drops of WGA/PI stain mixture are then pipetted onto the cellophane and it is covered and left for 20-30 minutes.

Once the stain has had sufficient time to infuse the bacteria, the cellophane is gently washed by dipping it into a beaker of sterile water. A microscope slide is prepared with a drop of 20% glycerol in its centre. The cellophane square is laid across the glycerol and another glycerol drop pipetted on top of it. Finally, a cover slip is pressed down over the cellophane and sealed with nail polish.

When we tried this technique, we found it resulted in much more 2-dimensional structures than with the original cover slip method. However, after some time, we began to notice unusual features in the hyphal structures. We realised that the bacteria seemed to be adhering much less well to the cellophane than to the glass. This means that as the stain was washed from the cellophane (a necessary part of the staining process), some bacteria would move or shear, thus disturbing their morphology.

We concluded that we needed to find a less brutal method of applying the stain to the bacteria. We explored the use of alternative stains which do not require washing and also alternative methods for applying and washing the stain.

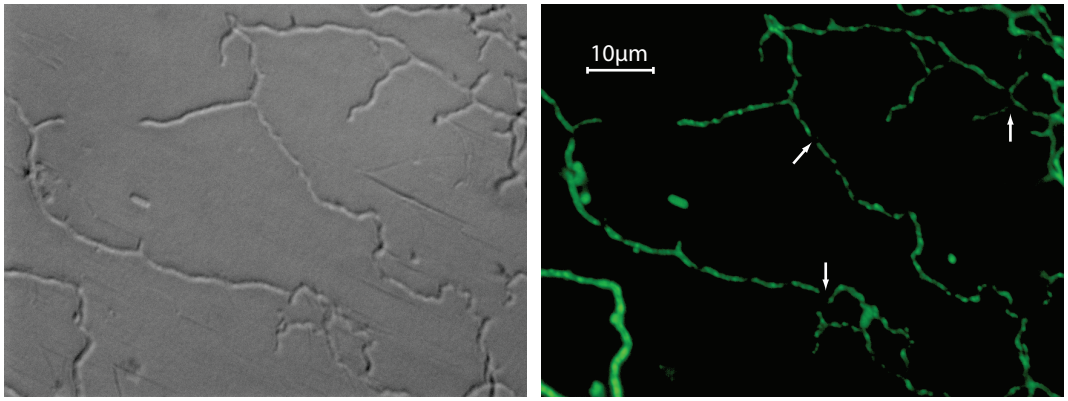

Figure 3.4: Example image showing staining with the AM1-43 stain: the left-hand image shows a DIC filter transmitted light image, while the right-hand image shows the AM1-43 fluorescence image of the same sample. Though clearly visible, the stain wasn't evenly distributed throughout the cell wall, with frequent discontinuities present (examples highlighted with arrows in the figure).

3.5.3 Use of alternative stains

There are stains available which do not require fixing or washing. We tried experimenting with two such stains - FM4-64 and AM1-43, from Molecular Probes range of lipophilic styryl stains. Using these stains, it is possible to remove the methanol fixing and beaker washing stages from the procedure outlined above.

When imaging samples stained with FM4-64 and AM1-43, we found the stain to be clearly visible, but not homogeneously distributed throughout the cell membrane (Figure 3.4). This caused significant problems for processing of the images, so we concluded that these stains did not provide the required solution to the problem.

3.5.4 An improved technique for cellophane growth

The technique we finally adopted is based on our early technique for cellophane growth, but with modifications to lessen the strain on the cellophane and bacteria. It is based on the idea of fixing, staining and washing from below, by laying the cellophane on small amounts of solution and allowing the solutions to permeate the membrane. Figure 3.5 illustrates the steps involved.

As with the earlier method, spores are grown on a cellophane disc laid on top of the medium and the spore solution is prepared according to the method described in Section 3.4. Once the spores have been allowed to germinate and grow for a fixed time period, a square of cellophane is cut with a razor blade. A piece of filter

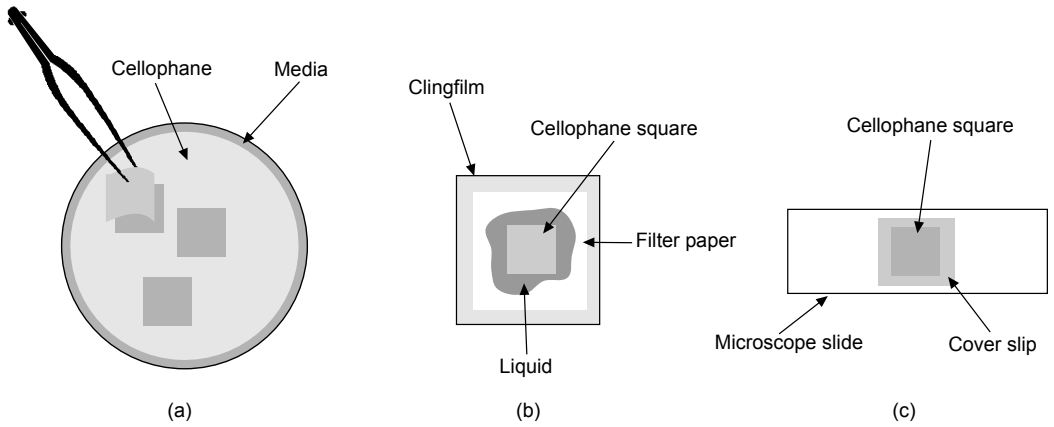

Figure 3.5: Growing *Streptomyces* on cellophane: (a) Having spread the spores on top of the cellophane and incubated, a square is cut and removed. (b) Fixing and staining is carried out by laying the cellophane onto infused filter paper. (c) The cellophane is mounted on a slide for viewing.

paper, slightly larger than the cellophane square, is cut and soaked with methanol from a pipette. The filter paper is placed on top of clingfilm to encourage retention of liquid. The square of cellophane is laid on top of the methanol soaked paper and allowed to rest for one minute. During this time, the methanol permeates the cellophane and produces fixing of the bacteria. Because the methanol evaporates relatively quickly, there is a danger of the cellophane drying out and curling. This is avoided if the cellophane is removed after a minute and laid on top of another piece of filter paper soaked in sterile water. Then, a pipette is used to transfer 15 µl of WGA/PI solution onto a microscope slide. The cellophane square is laid on top of this and covered while the solution permeates the cellophane and infuses the cells. As with previous methods, the solution is left for 20-30 minutes in the dark, but placed in a cold room to prevent the sample from drying out.

Washing of the stain solution is achieved using a piece of filter paper soaked in sterile water. Using tweezers, the cellophane square is lifted from the microscope slide and placed on the water soaked paper. It is covered and left for approximately a minute before lifting it up and placing it at a different site on the paper. This lifting and reseating process is repeated twice more.

A microscope slide is prepared with a drop of 20% glyercol in the centre. The washed cellophane is laid on top of the glycerol and another drop placed on top of the cellophane. A cover slip is pressed down, firmly but without shearing, and the edges sealed with nail polish.

When viewing samples prepared with this method, we found generally good results. Unlike with the early cellophane method, the bacteria seemed largely undisturbed by the process of fixing and washing. Good contrast was observed with epiflourescent microscopy, though it was not quite as good as the methods described in Sections 3.5.1 and 3.5.2 - perhaps because the washing is not sufficiently thorough to completely remove all surplus traces of the stain from the cellophane. However, overall this method provided the best balance of image quality and preservation of the bacterial morphology.

3.5.5 Microscopy

Obtaining clear, high quality, images of *Streptomyces* bacteria is not always a trivial task. This is largely due to their very small size, with diameters of no more than 1 µm. Fungal and plant cells are orders of magnitude larger, making it much easier to obtain good quality images.

We used a Zeiss Axio Imager widefield upright epiflourescent microscope with an attached AxioCam HR digital camera. This enabled us to use both transmitted light techniques and reflected light fluorescence techniques [10]. The microscope was fitted with both air-based and oil-based objectives. Oil-based objectives allow greater resolution and sharper images because light is transmitted through an immersion oil which has a higher refractive index than the air.

The microscope was equipped with a range of filters for transmitted light microscopy and we tried bright field (basic transmission microscopy), phase contrast filters (in which induced phase contrast shifts are used to increase contrast) and Differential Interference Contrast (DIC) optics (which use polarisation of light to give the impression of depth). We eventually settled on the use of a DIC filter, feeling it produced images that were clearest for human observers to discern. Though we did experiment with the use of image processing techniques on the transmitted light images, we quickly concluded that fluorescent imaging provided us with the clearest images for automatic processing (Chapter 4).

When undertaking fluorescent imaging, the microscope was set up to take a series of channel images - one transmitted light image, one green fluorescent image

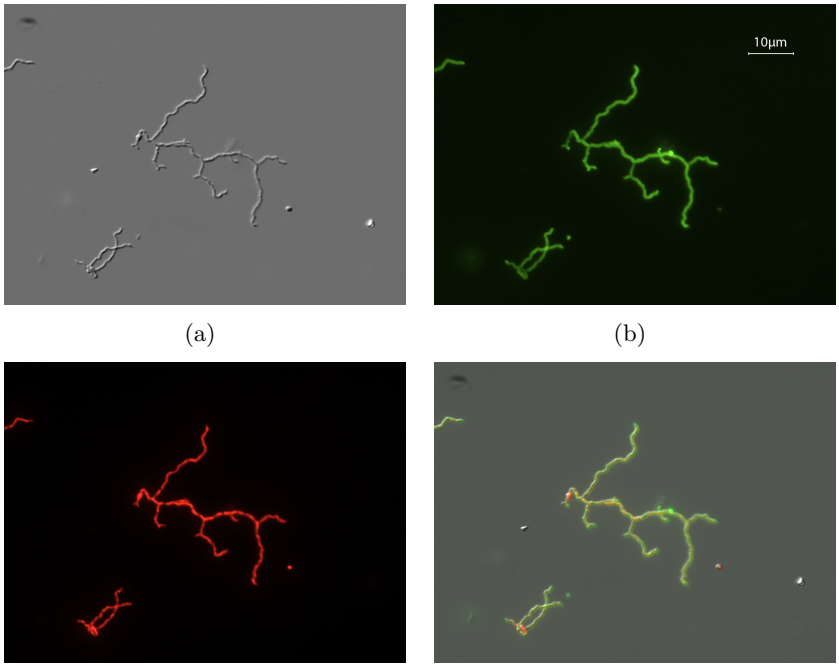

Figure 3.6: Example microscope images: (a) DIC filter (ordinary light) image. (b) WGA fluorescent image, showing cell wall profile. (c) PI fluorescent image, showing location of DNA. (d) Combined image.

(for WGA) and one red fluorescent image (for PI). It also produced a merged image containing an overlay of all the channel images. Figure 3.6 shows the channel and combined images for a typical specimen.

3.5.6 Time series experiments

In the absence of a mature method for carrying out live, real-time imaging (Section 7.2.1 describes our own early work on this), we carried out time-series experiments with the static imaging technique described above. In our time series experiments, we made slides at regular intervals and used these to understand how the organism developed over time.

In a typical experiment, we grew samples for up to 18 hours, making slides at two hour intervals from the sixth hour onwards. We choose the sixth hour as the start point because our own experimentation has shown that the initial germ tube only becomes visible at around 6-8 hours under the growth conditions that we used. We finished at around 18 hours, as by this time the filamentous structures were generally too complicated to differentiate.

We began by preparing seven plates and placing them all in an incubator. Six hours later, we took the first plate out and prepared three slides using the cellophane on the plate. One slide should contain enough samples, but we prepared three to allow for errors or inhomogeneity of the spreading. We repeated this process at two hourly intervals until 18 hours had elapsed.

3.6 Discussion

In this chapter, we have described the experimental approach we developed to enable good quality imaging of *S. coelicolor* morphological development. Conventional techniques for growth on glass cover slips enabled good quality images, but we found it hard to encourage 2-dimensional growth and found that young hyphae were easily disturbed when the cover slip was removed from the medium. Our method of growth on cellophane, combined with application of fixing and staining from below, enabled us to produce clear images of undisturbed bacteria.

We have also begun to investigate time lapse imaging, where we watch the development of a single bacterium over time. We will discuss this as possible future work in Chapter 7.

In the next chapter, we discuss the computational approaches used for semi-automatic analysis of microscope images of *S. coelicolor* grown with the cellophane techniques described in this chapter.

Chapter 4

Image Processing

4.1 Summary

In the previous chapter, we described the experimental work we carried out in order to capture microscope images of growing *Streptomyces*. These images were collected in order to carry out quantitative analysis of the bacteria's growth and morphology with a view to better characterising the wild-type and mutant strains. To analyse these images, we have developed a software tool, JFilamentAnalyser, to carry out semi-automatic analysis of filamentous microbes and to generate a wide range of biometrics and statistics.

This chapter begins with an overview of literature covering the application of image processing to filamentous microbes. We then move on to discuss our work, starting with an overview of the multi-stage process we developed to analyse the images that were captured during our experimental work. This is followed by sections detailing the theoretical and algorithmic basis of each stage in the process. The design and use of JFilamentAnalyser is then briefly discussed, with further detail contained in Appendix C.

4.2 Background literature

A number of reviews have been published which examine the use of image analysis in the study of filamentous organisms [13, 66, 80, 65]. Cox *et al.* [13] divide techniques into those that work on freely dispersed morphologies (those with no tip overlap),

dispersed morphologies (formed as hyphae becoming more packed with some overlap) and pellet morphologies (where there is much overlap of hyphae). Because of the use of filamentous microbes in industry, there is a lot of interest in categorising and analysing pellet morphologies in submerged cultures [56, 65, 83]. However, our own work has focused on the analysis of young bacteria which display freely dispersed morphologies.

Some of the earliest work studying freely dispersed morphologies was that of Adams and Thomas [1], who used an 8-bit microcomputer connected to a Hewlett Packard digitiser and a Magiscan image analyser. The hardware carried out image capture and segmentation (separation of hyphae from background), after which a human operator edited the images to remove artefacts and identified branches using a light pen. Software then calculated the length of filaments using the branch point information provided by the user.

The work of Reichl *et al.* [68] used similar techniques to Adams and Thomas in the study of early growth and branching of *Streptomyces tendae*. Their main improvement was to implement a method of automatic identification of branching sites, though there was still a degree of user interaction required in confirming the software's analysis. Reichl *et al.*, as well as Adams and Thomas before them, suffered from the technological limitations of the day which meant low resolution images and, despite using dedicated image processing hardware, processing times of up to 15 minutes per hyphal structure.

Later work by Drouin *et al.* [15] and Pons *et al.* [66] used image processing techniques on cultures of *S. ambofaciens*. Their particular focus was on identifying full and empty hyphal zones and quantifying the location of septa. Special stains were required to highlight these features, along with software which carried out a number of rounds of segmentation and skeletonization (thinning of structures).

Despite some of this early work, there are no freely available tools designed for the morphological analysis of filamentous bacteria. The software supplied with microscopes typically provides basic colour adjustment functionality and the ability to manually measure distances and areas, but such tools are inadequate for a detailed quantitative analysis. In the sections that follow, we describe the system we

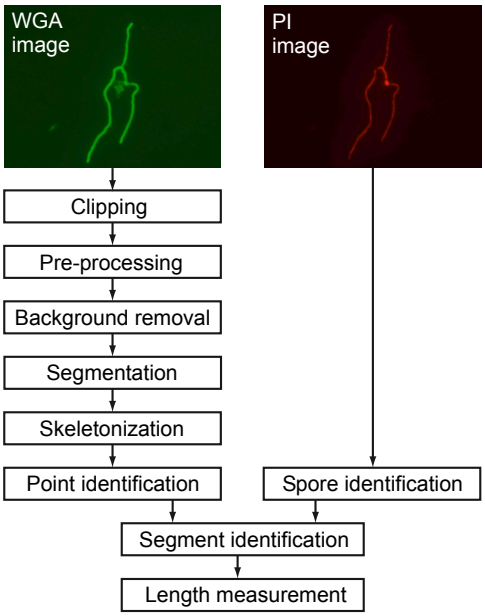

Figure 4.1: Diagram showing the steps involved in processing images and extracting morphological data. The inputs to the process are the two channel images - the green WGA image and the red PI image.

developed for the morphological analysis of *S. coelicolor*. Like much of the previous work, segmentation and skeletonization algorithms are key. In addition, we have implemented a number of other image processing and morphological analysis steps with the aim of creating a far more accurate and comprehensive analysis tool.

4.3 Overview of image processing steps

Our aim is to apply image processing and feature detection techniques to automatically extract morphological data from images of *S. coelicolor* obtained through static microscopy.

We have developed a multi-stage process for the extraction of morphological data (Figure 4.1). The process begins with the WGA channel (green fluorescence) image which provides good contrast between filament wall and background (Section 3.5). The image is clipped and pre-processed and a segmentation algorithm is used to separate the hyphal mass from the background. Because microscope images are not always uniformly illuminated, a background removal algorithm is applied before segmentation. After segmentation, a skeletonization algorithm is applied to the image in order to thin the hyphae to single pixel widths.

With a skeletonized hyphal image, it is possible to locate tip points and branch points and to measure distances between them along the skeleton. The final piece of information required is the location of the originating spore. Because the spore contains a high concentration of DNA, it can be located from the PI channel image where it appears as a small bright oval shape.

Once all key points have been identified and distances between them measured, it is possible to calculate a wide range of biometrics and statistics about the organism's morphology, which we shall describe in Section 4.4.

4.3.1 Pre-processing

Prior to segmentation, some pre-processing is performed on the images. This involves cropping to ensure that each image contains only one hyphal structure, as well as the application of a filter to smooth the image and reduce noise. Common filters for such a task are the mean, median and Gaussian filters [23, 76]. The mean and median filters replace a pixel's intensity with the mean or median intensity of the pixels in the 8-neighbourhoud, while the Gaussian filter weights the neighbouring pixels according to a 2-dimensional Gaussian distribution.

4.3.2 Segmentation

Segmentation is the name given to the process of identifying the constituent parts of an image. We wish to identify the hyphae and to remove any parts of the image that are not hyphae. This includes the image background, noise and any physical artefacts.

With good contrast microscope images, relatively simple segmentation methods can be applied with good results. A grey-level threshold segmentation works by accepting all pixels that fall above a particular threshold intensity, whilst excluding all others. Those below the threshold are assigned a value of zero in the segmented image. Those pixels with intensity above the threshold are assigned a value of one in the segmented image. So for an image f, represented by an m-by-n matrix of

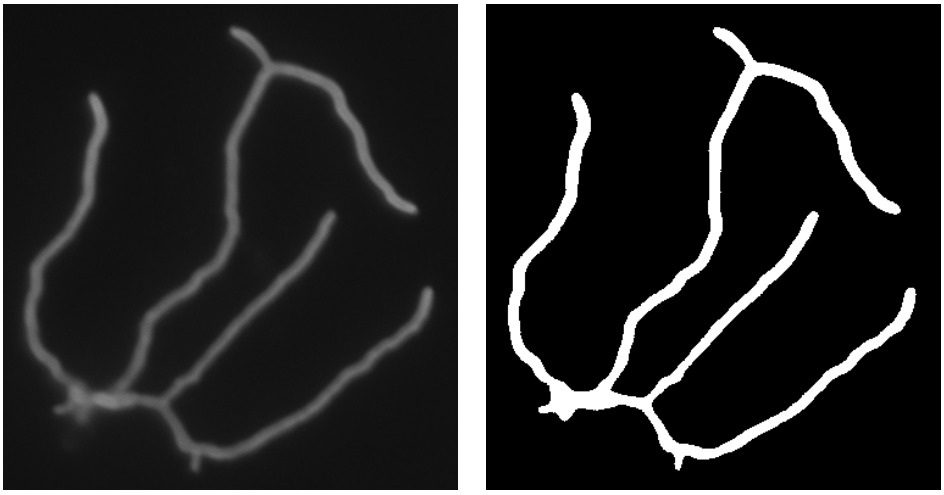

(a) (b)

Figure 4.2: Segmentation example: (a) Unprocessed microscope image. (b) Image after threshold segmentation.

values $f(i,j)$, the output image g is given by

$$g(i,j) = \begin{cases} 1 & \text{for} f(i,j) \geq T, \\ 0 & \text{for} f(i,j) < T. \end{cases} \tag{4.1}$$

In general, threshold segmentation is appropriate for images where the objects of interest do not touch each other and where the background grey levels are clearly distinguishable [23, 76]. In the case of the WGA images, the high contrast between background and cell wall suits this technique. However, where filaments are touching each other, the technique breaks down and is unable to distinguish between the two filaments. This is usually not a problem in our work, as the *Streptomyces* are sufficiently young that the filaments rarely touch.

The selection of segmentation threshold is key - too low a value and background image is merged with filament, too high and we break the filament connectivity. There are a range of automatic threshold selection algorithms that have been proposed, but no one algorithm has been found to be universally applicable [76, 23]. We adopt an approach known as iterative selection [76]. The aim is to provide an estimate of the mean background grey level I_b and the mean object grey level I_o and to set the threshold T between the two. To begin, an initial guess of T is made by calculating the mean grey level of the whole image. This threshold is then refined

according to the following steps:

1. Calculate the mean background intensity I_b by summing the intensities of all pixels with intensity $< T$ and dividing by the number of pixels.

2. Calculate the mean object intensity I_o by summing the intensities of all pixels with intensity $\geq T$ and dividing by the number of pixels.

3. Choose a new threshold level which is between the two mean levels just calculated, i.e. $T_{new} = \frac{1}{2}(I_b + I_o)$.

4. If T_{new} is different to T, go back to Step 1.

The process repeats until the threshold value stops changing. At that point, the threshold has reached a 'best guess' value. With our data, we find this approach usually selects a reasonably good threshold point. Even so, better results can often be obtained through manually adjustment of the value.

Figure 4.2a and 4.2b shows an example image before and after segmentation.

4.3.3 Background removal

The use of threshold segmentation relies on having an image with uniform illumination. This isn't always the case with florescence microscopy images, so we implement a background removal step prior to segmentation. The particular technique we have used is called a rolling ball algorithm [77] or sometimes a top-hat transformation [23].

We can consider the image as a 3-dimensional surface, with the height at each point determined by the pixel's intensity. The algorithm imagines rolling a ball of fixed radius underneath the surface, always maintaining contact between the surface and the ball. The path traced out by the top of the ball forms another surface and this new surface defines the background level across the image. Any pixel with an intensity below the background level is set to zero intensity, while any pixel with intensity above background keeps its current level.

Figure 4.3 illustrates the application of the rolling ball algorithm in 2-dimensions. The figure shows an intensity waveform with two objects represented by peaks. The

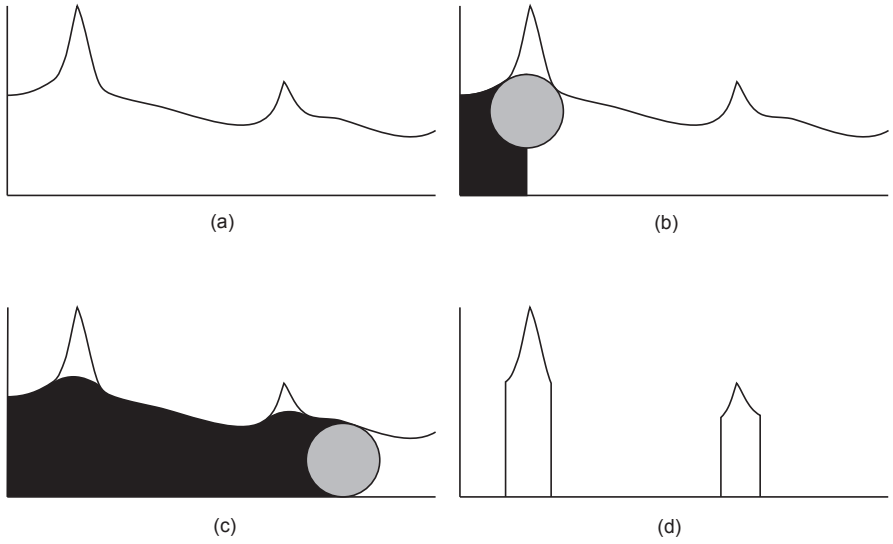

Figure 4.3: The rolling ball algorithm for background removal: (a) Example intensity waveform. Thresholding alone would probably keep first peak, but lose the second. (b) We begin to 'roll' the ball under the surface of the graph, ensuring it is always in contact with the graph. (c) The curve the ball draws as it rolls produces a new function which determines background intensity. (d) Any point below the background intensity function, we set to zero - this results in a new waveform that can more easily be thresholded.

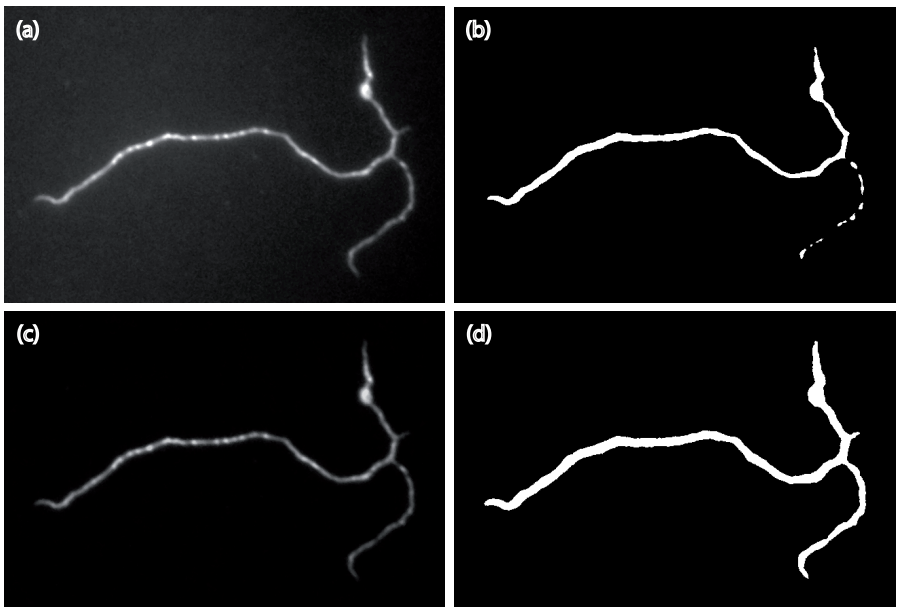

Figure 4.4: The effect of background removal: (a) Microscope image before processing. (b) Image after segmentation, but without background removal - hyphal shape is not preserved. (c) The original image after background removal. (d) The original image after background removal and segmentation, the original shape of the hyphae is preserved.

ball fits quite well to much of the waveform, but when it reaches the objects, its radius prevents it from following the line of the peaks. Thus, when the background is subtracted, the peaks are preserved.

Figure 4.4 shows an example microscope image and demonstrates the difference that the use of the rolling ball algorithm makes, compared to threshold segmentation alone.

4.3.4 Skeletonization

The result of segmentation is a binary image, but with filaments of variable thickness. Identification of points of interest and measurement of distances from such images is difficult, so the images are skeletonized in order to simplify this process. Thinning, or skeletonization, aims to reduce all lines to single pixel thickness, whilst still maintaining connectivity.

There are a large range of skeletonization algorithms, each of which has advantages and disadvantages and is more suited to one application than another. Lam *et al.* provide a comprehensive overview of skeletonization algorithms [47]. With the *Streptomyces* images, we were unable to find a single algorithm that reliably thinned all hyphae. Through experimentation with a range of *Streptomyces* images, we found that a combination approach involving the application of two algorithms would reliably skeletonize the images. We first applied the algorithm of Zhang and Suen [86], then the algorithm of Zhou *et al.* [87]. By doing this, we were able to get consistently reliable skeletonization results (Figure 4.5).

At a high level, both thinning algorithms operate by successive rounds of pixel erosion. In each round, the image is scanned and the decision to remove a pixel is made based on the number of pixels in the 8-neighbourhood and their connectivity. The process continues until no more pixels can be removed without breaking connectivity. Detailed descriptions of the algorithms are provided in Appendix B.

Figure 4.6a shows the effect of applying the thinning algorithms to the image in Figure 4.2b.

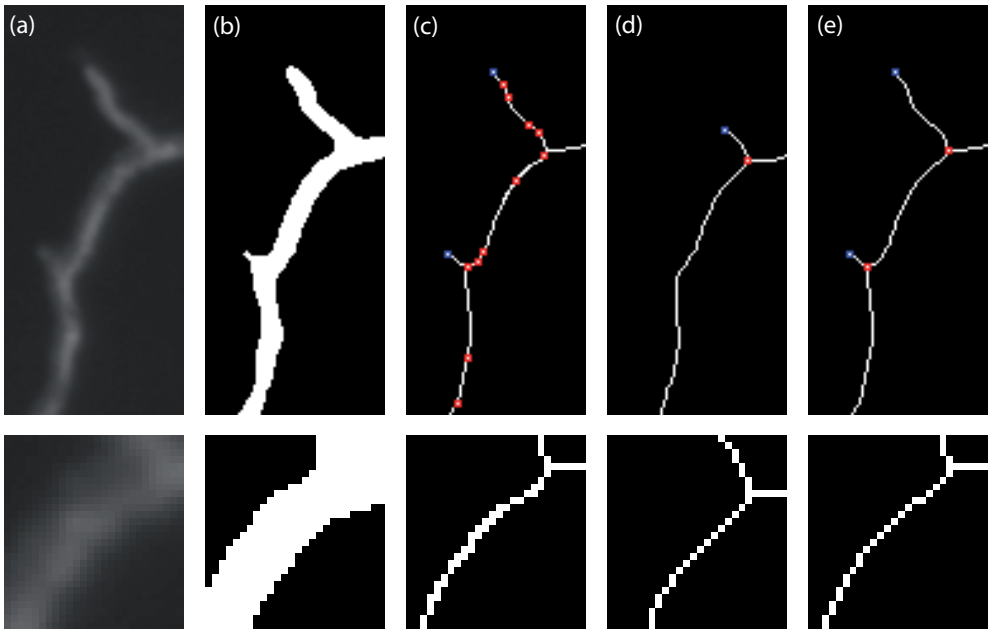

Figure 4.5: Skeletonization images: (a) Original microscope image. (b) Segmented image. (c) After skeletonization with the Zhang and Suen algorithm [86], the shape is well preserved, but the image is not perfectly thinned. (d) After skeletonization using the algorithm of Zhou *et al.* [87], the image is more consistently thinned, but we have lost some parts of the filament. (e) Applying both algorithms in series enabled us to achieve preservation of shape and consistent thinning.

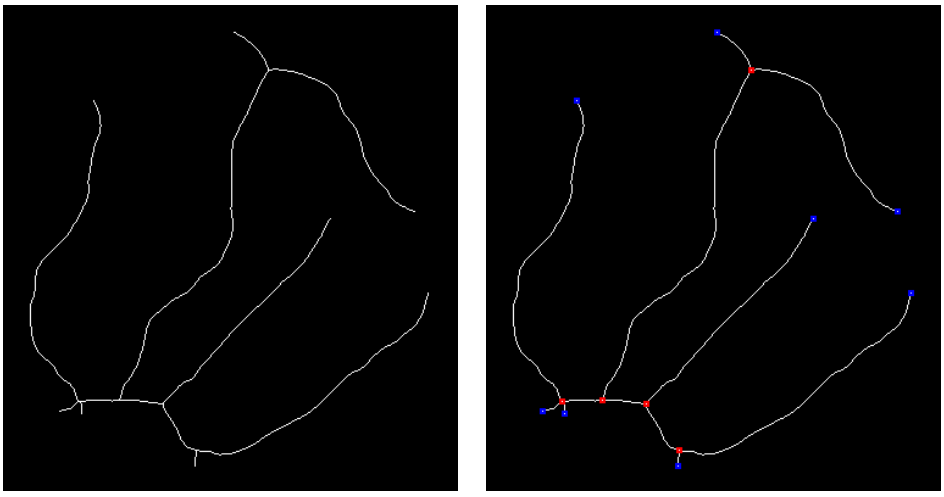

(a) (b)

Figure 4.6: Skeletonization and point finding: (a) Image from Figure 4.2b after applying the two thinning algorithms. (b) Branch and tip points located.

4.3.5 Point finding

In a skeletonized image, a branch point is defined as any point which has three or more neighbours in the 8-neigbourhood. To identify the branch points in the image, the image is raster-scanned and, for each pixel, a count of its neighbours is made. If the number of neighbours is greater than or equal to 3, the point is marked as a possible branch point.

Sometimes the pixel representation of a branching filament can result in more than one neighbouring pixel being marked as a branch point. To avoid this, once the whole image has been scanned, the list of possible branch points is rationalised to remove directly connected points. Any 8-neighbourhood connected points are replaced with a single point located at the average co-ordinate of the connected points.

Tip points are identified by running a series of 3-by-3 pixel templates over the image. Where a match is found, an end-point is marked (Figure 4.7).

Figure 4.6b shows the results of applying the point finding algorithms to the image in Figure 4.6a.

Currently, spore points have to be identified manually, by clicking on them in the PI channel image. This is a very easy thing for a human to identify, but surprisingly difficult for software to automatically recognise. We decided that manual selection of spore point was an acceptable approach to take for our purposes, but in the future it may be worthwhile to try to develop reliable algorithms for automatic spore identification.

Figure 4.7: Templates used for finding end points. Each template is moved over the image, pixel-by-pixel. Where template squares are shown as set (1), the underlying pixel must also be set. Where template squares are shown as unset (0), the underlying pixel must also be unset. Grey squares can be set or unset.

4.3.6 Identification of segments

We define a segment as a section of filament between two tip points, two branch points or one tip point and one branch point. Once the list of tip points and branch points has been built, the following algorithm is applied:

1. Take the next item from the list of tip points.
2. Follow the path from the tip point, pixel-by-pixel, until we meet either a branch point or a tip point.
3. Mark the set of pixels we have traveled as a segment. Remove them from the skeleton.
4. As a result of the removal of points in the previous step, test to see if the point we finished at should now be made into a tip point.
5. Are there any more tip points? If so, go back to Step 1. If not, we have identified all the segments.

4.3.7 Length measurement

The lengths of segments can be measured by calculating the arc length. Consider a real valued differentiable function, $f(x)$. The length, l, of an arc between $f(x_1)$ and $f(x_2)$ is given by

$$l = \int_{x_1}^{x_2} \sqrt{1 + \frac{df}{dx}^2}\, dx \ . \tag{4.2}$$

Consider the curve in Figure 4.8a. We can approximate the gradient $\frac{df}{dx}$ at point i by

$$\frac{df}{dx} \simeq \frac{f_{i+1} - f_{i-1}}{2d} \ ,$$

where d is the distance between adjacent points. This equation, combined with the trapezium rule for approximation of integrals, applied to Equation 4.2 yields the formula

$$l = d \sum_{i=0}^{N} \sqrt{1 + \left(\frac{f_{i+1} - f_{i-1}}{2d} \right)^2} \ .$$

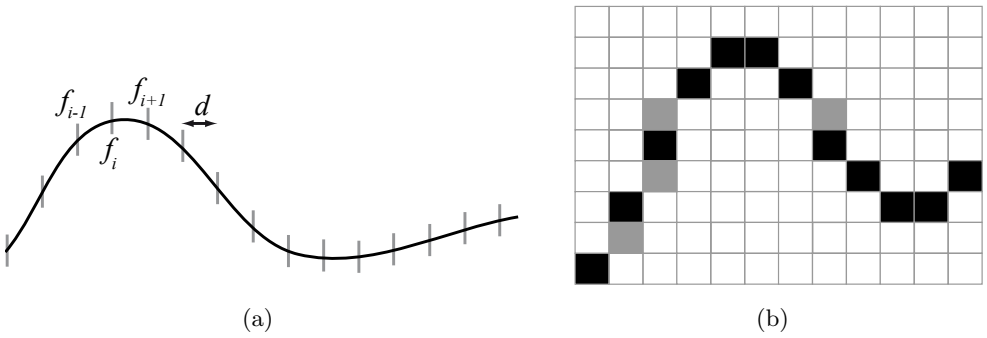

Figure 4.8: Finding the length of a segment: (a) We approximate the gradient at point i by using points either side. (b) When transferred to pixel-based lines, we sometimes have more than one value of y for a given x. We pick the middle value (black squares) and discard other values (grey squares).

In practical terms, if we work with single pixel increments for highest accuracy (i.e. we set $d = 1$), this simplifies to

$$l = \sum_{i=0}^{N} \sqrt{1 + \left(\frac{f_{i+1} - f_{i-1}}{2} \right)^2} \, .$$

Implementation is a relatively straightforward process of going through each x co-ordinate in a set of points and finding a corresponding y co-ordinate. This gives values for f_{i-1} and f_{i+1} and calculation of l is then trivial. In some situations, there may be more than one y co-ordinate for a given x co-ordinate, in which case we pick the middle value (Figure 4.8b). Accuracy is improved by rotating the image through 90 degrees (or, in practice, iterating through y co-ordinates, rather than x) if the segment being measured is taller than it is wide.

The result is a length measurement with units of pixels. To convert to microns, the value is multiplied by a scaling factor which is determined by the objective used on the microscope. Accuracy of the method was confirmed by testing against a series of plotted lines and curves of known length.

4.4 Calculation of biometrics and statistics

Once we know the location of branch and tip points, the segments that connect those points together, and the length of those segments, we can generate a wide range of biometrics and statistics. Many of these can be calculated relatively easily - for example, the number of growing tips, the total hyphal length and the distribution of

segment lengths are all easily derived and some results have already been published for the wild-type (see Chapter 5). However, a number of biometrics require somewhat more sophisticated processing which we now describe. These are, to our best knowledge, new metrics, for which there is no previously published work to consider.

4.4.1 Finding the primary filament

Filaments may be classified according to the order of their branching. Germ tubes are classified as primary filaments, lateral branches from the germ tube are secondary filaments, branches from these are tertiary filaments and so forth. We use the term filament depth to assign a number to this labelling, so primary branches have a depth of 1, secondary branches a depth 2 etc.

Because our images don't show the development of the same bacterium over time, we cannot classify filaments as they emerge. Instead, we retrospectively calculate the depth based on the assumption that all tips extend at a similar rate and that none of them stop growing. Though this assumption is unlikely to hold all of the time, it appears to be a safe assumption when dealing with young bacteria under conditions of stable nutrient supply [2, 11].

In view of our assumption, we apply the following algorithm to classify the depth of all filament sections:

1. Mark all segments as *unvisited*.
2. Set $startPoint = sporePoint$ and $d = 0$.
3. Increment d.
4. Build a list of all paths from $startPoint$ to all tip points, travelling along only unvisited segments.
5. Find the longest path in the list and mark each segment of it as *visited* and with depth of d.
6. For each branch point in the longest path, set $startPoint = branchPoint$ and repeat Steps 3-6.

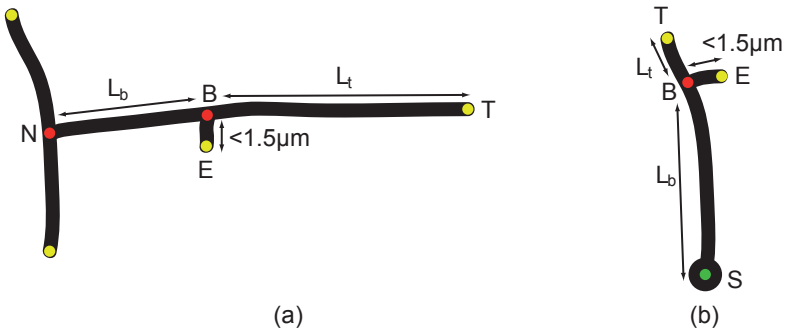

Figure 4.9: Detecting emerging tips: (a) The tip E is classified as an emerging tip because it is less than 1.5µm long and is connected to branch point B, which is in turn connected to the growing tip T and a basal node, N. (b) The first branch on a germ tube is a special case of the emerging tip. Here the basal node must be the spore point, S.

We can also use the depth data to calculate a measure of hyphal balance - that is, the proportion of hyphal length attached to each germ tube. In *S. coelicolor*, there are typically two germ tubes, the second emerging later than the first and extending in the opposite direction. Adding up the hyphal length on each side of the spore provides insights into the symmetry of the organism.

4.4.2 Detection of emerging tips

We have an interest in identifying newly formed branches in order to gather data on the positioning of child branches relative to the parent filament. We accomplish this by looking through the list of tip points and identifying any of these where the distance to the nearest branch point is less than a threshold value. This tip is classed as an emerging tip and the nearest branch point provides the point of branching on the parent filament (Figure 4.9a). The threshold value needs to be chosen carefully - if it is too low, we miss tips that should be included and reduce the size of our sample set, but if it is too high, we end up capturing mature tips as well as emerging tips. We chose a threshold value of 1.5µm based on visual inspection of a number of images.

The parent branch point, B, must be connected to a node, N, which represents either its own birth from another filament, or the site of its previous child branch. New branches tend to form between the tip and the previous branch [45], so the parent branch point is usually connected to a tip point, T, which represents the

parent filament's active tip. The distances from T to B and from B to N are useful indicators of branching behaviour.

The algorithm for detection of emerging tips is as follows:

1. Take the next point, P, from the list of tip points.
2. Let B be the branch point connected to P.
3. P is classed as an emerging tip if and only if:
    - the distance from P to B is less than 1.5µm;
    - *and* B is connected to a tip point T, that isn't P;
    - *and* B is connected to a branch point, N, that isn't a spore.
4. Are there any more tip points? If so, go to Step 1.

A special case of this algorithm is used to detect the location of the first branch on a germ tube (Figure 4.9b). For this, instead of looking for B to be connected to a tip point and another branch point, we expect B to be connected to a tip point and the spore point.

4.4.3 Detection of apical branches

We also want to identify apical branching. In wild-type *S. coelicolor*, new branches predominantly form behind a tip, but in some fungi and mutants, the growing tip can split into two [17, 69, 70]. Quantification of the degree of apical branching could be an important way of understanding the differences between two strains of bacteria.

Recent apical branches may be identified by looking for two emerging tips which share the same parent branch point (Figure 4.10). The following algorithm can be used to detect them:

1. Take the next point, P, from the list of tip points.
2. Let B be the branch point connected to P.
3. P is classified an apical tip if and only if:

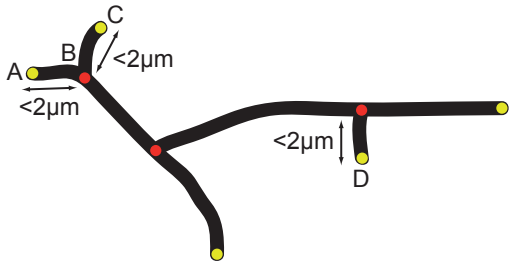

Figure 4.10: Detecting apical branches: We look for two short tip segments which share the same branch point. In this example, tip points A and C represent apical branches which share the same branch point, B. However, point D is not an apical branch, as there is no other short tip segment that shares the same branch point.

- the distance from P to B is less than 2μm;
- *and* B is connected to a second tip point which is less than 2μm from B.

4. Are there any more tip points? If so, go to Step 1.

4.4.4 Pairwise distances

Our tool generates pairwise distance data for an organism, as a way of representing the spatial arrangement of mycelia. The pairwise distance data is calculated by measuring the direct Euclidian distance from each tip point to each of the other tip points in the organism. The Euclidian distance, l_e, between point P_1 at co-ordinates (x_1, y_1) and point P_2 at co-ordinates (x_2, y_2) is given by

$$l_e = \sqrt{(x_1 - x_2)^2 + (y_1 - y_2)^2} \ . \tag{4.3}$$

4.4.5 Segment deviation

During our experimental work, we observed that filament segments of wild-type *S.coelicolor* were generally quite straight compared to some of the mutant bacteria and we wanted a metric to quantify this apparent difference. Thus, we introduce the segment deviation, which is a measure of how much longer a segment is than the Euclidian distance between the two ends of the segment (Figure 4.11). If l_s is the measured length of the segment and l_e is the Euclidian distance between the two ends of the segment, then the segment deviation, d is given by

$$d = \frac{l_s}{l_e} \ . \tag{4.4}$$

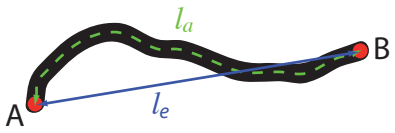

Figure 4.11: Segment deviation quantifies how much longer a measured segment length, l_s, is than the straight-line Euclidian distance, l_e, between the two ends of the segment.

An alternative way of expressing this is as a deviation percentage - that is, the increased length of l_s as a percentage of l_e, i.e.

$$d = 100\left(\frac{l_s}{l_e} - 1\right) . \tag{4.5}$$

Thus, a value for d of 10 means that the measured segment was 10% longer than the Euclidian distance between the segments two ends.

4.5 JFilamentAnalyser

The image processing and analysis techniques described in the preceding sections have been implemented in a Java application called JFilamentAnalyser. It is designed to be a general purpose tool for analysis of filamentous microbes, but has currently only been used on our *Streptomyces* dataset.

4.5.1 Basic use of the tool

The application's user interface is divided into two panels - a large scrollable window on the left-hand side is used for display of microscope images, while a narrower panel on the right-hand side displays organism biometrics (Figure 4.12). Upon initially starting the application, the user can load previously analysed images, or select the 'Wizard' icon to process a new image (Figure 4.13). The wizard takes the user quickly through five steps to turn a microscope image into a fully analysed bacterirum. Most of the time, the user can just click the 'Next' button to move through each stage of the wizard, but occasionally some user intervention may be required to ensure better results. The five steps are as follows:

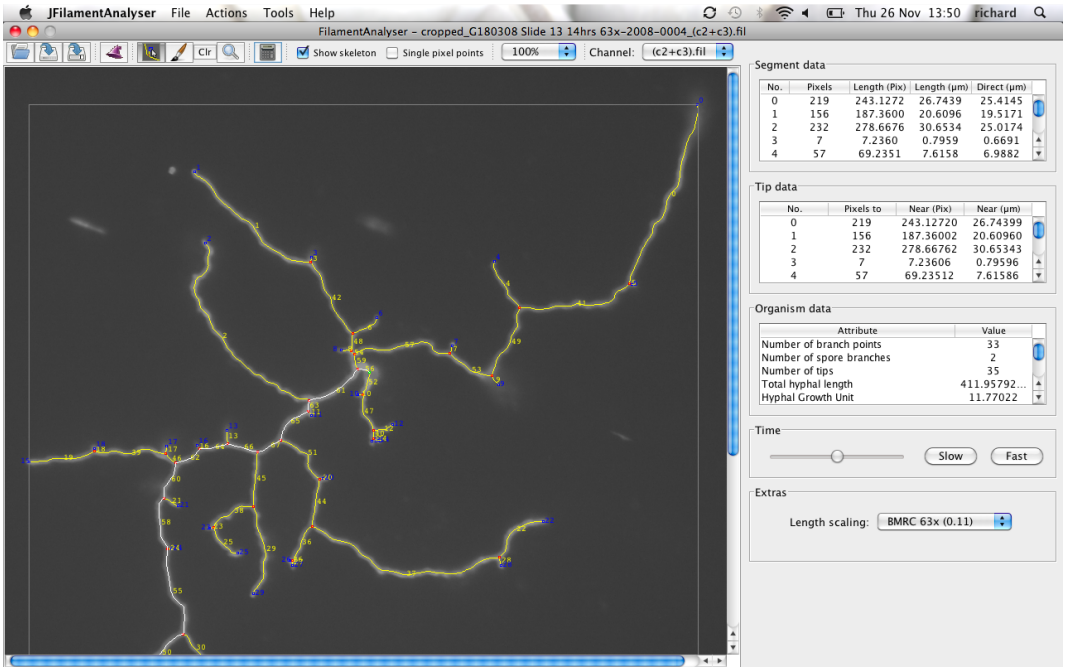

Figure 4.12: JFilamentAnalyser running: The toolbar at the top of the screen provides a number of options for editing the skeleton, changing the location of branch points and tip points and zooming in to the image. A drop down menu to the right of the toolbar allows the user to select a different channel image to view, with the skeleton displayed on top of it.

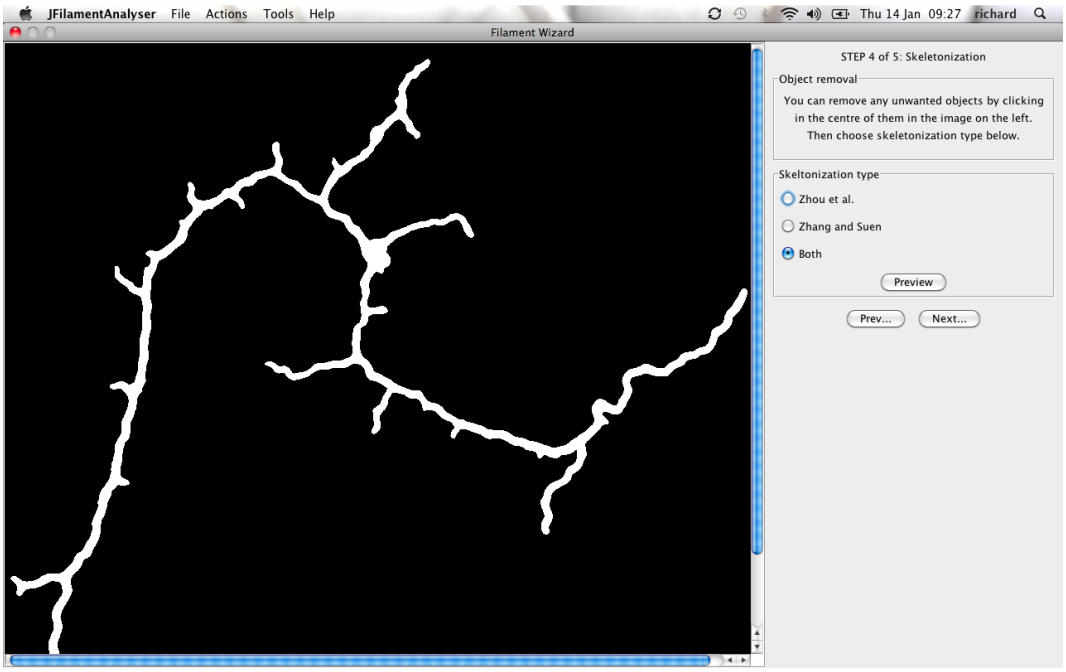

Figure 4.13: The filament wizard: The user is taken through five steps to complete the analysis of a microscope image. Usually each step just requires a click of the 'Next' icon, though parameters can be changed if necessary.

1. **Selection of the image and specification of microscope objective:** we use a naming standard for microscope images which includes the magnification. If this convention is followed, the software will automatically select the correct objective.

2. **Selection of cropping zone, pre-processing and background removal:** the user can drag a selection box around the portion of the image containing the bacterium they wish to analyse. The software will perform this crop on all channel images. The user can also select whether to perform background removal and has a choice of three different preprocessing filters - by default, the Gaussian filter is selected.

3. **Selection of segmentation threshold:** the software picks an initial threshold value, but the user is able to drag a slider to adjust this.

4. **Removal of artefacts and skeletonization:** the user is able to click on any objects that survived segmentation, but are not part of the mycelia - these will then be removed by the software. The user can also chose whether to run one or both of the skeletonization algorithms. By default, both skeletonization algorithms are selected.

5. **Point identification:** the skeleton is shown and tip points and branch points are automatically identified. The user clicks 'Next' to complete the wizard process and return to the main analysis window.

The processing involved in each step happens very quickly. Most stages take under a second to process, though skeletonization can take 3 or 4 seconds for complicated structures. Thus, it is very easy to complete the whole wizard process in under a minute for more straightforward structures and a few minutes for very complicated or poor quality images.

When the wizard has completed, results are saved into a filament data file and the newly analysed image is shown in the main window, overlaid by the skeleton, tip points and branch points. Biometrics and statistics can be generated by clicking on the 'Analyse' button in the toolbar and results of this analysis are shown in the scrolling lists to the right of the main window. These statistics may be saved, or

appended, to a set of comma separated value (CSV) files, the formats of which are described in Appendix C.

Other tools in the toolbar allow the image to be zoomed in or out, the skeleton to be edited manually, tip points to be added or removed, branch points added or removed and spore points added or removed.

4.5.2 Overview of software design

The software adopts an object-oriented design and is written in Java. Figure 4.14 uses UML notation [78] to show the interaction between the main classes. Implementations of all algorithms were carried out by the author, with the exception of the rolling ball algorithm for background removal and the Zhang and Suen skeletonization algorithm. The former is implemented using a class provided by the open source ImageJ library, while the latter implementation is taken from [64]. A brief overview of the other main classes follows.

The class JFilamentAnalyser is the entry point for the application and provides most of the GUI functionality. The class FilamentFile is used to represent the contents of a filament file - specifically, the co-ordinates of all skeleton points, branch points, tip points and spore points. The class OrganismData represents all generated biometrics and statistics and provides methods to write these to a file.

The JFilamentAnalyser class passes filament file point lists to a number of other classes which perform analysis. PrimaryFilamentFinder not only locates the primary filament, but classifies all filaments according to branching order. SegmentLengthFinder measures the length of every segment using the arclength calculation described in Section 4.3.7. EmergingBranchFinder locates emerging branches.

The FilamentWizard class provides the GUI components of the filament wizard and uses a number of other classes to perform image processing and analysis. Cropper performs a crop on a file or series of files. MeanFilter, MedianFilter and GaussianFilter provide the pre-processing filters their names suggest. BackgroundRemover and ThresholdSegment provide methods to carry out the rolling ball algorithm and threshold segmentation respectively. LineThinner implements the two skeletonization algorithms, and provides methods to call one or both of

them. All the image processing algorithms operate on the standard Java BufferedImage class, which provides easy pixel-by-pixel manipulation of images.

The BranchPointFinder class implements the algorithms to locate not only branch points, but also tip points. Skeleton points, tip points, branch points and spore points are stored in a FilamentFile object, which is written to disc before passing back to the main JFilamentAnalyser class for biometrics and statistics gathering.

Appendix C provides further details on the design of JFilamentAnalyser, including descriptions of the file formats used to hold filament data and statistics.

4.6 Discussion

In this chapter, we have outlined the processing steps necessary to perform semi-automatic analysis of microscope images of young filamentous microbes. We have described algorithms involved in pre-processing, background removal, segmentation, skeletonization and the automatic location of branch points and tip points. We have described algorithms used for locating apical branches, newly emerging tips, for the classification of branching order and for computing biometrics from these quantities.

We have also introduced a software tool, JFilamentAnalyser, in which we have implemented the algorithms described and which is capable of performing supervised automatic analysis of filamentous structures. In the next chapter, we present the results of the analysis of around 2,200 bacterial images carried out using this tool.

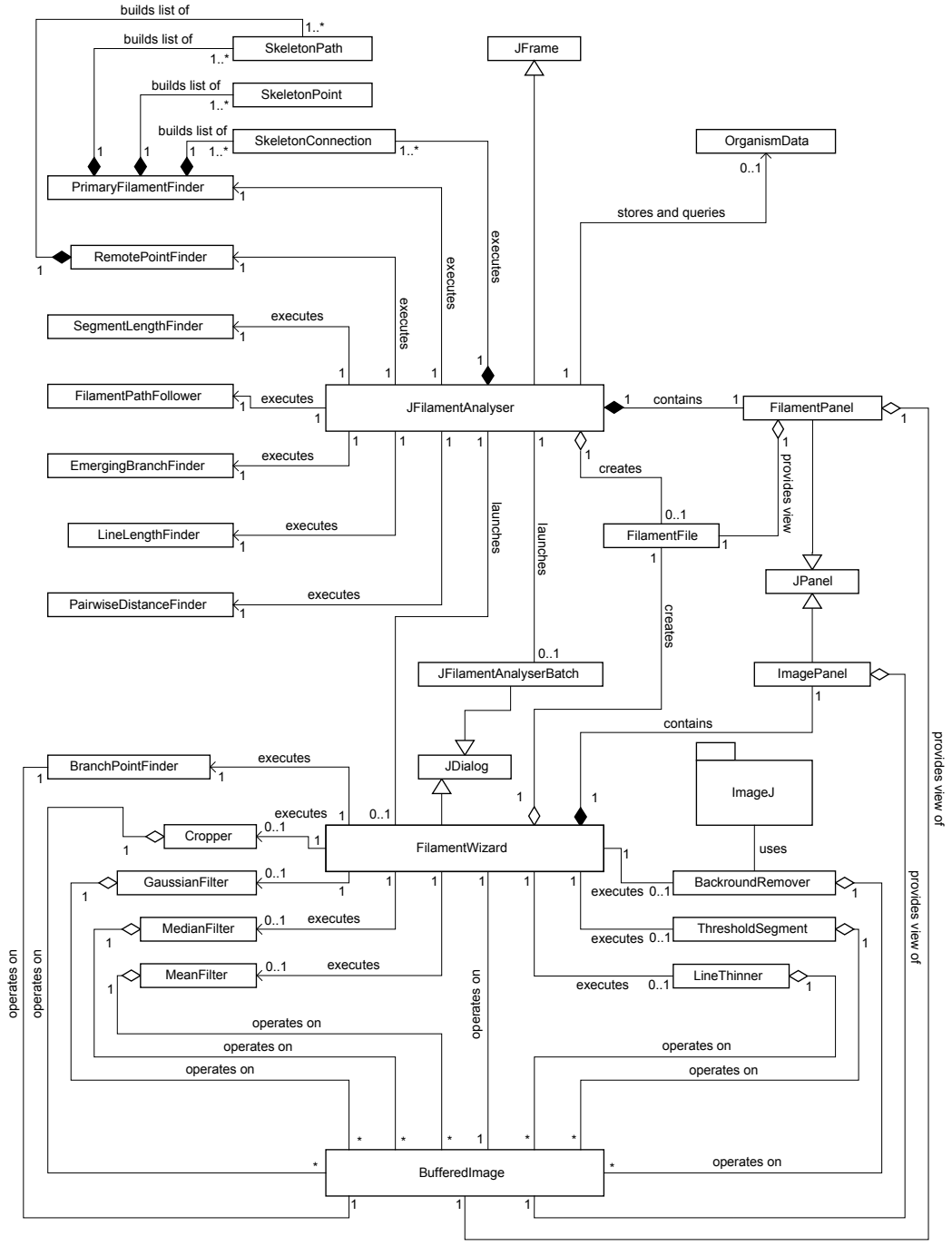

Figure 4.14: Class diagram, in UML notation, of JFilamentAnalyser.

Chapter 5

Experimental Results

5.1 Summary

In the previous chapter, we described a collection of image processing algorithms for carrying out semi-automatic analysis of microscope images of growing *Streptomyces coelicolor* bacteria, that we have implemented in a software tool called JFilament-Analyser. We used this tool to analyse a data set consisting of thousands of images we obtained according to the experimental procedures described in Chapter 3. In this chapter, we summarise the results of the analysis and present a range of graphs and statistics which together form a quantitative description of the morphological differences between wild-type and mutant bacteria.

In Section 5.2, we begin by presenting a summary of the data that we generated. In Section 5.3, we describe some qualitative observations on the differences between the bacteria. In Section 5.4 and the following sections, we describe our quantitative results in detail, examining specific statistics and biometrics individually. Where comparable data has already been published, we compare our results with these. However, to date, there has been a lack of quantitative work on *Streptomyces* morphology and we believe much of the data presented here is unique.

5.2 The data

Table 5.1 summarises the time-series experiments carried out and the number of images analysed in each experiment. In total, nearly 2,200 images were analysed.

			Number of images						
Date	Bacteria	Media	8hrs	10hrs	12hrs	14hrs	16hrs	18hrs	Total
18 Mar 08	wild-type	MMM	53	57	68	74	60	32	344
29 May 08	wild-type	MMM		40	40	40	40	40	200
11 Jun 08	wild-type	SFM		25	40	40	40		145
20 Jun 08	wild-type	SFM		40	40	40	24		144
29 May 08	Δ*scy*	MMM		40	40	40	40	40	200
2 Jul 08	Δ*scy*	MMM		40	40	40	40	21	181
11 Jun 08	Δ*scy*	SFM		18	13	40	40		111
20 Jun 08	Δ*scy*	SFM		40	40	30	23		133
2 Jul 08	Δ*scy*	SFM		40	40	40			120
10 Jul 08	Δ*filP*	MMM		40	41	40	40		161
17 Jul 08	Δ*filP*	SFM		40	40	40	30		150
10 Jul 08	Δ*scy-filP*	MMM		40	40	40	23		143
17 Jul 08	Δ*scy-filP*	SFM		40	40	40	22		144

Table 5.1: Details of the experimental data sets, showing the number of images collected at each time point.

For those combinations of media and bacteria where we carried out repeat runs, we have combined the results of the original and repeat runs. Thus, there are eight sets of results presented, consisting of four bacterial strains, each grown on two types of media. Further sets of results are contained in Appendix D.

5.3 Qualitative observations

When grown on MMM medium, images of wild-type and the mutant strains appear superficially similar, though the statistics in the sections that follow highlight some significant differences. However, when grown on SFM, differences between the wild-type and the mutants are much more obvious (Figure 5.1). Most significantly, the Δ*scy* and Δ*scy-filP* mutants appear to show a large number of short, aborted, branches, possible apical branching and generally more compact structures than the wild-type. The Δ*filP* mutant also shows a markedly different morphology to the wild-type, with more curling and overlapping hyphae. This observation is in agreement with the description given in the publication that originally identified *filP* [4]. In it, Bagchi *et al.* describe a 'characteristic distorted morphology' for a Δ*filP* mutant grown on cover slips in solid media, where a wild-type grew in a 'straight fashion' under the same conditions.

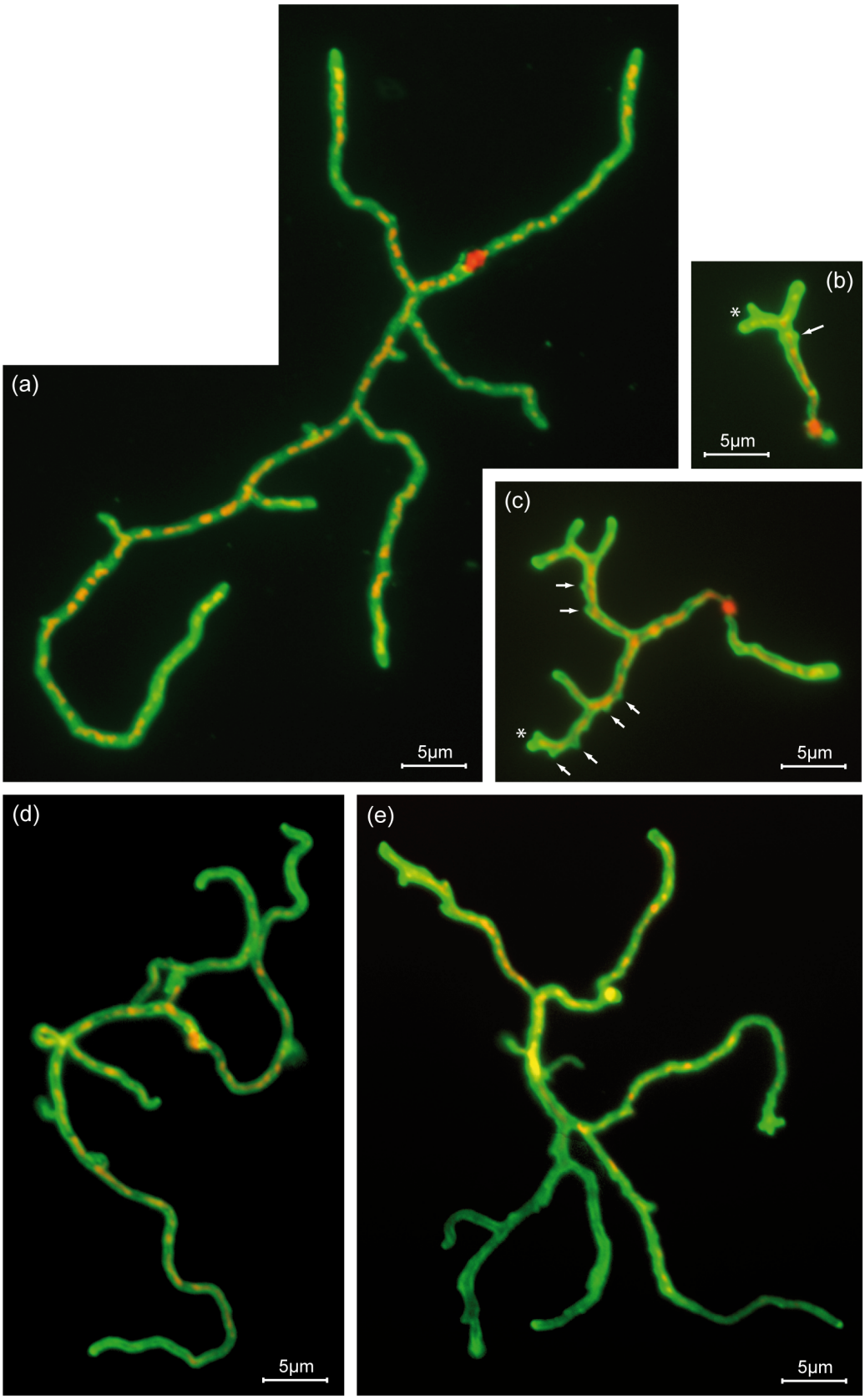

Figure 5.1: Fluorescence images of *S. coelicolor* on SFM medium: (a) Wild-type. (b) and (c) Δ*scy* mutant. Note appearance of aborted tips (arrows) and apical branching (asterisk). (d) Δ*filP* mutant, which has a curlier appearance than the wild-type with some overlapping filaments. (e) The Δ*scy-filP* mutant.

5.4 Total hyphal length

The Total Hyphal Length (THL) is the sum of all filament lengths for a single bacterium. Figure 5.2 provides natural log graphs of total hyphal length against time for all eight sets of data. Error bars provide an indication of the standard error.

The number of measurements used to define each point on the graph is high, so error bars on individual points are small. However, there are only a few time points, which makes finding a good linear fit difficult. Thus, there is quite a wide interval on the 95% confidence bounds of the linear fit for some data sets (Table 5.2). Despite this, there appears to be quite a good linear fit to most points of each graph, which indicates exponential growth. This observation is in support of the prevailing view, outlined in Chapter 2, that *Streptomyces* exhibits an exponential increase in overall biomass, at least in the early stages of colony growth [11].

Our data for the wild-type on MMM is in good agreement with that from Allan and Prosser [2], who also used *S. coelicolor* and a minimal media. Their data shows an almost identical growth rate for the same stage of growth. This is remarkable, considering that they were only monitoring the growth of a single spore, while our data covers several hundred.

On both media, the growth rate (as indicated by the gradient, Table 5.2) is highest for the wild-type, followed by Δ*scy* , Δ*filP* and Δ*scy-filP* . However, the growth rates of wild-type and the Δ*scy* mutant, particularly on MMM, are very similar. This is perhaps surprising and, if not attributed to errors in data or fitting, suggests that the Δ*scy* mutant doesn't have an overall physiological defect, but one that affects only morphological patterning.

	MMM				SFM			
	wild-type	Δ*filP*	Δ*scy*	Δ*scy-filP*	wild-type	Δ*filP*	Δ*scy*	Δ*scy-filP*
Lower	0.40	0.14	0.34	0.16	0.17	0.05	-0.27	0.00
Gradient	**0.47**	**0.31**	**0.44**	**0.28**	**0.46**	**0.25**	**0.35**	**0.21**
Upper	0.54	0.48	0.54	0.40	0.74	0.45	0.98	0.43
G (mins)	88.49	134.16	94.52	148.53	90.41	166.36	118.83	198.04

Table 5.2: Summary table for total hyphal length graph. Lower and upper bounds refer to the lower and upper 95% confidence bounds of the linear fit. G is the generation time, in minutes.

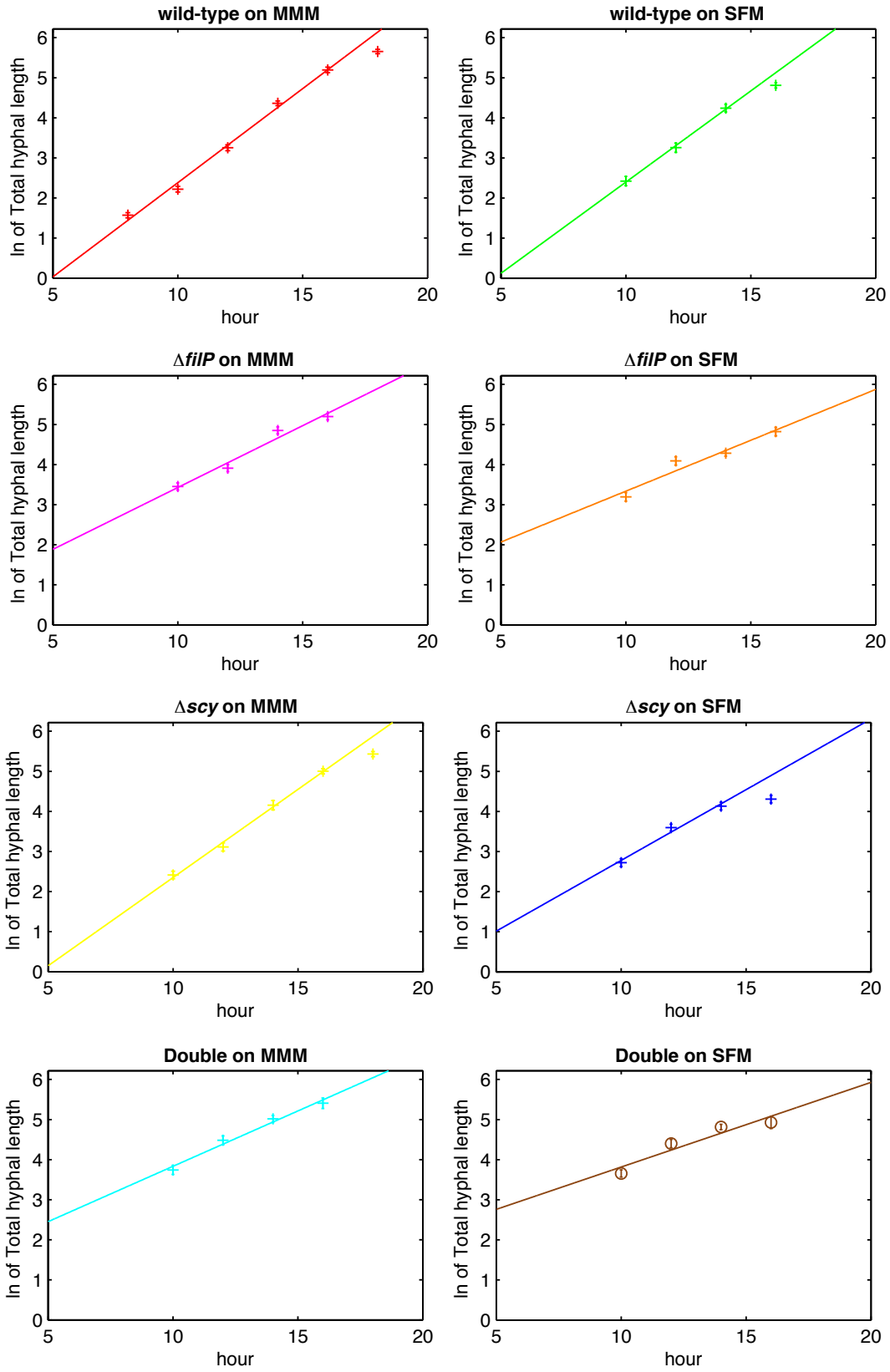

Figure 5.2: Graphs of natural log of total hyphal length against time. Plot points represent mean values of total hyphal length for the corresponding time point and error bars indicate standard error. Lines are linear fits of the data points.

5.5 Generation time

In rod-shaped or spherical bacteria, the generation time is the time taken for a bacterial cell to double. The generation time, G, is given by

$$G = \frac{t \ln 2}{\ln B - \ln B_0}$$

where B is the number of bacteria at time t and B_0 is the number of bacteria at time $t = 0$. Filamentous bacteria such as *Streptomyces* do not divide to form distinct cells, but we can still approximate the doubling time by replacing the number of cells with the total hyphal length. Thus, we can use the gradient, m, of the fit lines in Figure 5.2 to calculate the generation time of our samples. We substitute m for $\ln B - \ln B_0$ and set $t = 1$, giving

$$G = \frac{\ln 2}{m} \ .$$

Table 5.2 lists values of G for the eight bacteria/media combinations. It is difficult to compare these results to published data, as differences in bacterial strains or medium composition can have a big effect. However, figures of around 80-120 minutes are common for wild-type *Streptomyces coelicolor* grown on minimal media [20, 35].

5.6 Number of tips

Figure 5.3 provides graphs of number of tips against total hyphal length for the eight bacteria and media combinations. Linear fit lines are included, with 95% confidence bounds marked with dashed lines. For clarity, Figure 5.4 provides overlaid plots, allowing easier comparison of different experiments.

In all experiments, we observe a linear increase in the number of growing tips, which accounts for the exponential increase in overall hyphal length. As with the total hyphal length data, we find a close fit between our wild-type on MMM data and the Allan and Prosser data [2].

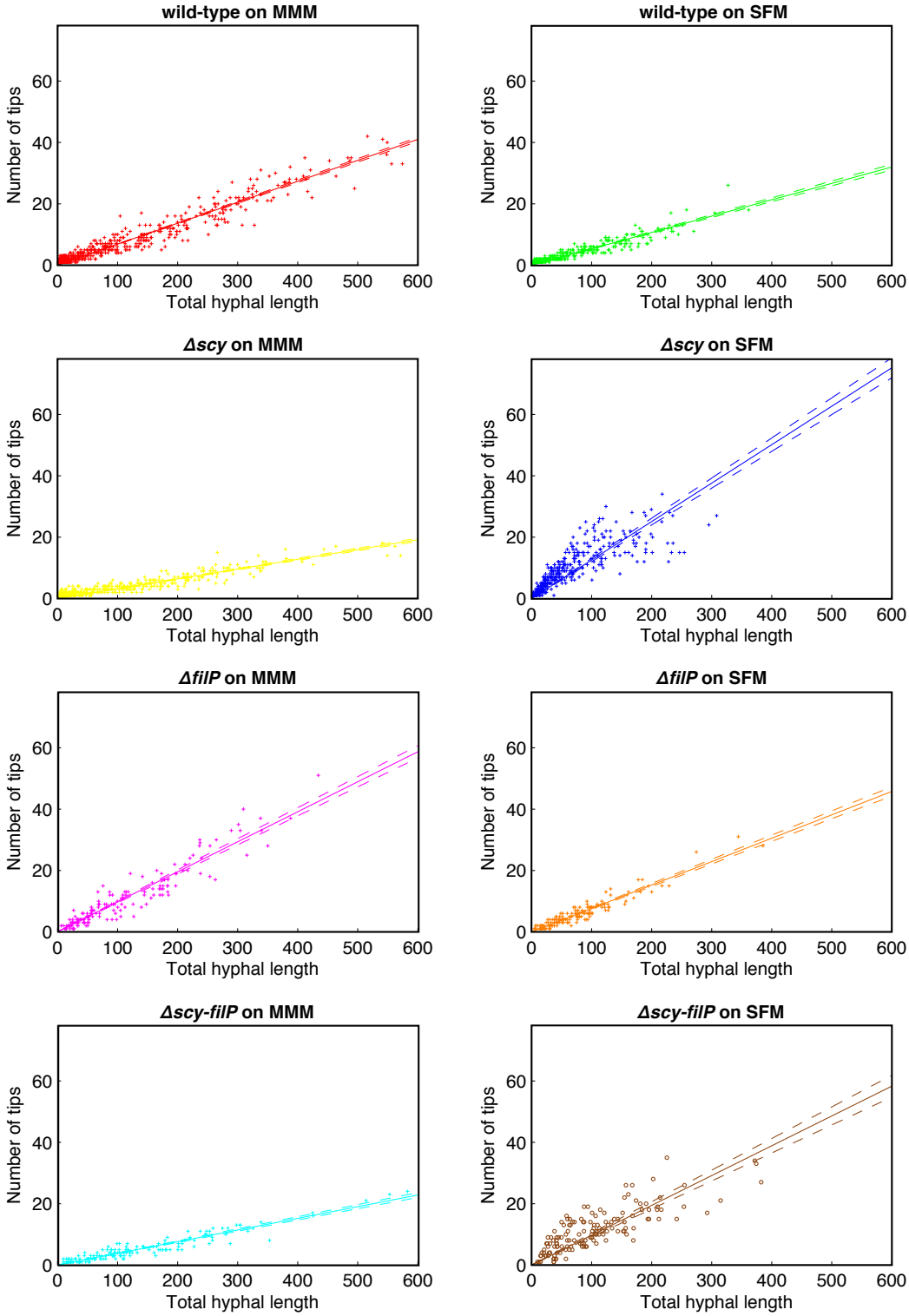

Figure 5.3: Graphs of number of tips against total hyphal length. Solid lines are linear fits, dotted lines represent the 95% confidence bounds for the fits.

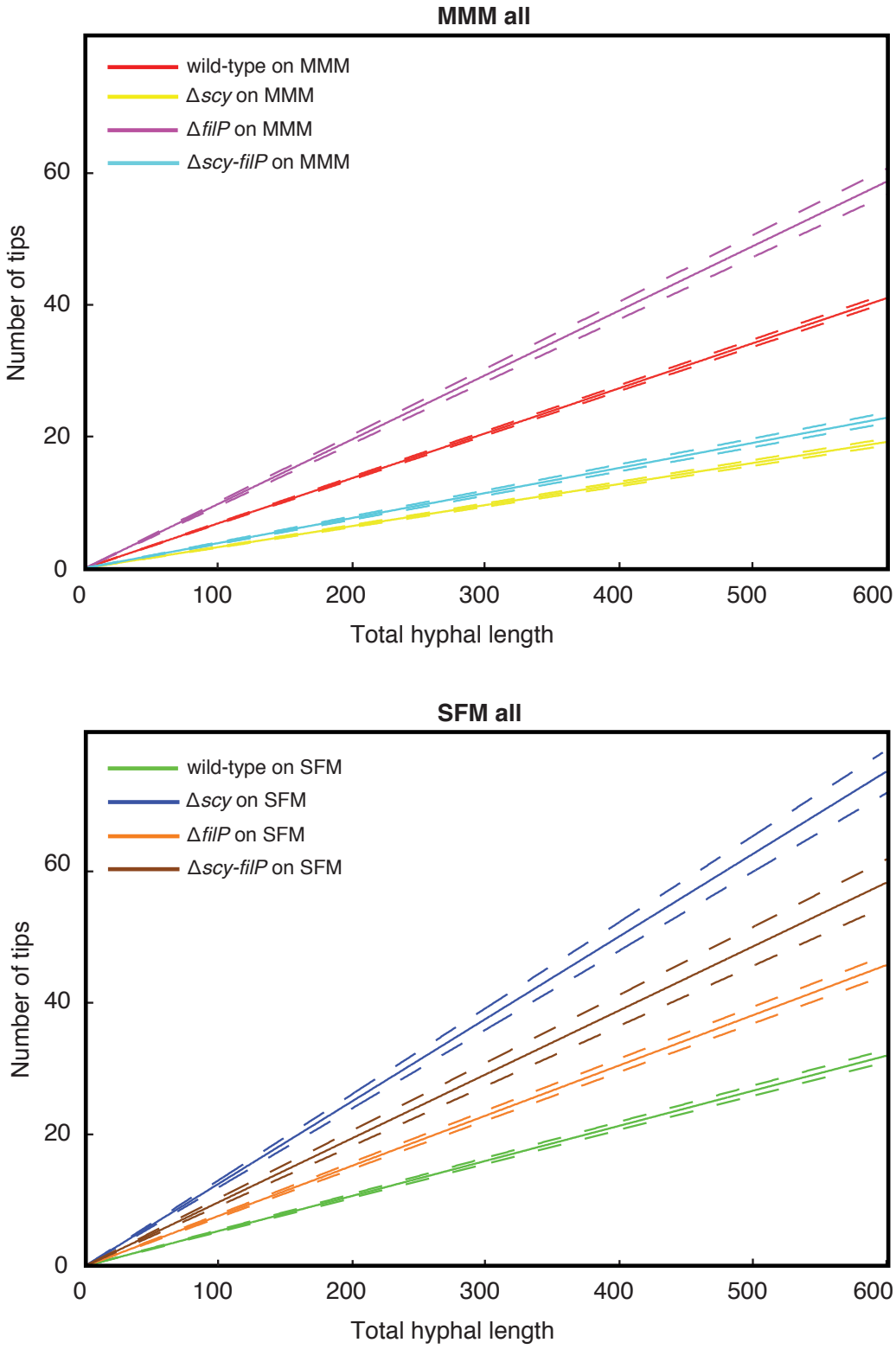

Figure 5.4: Graphs of number of tips against total hyphal length. Solid lines are linear fits, dotted lines represent the 95% confidence bounds for the fits.

We note the following observations:

- On MMM, the Δ*filP* mutant produces the most tips, followed by wild-type, then Δ*scy-filP* and the Δ*scy* mutant.
- On SFM, the Δ*scy* mutant produces the most tips, followed by the Δ*scy-filP* mutant, the Δ*filP* and wild-type produces the fewest.
- wild-type and the Δ*filP* mutant produce more tips on MMM than on SFM.
- The Δ*scy* and Δ*scy-filP* mutants produce more tips on SFM than on MMM.

5.7 Segment lengths

Figure 5.5 shows histograms of internal segment lengths for the eight sets of data. Internal segment lengths are all filament sections which are bounded by two branch points, but not segments which contain a tip point at either end. Thus, these segments are fixed in size and do not grow with the extension of the growing tips. The histograms are composed of data from all time points. Table 5.3 provides a numerical summary of the histogram data, providing mean values and chi-squared comparisons of the distributions. Finally, Figure 5.6 summarises the data as a box plot.

The frequency distribution we found for wild-type on MMM is very similar to that described by Allan and Prosser [2], who also used *S. coelicolor* and a minimal media. However, the results in [2] were based on considerably less repeats and much less sophisticated measurement. More recently, Jyothikumar *et al.* reported an average distance between branches of 7.63 µm for growth of *S. coelicolor* on a minimal media [38]. This is similar to our mean value of 8.40 µm and the small difference is almost certainly explained through slightly differing medium composition and experimental conditions.

The Δ*scy* and Δ*scy-filP* mutants show large differences in the distribution of segment lengths on the two different media and this is also reflected in the chi-squared p-values. On MMM, we see wider distributions, with a mean of 12.87 µm for the Δ*scy* mutant and 12.92 µm for the Δ*scy-filP* mutant. On SFM, there is a

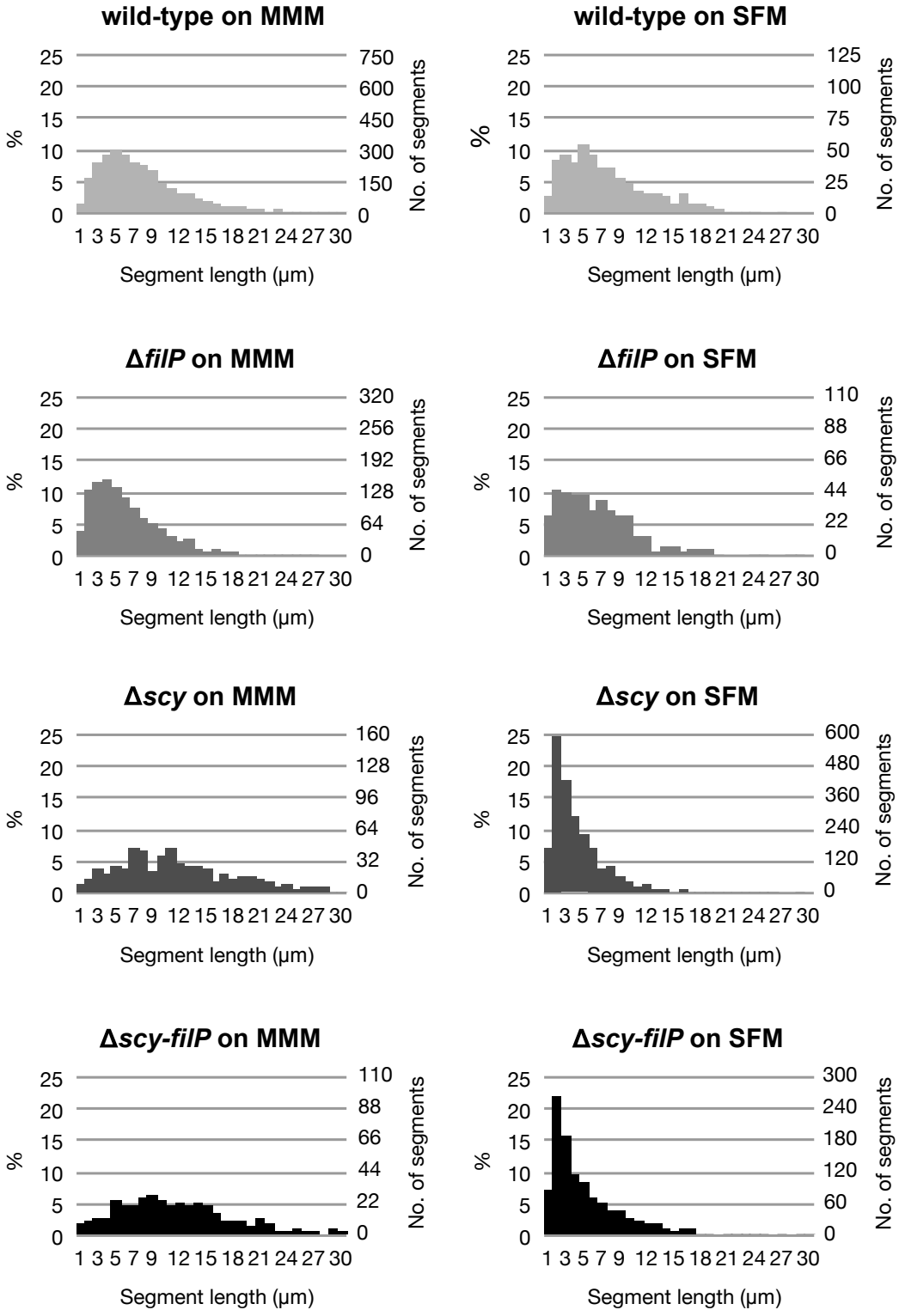

Figure 5.5: Histograms of internal segment lengths, bin size 1 μm. Graphs plotted on % scale to aid comparison, with absolute counts also indicated. Distributions for wild-type and Δ*filP* vary little between SFM and MMM. However, distributions for Δ*scy* and Δ*scy-filP* show notable differences on the two media, with a tendency towards much shorter segment lengths on SFM and longer lengths on MMM.

Bacteria	Media	Number of segments	Mean (µm)	χ^2	two tailed p-value	Significant? ($p < 0.05$)
wild-type	MMM	2935	8.40			
wild-type	SFM	517	7.43	8.18	1.0000	No
Δ*filP*	MMM	1254	6.25	18.14	0.9988	No
Δ*filP*	SFM	440	6.33	31.96	0.8136	No
Δ*scy*	MMM	677	12.87	68.67	0.0032	Yes
Δ*scy*	SFM	2382	4.15	129.13	0.0001	Yes
Δ*scy-filP*	MMM	431	12.92	68.50	0.0033	Yes
Δ*scy-filP*	SFM	1194	5.20	94.02	0.0001	Yes

Table 5.3: Summary table for segment length histogram, showing number of segment lengths measured, mean segment length and chi-squared comparisons between the wild-type on MMM distribution and each of the other experimentally derived distributions. For the chi-squared test, the number of bins equates to 40 degrees of freedom and we use the convention of assuming statistical significance when $p < 0.5$.

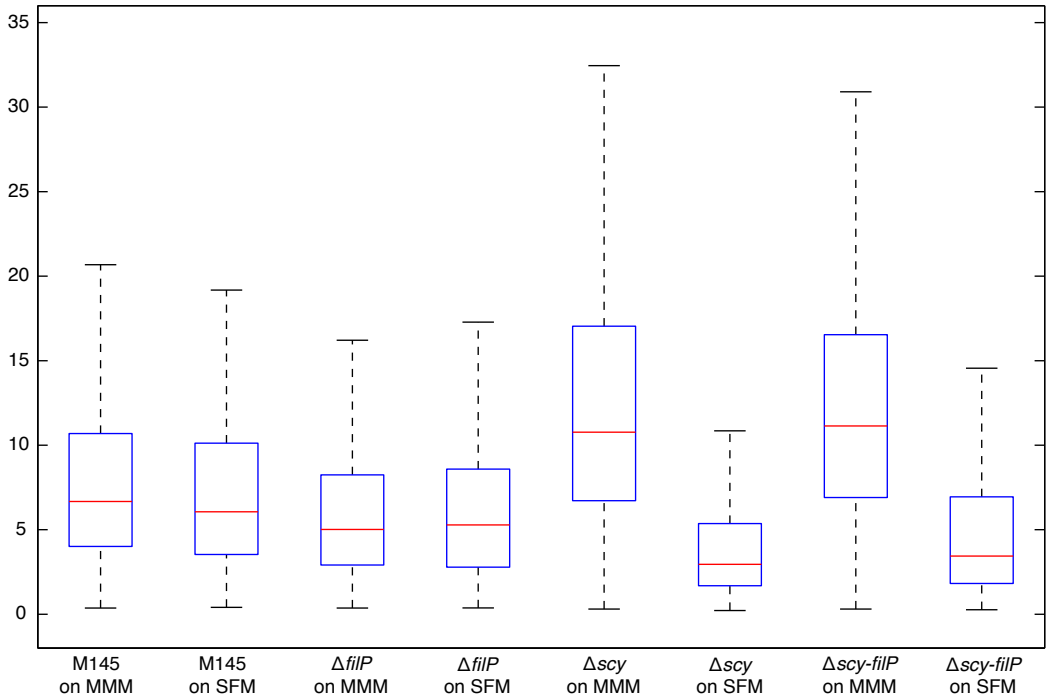

Figure 5.6: Segment length box plot: red lines indicated median values, the edges of the box are the 25th and 75th percentiles, and the whiskers extend to the most extreme data points not considered outliers. Plot produced with standard Matlab boxplot function.

narrower distribution and at shorter lengths, with mean segment lengths of 4.15 µm and 5.20 µm for Δ*scy* and Δ*scy-filP* respectively. In contrast, the wild-type and the Δ*filP* mutant yield similar segment length distributions on MMM and SFM.

Comparing the histograms of the wild-type and the mutants, we note that the Δ*scy* and Δ*scy-filP* mutants display longer segment lengths than the wild-type and Δ*filP* mutants when grown on MMM, but shorter segment lengths when grown on SFM.

5.8 Germ tubes

All the bacterial strains we examined began growth with one initial germ tube emerging from the spore and, after a delay, this was usually followed by a second germ tube. Figure 5.7 shows graphs of the percentage of bacteria with 2 or more germ tubes, as a function of total hyphal length.

When grown on MMM, we observe that a much lower percentage of Δ*scy* and Δ*scy-filP* mutant bacteria produce two germ tubes. Around half of Δ*scy* spores develop only a single germ tube, even after prolonged growth. However, on SFM, the Δ*scy* spores appear to develop two germ tubes faster than the wild-type, though the difference between them is much less pronounced than it is on MMM.

For the wild-type, at THL less than 150µm (younger samples), we observe a lower percentage of bacteria with 2 or more germ tubes on SFM than on MMM. At higher THL (older samples), we observe around 80% of bacteria with 2 or more germ tubes on MMM and around 90% on SFM. Therefore, it appears that the wild-type bacteria is slower to initiate a second germ tube on SFM than it is on MMM, but that it does do so eventually. A similar phenomenon is observed with the Δ*filP* bacteria. There may be an advantage in initiating a second germ tube earlier in poorer media because the new germ tube would provide less competition for scarce nutrients around the site of the initial germ tube than would a lateral branch. Additionally, a second germ tube heading in an opposite direction would enable the search for richer nutrients to be broadened.

Our software detected a number of instances of 3 and 4 germ tubes from a single spore (Table 5.4). As discussed in Chapter 2, there is some disagreement in the

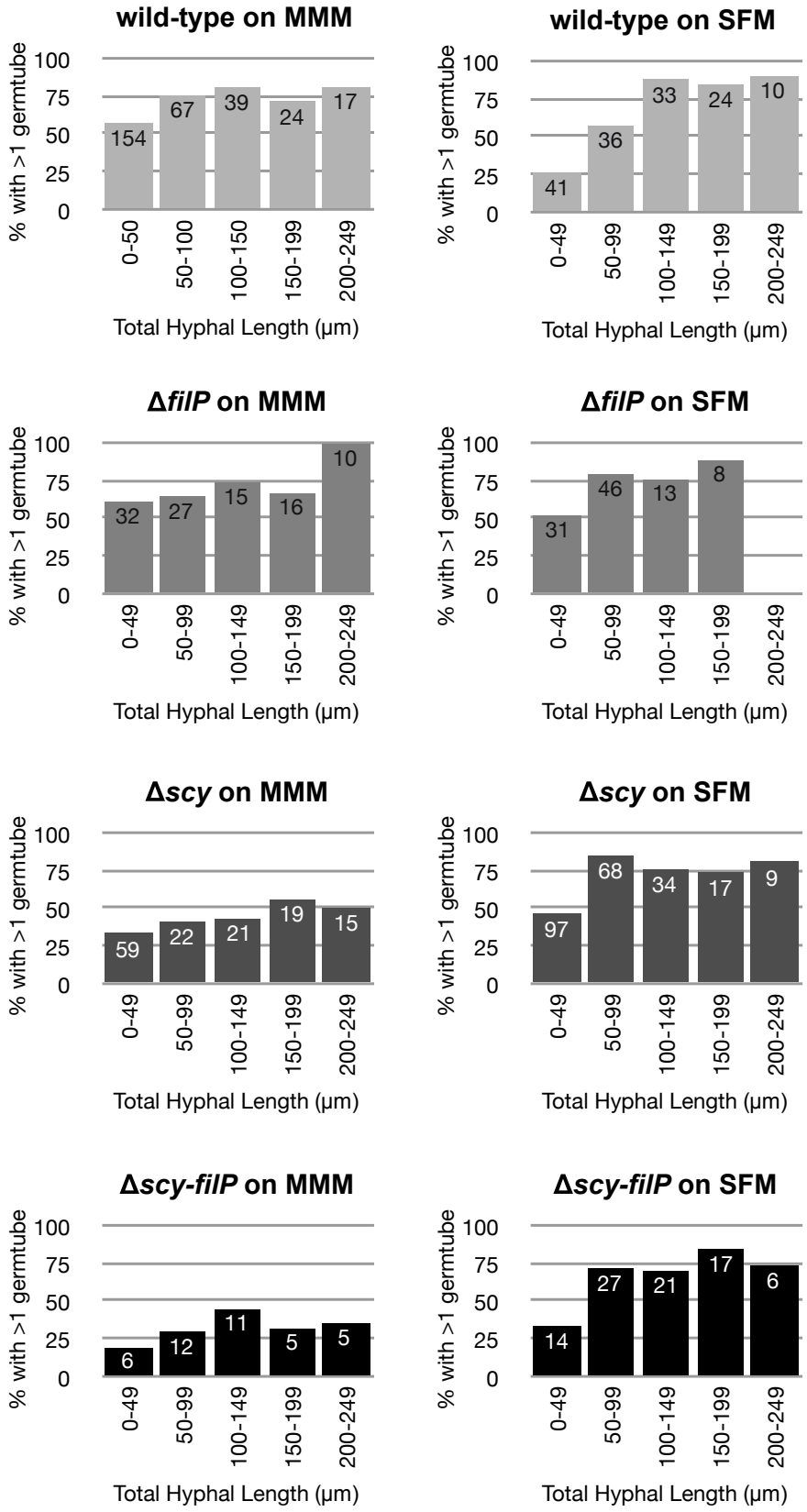

Figure 5.7: Graphs showing the percentage of bacteria with 2 or more germ tubes at given total hyphal lengths. The numbers in each bar show the number of bacteria of the given length represented by the bar.

		% of bacteria (count) with			
Bacteria	Media	1	2	3	4
wild-type	MMM	32.54 (177)	64.71 (347)	2.76 (20)	0.00 (0)
wild-type	SFM	48.44 (140)	48.44 (140)	3.11 (9)	0.00 (0)
Δ*filP*	MMM	29.81 (48)	68.94 (111)	1.24 (2)	0.00 (0)
Δ*filP*	SFM	29.73 (44)	66.22 (98)	4.05 (6)	0.00 (0)
Δ*scy*	MMM	56.43 (215)	41.21 (157)	1.84 (7)	0.52 (2)
Δ*scy*	SFM	37.36 (136)	55.22 (200)	6.87 (26)	0.55 (2)
Δ*scy-filP*	MMM	64.34 (92)	35.66 (51)	0.00 (0)	0.00 (0)
Δ*scy-filP*	SFM	35.92 (51)	55.63 (79)	8.45 (12)	0.00 (0)

Table 5.4: Table showing percentage (with actual count in brackets) of bacteria with 1, 2, 3 and 4 germ tubes.

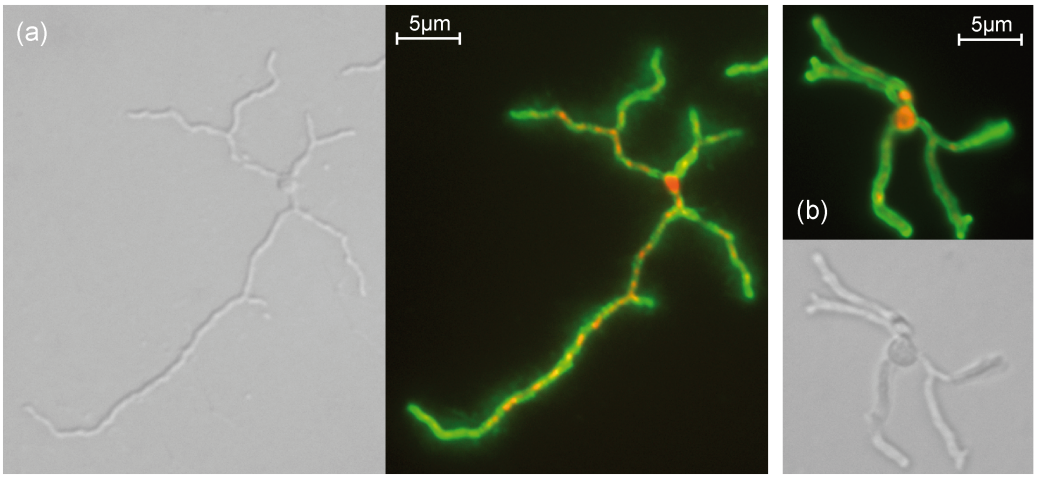

Figure 5.8: DIC and fluorescent images of spores with 3 and 4 germ tubes: (a) wild-type on MMM, with 3 germ tubes. (b) Δ*scy* on SFM with apparently 4 germ tubes.

published literature as to whether more than 2 germ tubes are ever formed in *S. coelicolor*. We reviewed the specimens in our dataset flagged as having 3 or 4 germ tubes and, whilst some may simply be early branches on existing germ tubes, it does appear that there are some circumstances (around 2%) where 3 germ tubes form in the wild-type (Figure 5.8a). Significantly, in the Δ*scy* and Δ*scy-filP* mutants, we found possible cases of 4 germ tubes (Figure 5.8b), while the overall percentage of spores with 3 or 4 germ tubes in these mutants is over twice that of the wild-type.

5.9 Apical branching

As described in Section 4.4.3, we identify apical branches by looking for two or more emerging branches, which share the same branch point. Figure 5.9 provides graphs

showing the number of apical branches as a percentage of all emerging (less than 2 µm) branches and Table 5.5 provides summary data.

It is generally understood that wild-type *S. coelicolor* only branches sub-apically. Although our data lists apical branching percentages of up to 6% for the wild-type, we believe the majority of these are simply branches close to the tip that are misidentified. We therefore see insufficient evidence to reassess the orthodoxy. However, with the Δ*scy* and Δ*scy-filP* mutants, there does appear to be a significant amount of apical branching which becomes apparent when grown on SFM (Figure 5.10). It seems likely that the *scy* gene has some involvement in the selection of branching sites and one of the effects of its removal is the apical branching behaviour we have observed.

5.10 Emerging tips

Newly emerging tips are located according to the algorithm given in Section 4.4.2, in which we defined the following two symbols (Figure 4.9):

- L_t is the distance from the site of the emerging child tip to the tip of the parent filament.
- L_b is the distance from the site of the emerging child tip to the previous branch of the parent filament.

We now introduce two further measures:

- L_{tb} is the distance from the parent filament tip to the previous branch, equal to $L_t + L_b$.
- R_{tb} is the ratio L_t/L_{tb} and provides a measure of how far along the parent filament a new filament emerges.

Figure 5.11 shows histograms of L_{tb}. This provides an indication of the length that tip segments reach before a tip forms somewhere along the length. Table 5.6 provides chi-squared comparisons between the histogram distributions on MMM and SFM, suggesting statistical significance in each case. Table 5.7 provides a summary of mean values and standard error. The table also provides values for the longest

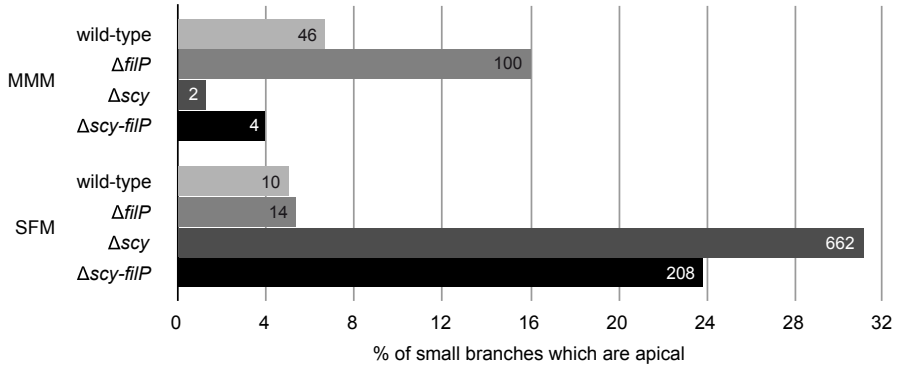

Figure 5.9: Graphs of apical branches as a percentage of newly emerging branches. The percentage scale is chosen to allow easy comparison, while figures within bars indicate the number of branches represented by the bar.

Bacteria	Media	Total no. of branches	No. of emerging branches	No. of apical branches	Apical % of all branches	Apical % of emerging branches
wild-type	MMM	2087	682	46	2.20	6.74
wild-type	SFM	1086	197	10	0.92	5.08
Δ*filP*	MMM	1279	625	100	7.82	16.00
Δ*filP*	SFM	776	260	14	1.80	5.38
Δ*scy*	MMM	1005	151	2	0.20	1.32
Δ*scy*	SFM	3370	2125	662	19.64	31.15
Δ*scy-filP*	MMM	473	100	4	0.85	4.00
Δ*scy-filP*	SFM	1440	873	208	14.44	23.83

Table 5.5: Summary table for apical branching data, giving total numbers of branches, numbers of apical branches and percentage of apical branches.

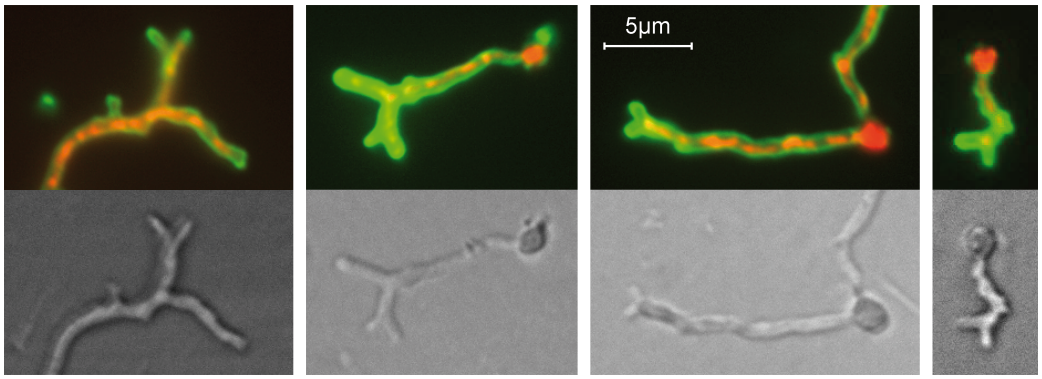

Figure 5.10: Example images of apical branching: Fluorescent (top) and DIC (bottom) microscope images showing apparent apical branching of Δ*scy* mutant on SFM.

Bacteria	χ^2	degrees of freedom	two tailed p-value	Significant? ($p < 0.05$)
wild-type	25.54	6	0.0003	Yes
Δ*filP*	65.81	5	< 0.0001	Yes
Δ*scy*	734.72	11	< 0.0001	Yes
Δ*scy-filP*	176.47	10	< 0.0001	Yes

Table 5.6: Chi-squared test results for the histograms in Figure 5.11, comparing the MMM histograms with those for the same bacteria on SFM. We adopt the convention of assuming statistical significance when $p < 0.5$.

Bacteria	Media	Number of tips	Mean (µm)	Longest (µm)	95% of tips below (µm)
wild-type	MMM	492	22.16	69.13	46.71
wild-type	SFM	97	28.06	54.39	47.29
Δ*filP*	MMM	302	14.80	51.58	38.69
Δ*filP*	SFM	109	22.69	42.77	39.10
Δ*scy*	MMM	63	50.34	110.81	97.25
Δ*scy*	SFM	778	7.62	67.58	23.12
Δ*scy-filP*	MMM	57	38.82	121.12	77.62
Δ*scy-filP*	SFM	345	13.24	67.12	42.61

Table 5.7: Table showing mean distance from parent tip to previous branch, the longest distance from parent tip to previous branch, and the length below which we find 95% of measurements.

segment length found that contains an emerging tip. The significance of this is that, in our experiments, we found the tip segment never grew beyond this length without generating a new lateral branch.

For wild-type, our data shows a slightly longer mean length when grown on SFM than on MMM. The same is true for the Δ*filP* mutant. However, for the Δ*scy* mutant, we find the opposite is the case - a much shorter mean length on SFM than on MMM - and the difference between the two media is much more apparent than with the wild-type. The Δ*scy-filP* mutant displays the same behaviour as the Δ*scy* mutant, though the SFM peak is not as tall.

Figure 5.12 shows histograms of the ratio R_{tb} which gives a distribution of the location of emerging tips along the parent filament. Table 5.8 provides a summary of mean values. The graphs show significant differences in the observed distributions. For wild-type on MMM, we observe a lower probability of a tip emerging in the first and last 10%, but a relatively even distribution elsewhere. However, on SFM, there is a clear tendency for new tips to emerge towards the previous branch and away from the tip. The Δ*filP* mutant displays similar behaviour to the wild-type.

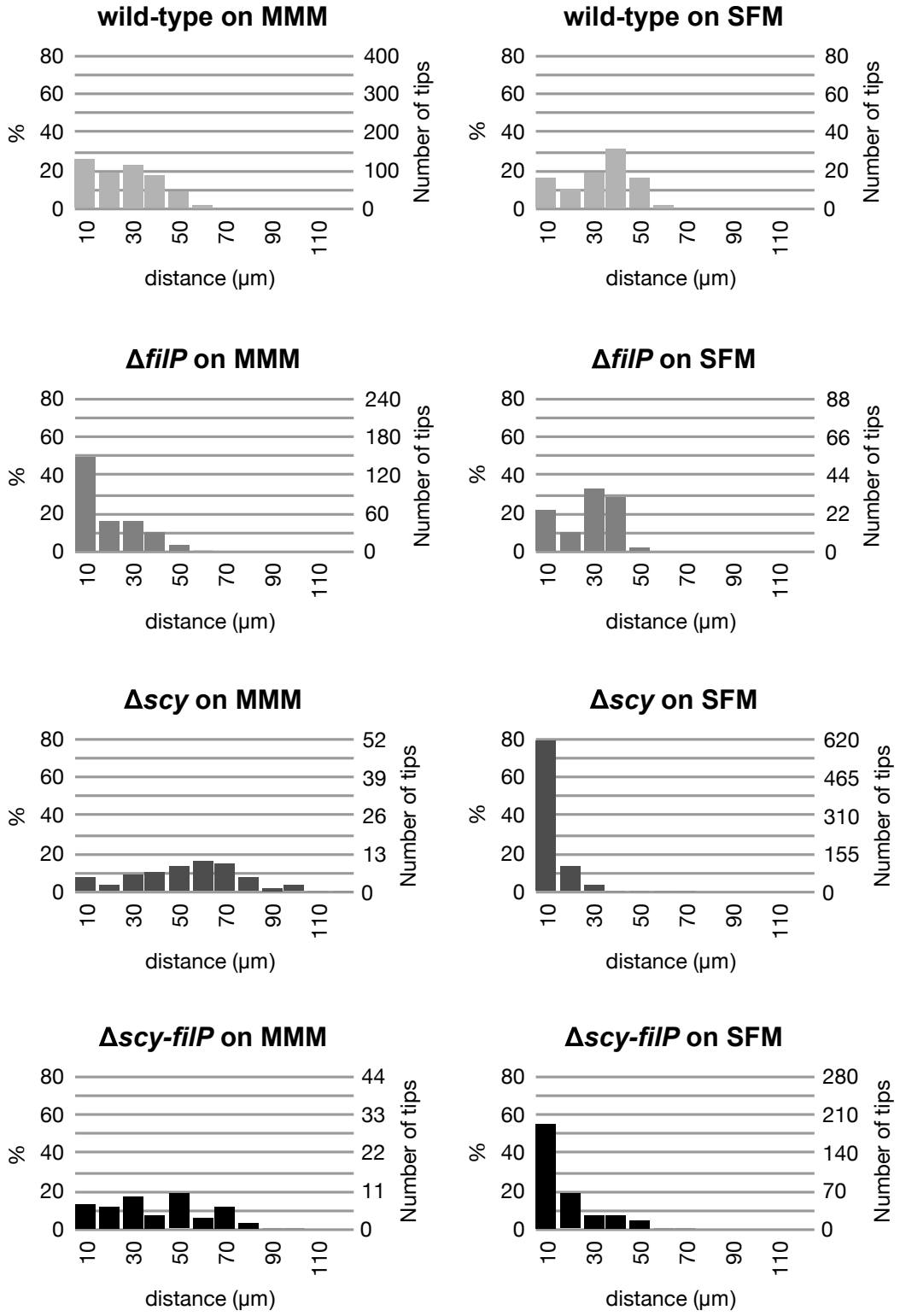

Figure 5.11: Histograms of distances from parent tip to parent previous branch point for emerging tips, with bin size 10 μm. Graphs plotted on % scale to aid comparison, with absolute counts also indicated.

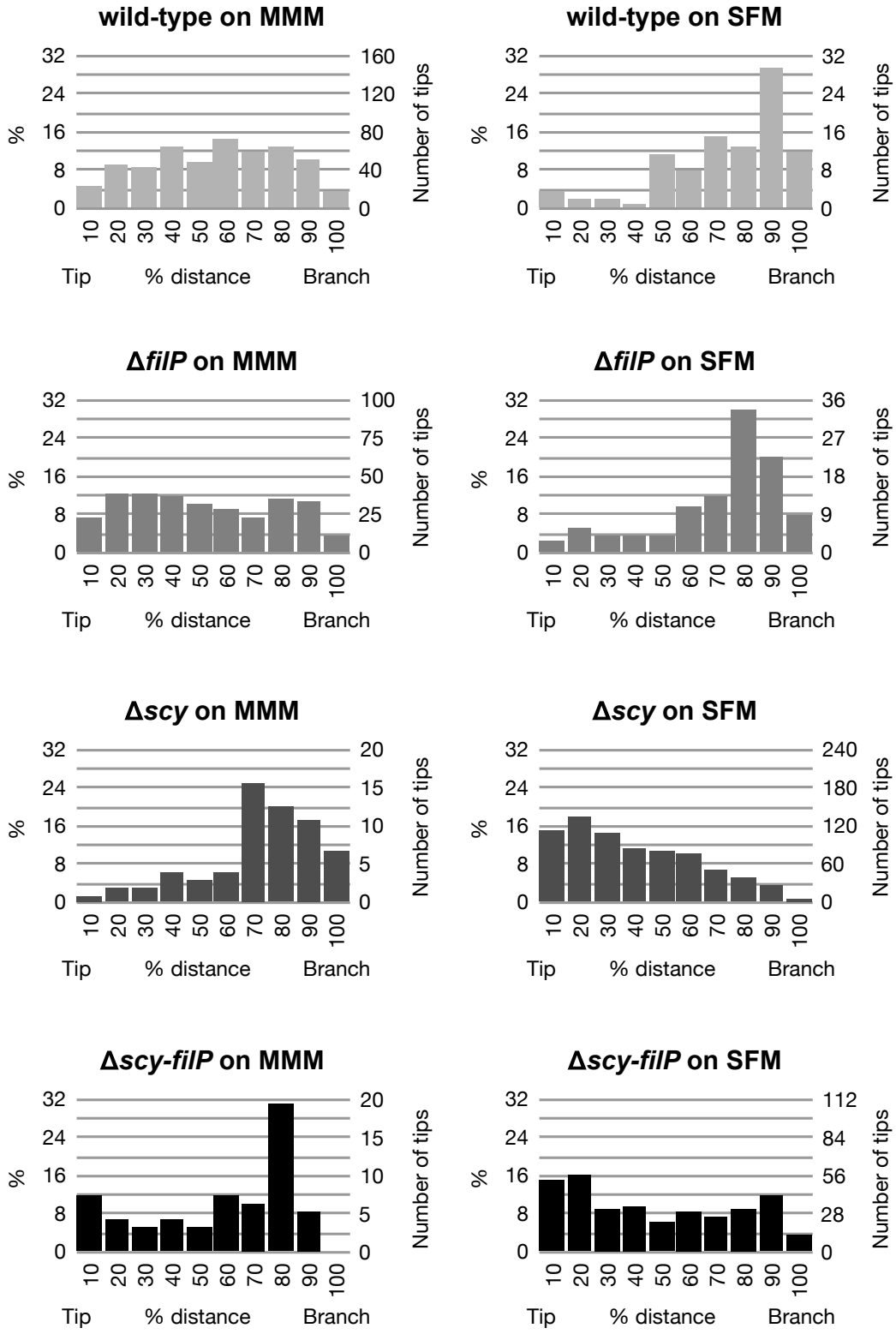

Figure 5.12: Histograms of branch position, relative to parent filament tip and previous branch points, with bin size 10 µm. Graphs plotted on % scale to aid comparison, with absolute counts also indicated.

Bacteria	Media	Number of tips	Mean (µm)	χ^2	two tailed p-value	Significant? ($p < 0.05$)
wild-type	MMM	492	51.07			
wild-type	SFM	97	68.15	82.70	< 0.0001	Yes
Δ*filP*	MMM	302	46.85	9.33	0.4074	No
Δ*filP*	SFM	109	65.74	55.22	< 0.0001	Yes
Δ*scy*	MMM	63	66.18	59.01	< 0.0001	Yes
Δ*scy*	SFM	778	36.05	50.14	< 0.0001	Yes
Δ*scy-filP*	MMM	345	43.12	50.19	< 0.0001	Yes
Δ*scy-filP*	SFM	57	53.32	38.98	< 0.0001	Yes

Table 5.8: Table showing the mean position of an emerging tip, expressed as a percentage of the distance between the previous branch and the growing tip (0=current tip, 100=previous branch). The table also provides chi-squared comparisons of the wild-type on MMM distribution and each of the other experimentally derived distributions shown in Figure 5.12. The 10 histogram bins equate to 9 degrees of freedom and we adopt the convention of assuming statistical significance when p < 0.5.

For the Δ*scy* mutant, we see a preference towards the previous branch on MMM, but a bias towards the growing tip on SFM. The Δ*scy-filP* mutant behaves similarly.

Combining the data in Figures 5.11 and 5.12, it is possible to make the following general observations.

- For wild-type grown on MMM, the majority of new tips appear when the apical filament segment is in the range 5-45µm. The new branch is equally likely to appear anywhere along the middle four fifths of the segment length.
- For wild-type grown on SFM, the majority of new tips also appear when the apical filament segment is in the range 5-45µm. However, new tips tend to be located far from the parent tip.
- For the Δ*scy* mutant grown on MMM, the apical filament section can grow quite long - up to 100µm - before new branches are initiated. New tips tend to be located far from the parent tip.
- For the Δ*scy* mutant grown on SFM, almost all tips appear when the apical filament segment is less than 20µm long and around two thirds appear at less than 5µm. The new branch is likely to appear near to the parent tip.

Histograms of the distances from emerging tips to the parent's tip and previous branch are provided in Appendix D. The appendix also contains histograms for the first emerging tip - that is, the first branch to form on the primary germ tube.

5.11 Mean depth

As described in Section 4.4.1, the organism depth provides a measure of the branching complexity of the bacteria. An organism with only primary filaments has a depth of 1, one with primary and secondary filaments has a depth of 2, and so on. Figure 5.13 provides graphs of mean depth against total hyphal length.

Though not always pronounced, there are some subtle differences between the different experiments:

- On MMM, the Δ*scy* and Δ*scy-filP* mutants display a lower mean depth (and hence lower level of complexity) than the wild-type and Δ*filP* mutants.
- On MMM, both the wild type and Δ*filP* mutant appear to display slightly higher mean depth (and hence greater complexity) than on SFM. With the Δ*scy* and Δ*scy-filP* mutants, the opposite is the case - greater depth on SFM than on MMM.

5.12 Mean distance to centre

The mean distance to centre is a measure that allows the area covered by the bacteria to be quantified so as to understand if colony observations at the macroscopic level are explained by, or mirrored in, the early microscopic growth. An alternative measure, the bounding box area, was also investigated and results for this are provided in Appendix D.

The mean distance to centre of a filamentous organism is found by calculating the mean distance from each tip to the centre of the organism. The co-ordinates of the centre of the organism, x_c and y_c are found by averaging the tip co-ordinates of the N tips:

$$x_c = \frac{1}{N}\sum_{i=1}^{N} x_i \ ,$$

$$y_c = \frac{1}{N}\sum_{i=1}^{N} y_i \ .$$

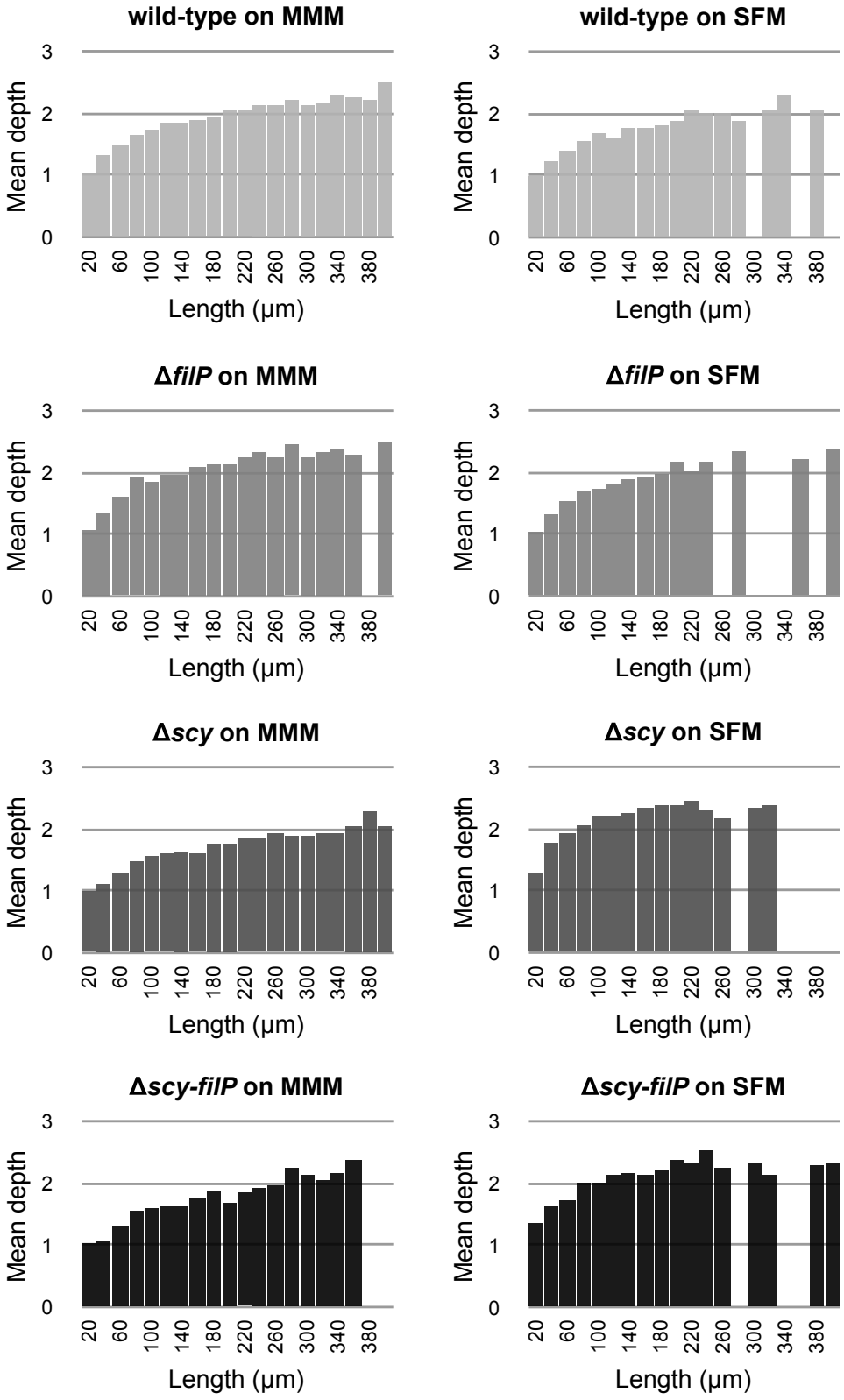

Figure 5.13: Graphs showing mean depth against total hyphal length. Missing bars indicate insufficient data available to plot.

Thus, the mean distance to centre, d_{mean} is

$$d_{mean} = \frac{1}{N}\sum_{i=1}^{N}\sqrt{(x_i - x_c)^2 + (y_i - y_c)^2} \ .$$

Figure 5.14 shows scatter plots of mean distance to centre for all bacteria. A line of best fit has been plotted according to the equation

$$y = a\sqrt{x} \ ,$$

where a is a constant for each bacteria/media combination chosen by the fitting algorithm (Table 5.9). We might expect this square root relationship because *Streptomyces* forms round colonies and the mean distance to centre can be thought of as the radius of a circular colony of area πr^2.

Figure 5.15 displays the fit lines from Figure 5.14 overlaid, allowing easier comparison of data for MMM and SFM. We note that on SFM, the Δ*scy* , Δ*filP* and Δ*scy-filP* mutants forms more compact structures than the wild-type. This difference is also apparent when the bacteria are allowed to grow to colony size (Figure 5.16). On MMM, the Δ*filP* mutant forms more compact structures than the wild-type, but the Δ*scy* mutant forms less compact structures.

5.13 Segment deviation

The segment deviation measure was created to quantify the degree of curliness observed in Δ*filP* hyphae (Section 5.3) and to understand if the other mutants also displayed this behaviour. The deviation of every segment was calculated by our software according to the method described in Section 4.4.5, which defines the deviation as the ratio of measured segment length to the Euclidian distance between the start and end of the segment. Figure 5.17 provides histograms of the segment deviations and Table 5.10 provides a summary of mean values for each experiment, as well as the percentage of segments which show a deviation below 10%.

On both MMM and SFM, we find that the Δ*filP* mutant displays a wider distribution and larger mean value for segment deviation than the wild-type. Only around

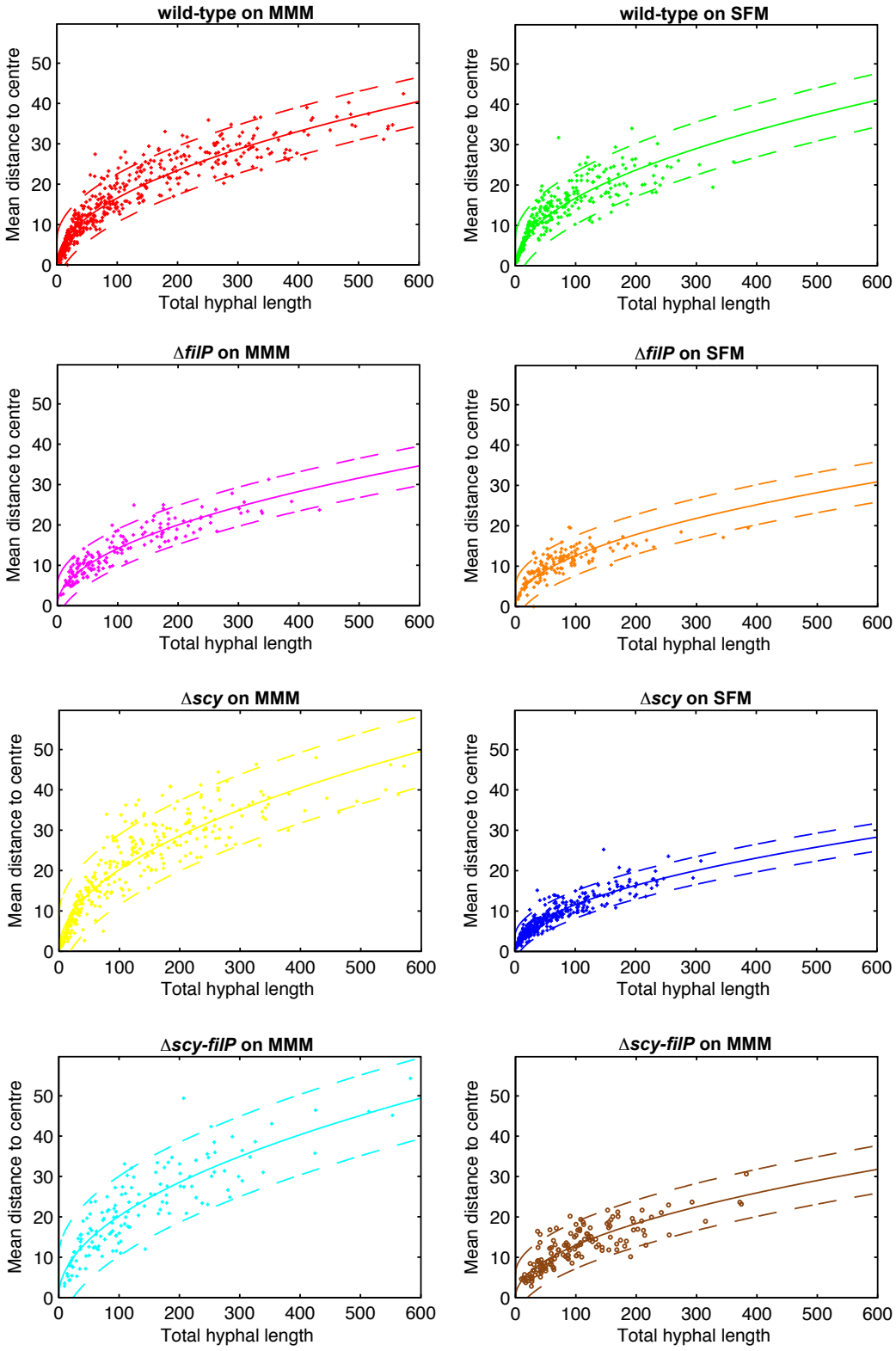

Figure 5.14: Scatter plots of mean distance to centre against total hyphal length. Solid curves are fits to the equation $y = a\sqrt{x}$, dotted lines show 95% bounds.

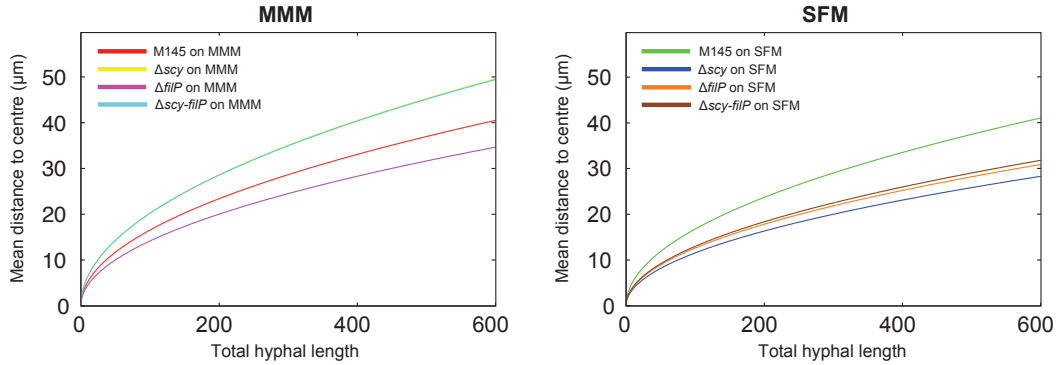

Figure 5.15: Comparison of mean distance to centre curves for MMM and SFM. Note, on MMM, the Δ*scy* and Δ*scy-filP* lines overlap.

	MMM				SFM			
	wild-type	Δ*filP*	Δ*scy*	Δ*scy-filP*	wild-type	Δ*filP*	Δ*scy*	Δ*scy-filP*
Lower bound	1.63	1.38	1.98	1.95	1.63	1.22	1.13	1.25
a	**1.65**	**1.42**	**2.02**	**2.02**	**1.68**	**1.26**	**1.16**	**1.30**
Upper bound	1.68	1.45	2.07	2.09	1.72	1.31	1.18	1.35

Table 5.9: Values for the fitting constant, a, for the distance to centre graph, as well as lower and upper 95% confidence bounds.

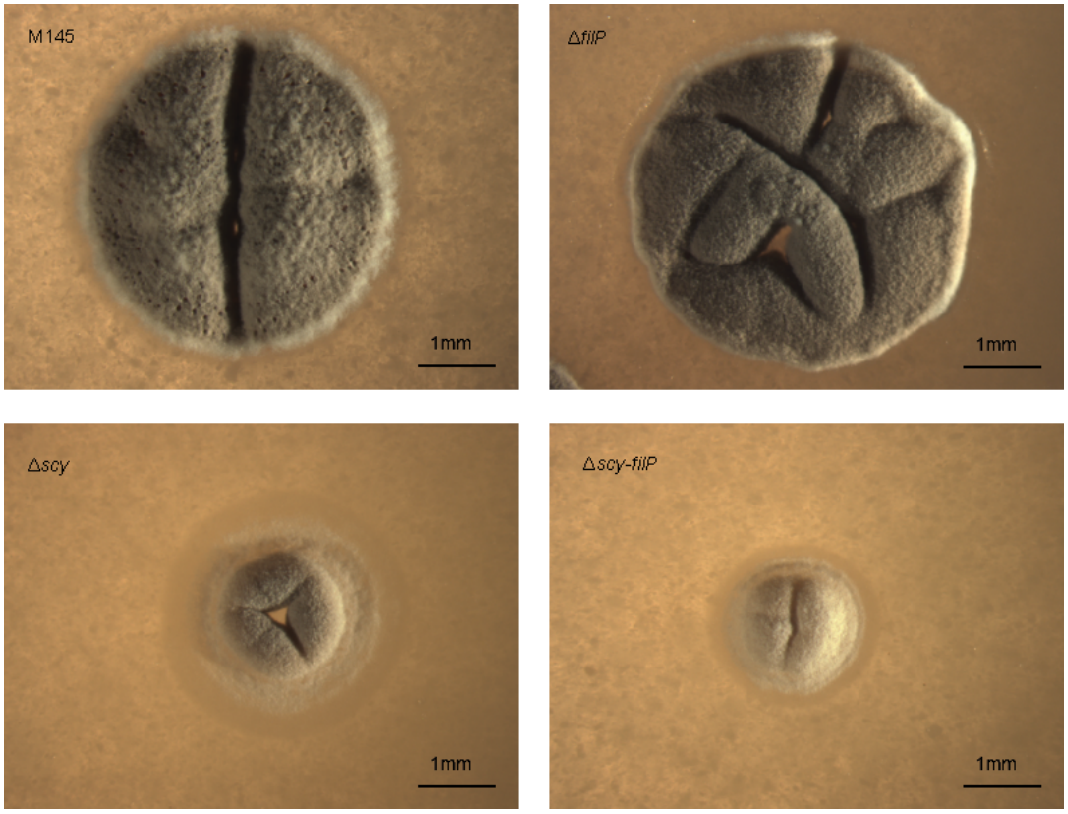

Figure 5.16: Images of colonies grown on SFM for 6 days. The Δ*scy* and Δ*scy-filP* mutants show much more compact colonies than the wild-type and Δ*filP* mutant. (Images provided by Neil Holmes)

Bacteria	Media	$\bar{d}$	% with $d < 10$	$\bar{d_n}$	% with $d_n < 2$
wild-type	MMM	8.76	74.24	2.36	74.72
wild-type	SFM	8.43	77.37	2.63	72.73
Δ*filP*	MMM	12.35	53.59	4.31	52.39
Δ*filP*	SFM	14.20	52.27	4.93	49.09
Δ*scy*	MMM	9.69	72.53	2.16	85.23
Δ*scy*	SFM	9.34	72.38	5.67	42.57
Δ*scy-filP*	MMM	10.07	73.09	2.06	84.69
Δ*scy-filP*	SFM	9.97	70.10	5.20	46.57

Table 5.10: Summary table for segment deviation: $\bar{d}$ is the mean segment deviation percentage, $\bar{d_n}$ is the normalised mean segment deviation percentage.

50% of segments have a deviation under 10% for Δ*filP* , compared with around 75% of segments in the wild-type. This indicates that the Δ*filP* segments are not as straight as the wild-type, something that supports the qualitative observation in Section 5.3 and in [4].

The deviation behaviour of the Δ*scy* and Δ*scy-filP* mutants is similar and seems unaffected by medium. Both have a mean deviation of 9-10% and around 70% of segments display a deviation below 10% on both media. This is only a slightly higher mean deviation than the wild-type, which is perhaps surprising given the relatively disturbed morphology of Δ*scy* on SFM. We wondered if the lower segment lengths of Δ*scy* on SFM could be obscuring an instability in the straightness of segments. We therefore decided to calculate the normalised deviation - that is, the deviation per unit length. This is achieved by simply dividing each segment deviation by the measured length of the segment. A histogram of normalised deviations is provided in Figure 5.18, with summary values in Table 5.10.

As well as emphasising the behaviour of the Δ*filP* mutant, the normalised data shows that the Δ*scy* and Δ*scy-filP* mutants do indeed display different behaviour on SFM than to the wild-type on either medium. If segments were able to grow to the length of wild-type segments, the data suggests they would display greater levels of deviation than the wild-type filaments. This could be indicative of instability in the hyphal wall or in the mechanisms of tip polarity.

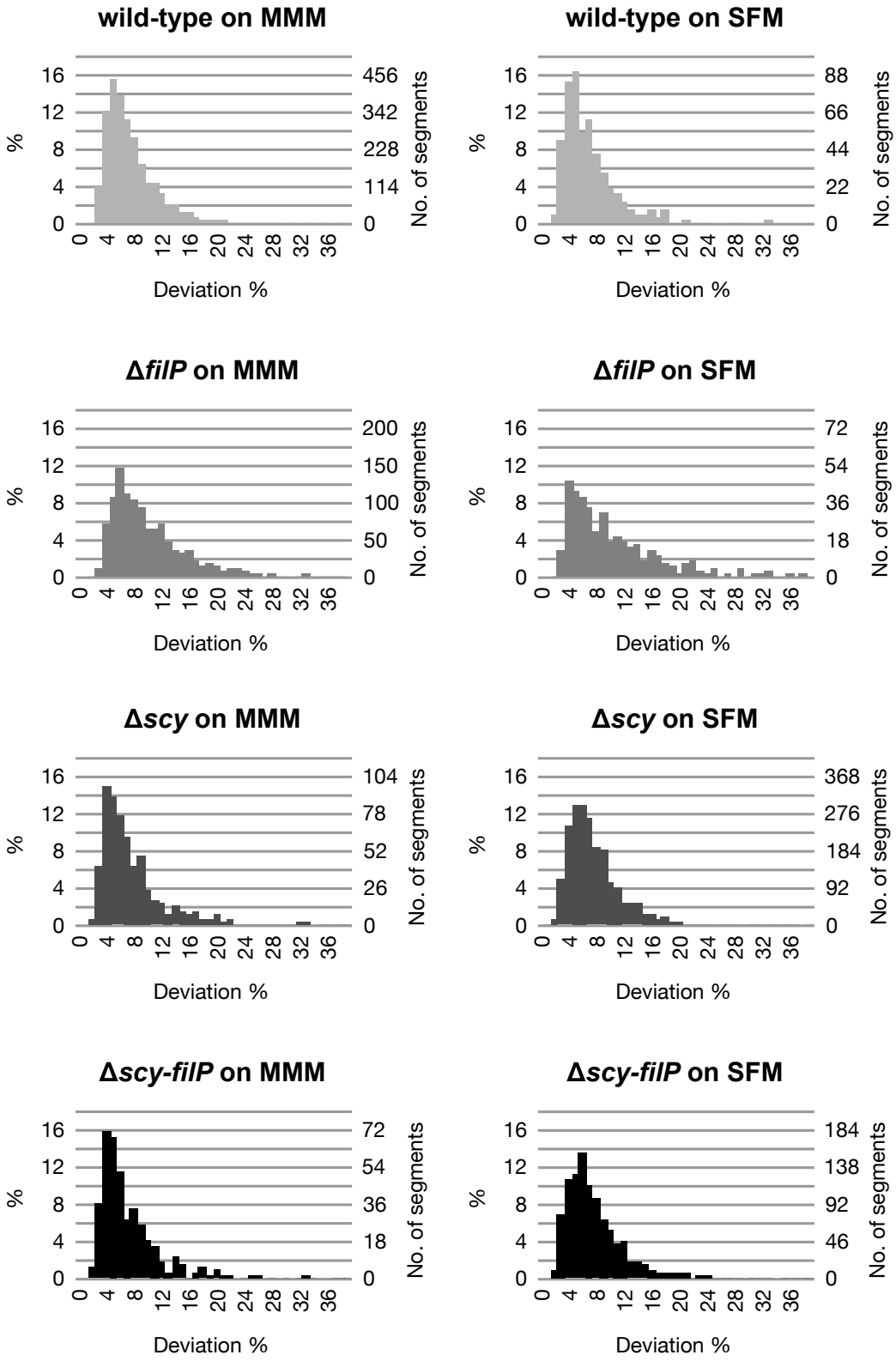

Figure 5.17: Histograms of segment deviation, created using all internal segment length measurements. The deviation is expressed as a percentage of the Euclidian distance. Thus a segment with a deviation of 10% is 1.1 times the length of the Euclidian distance between the two ends of the segment.

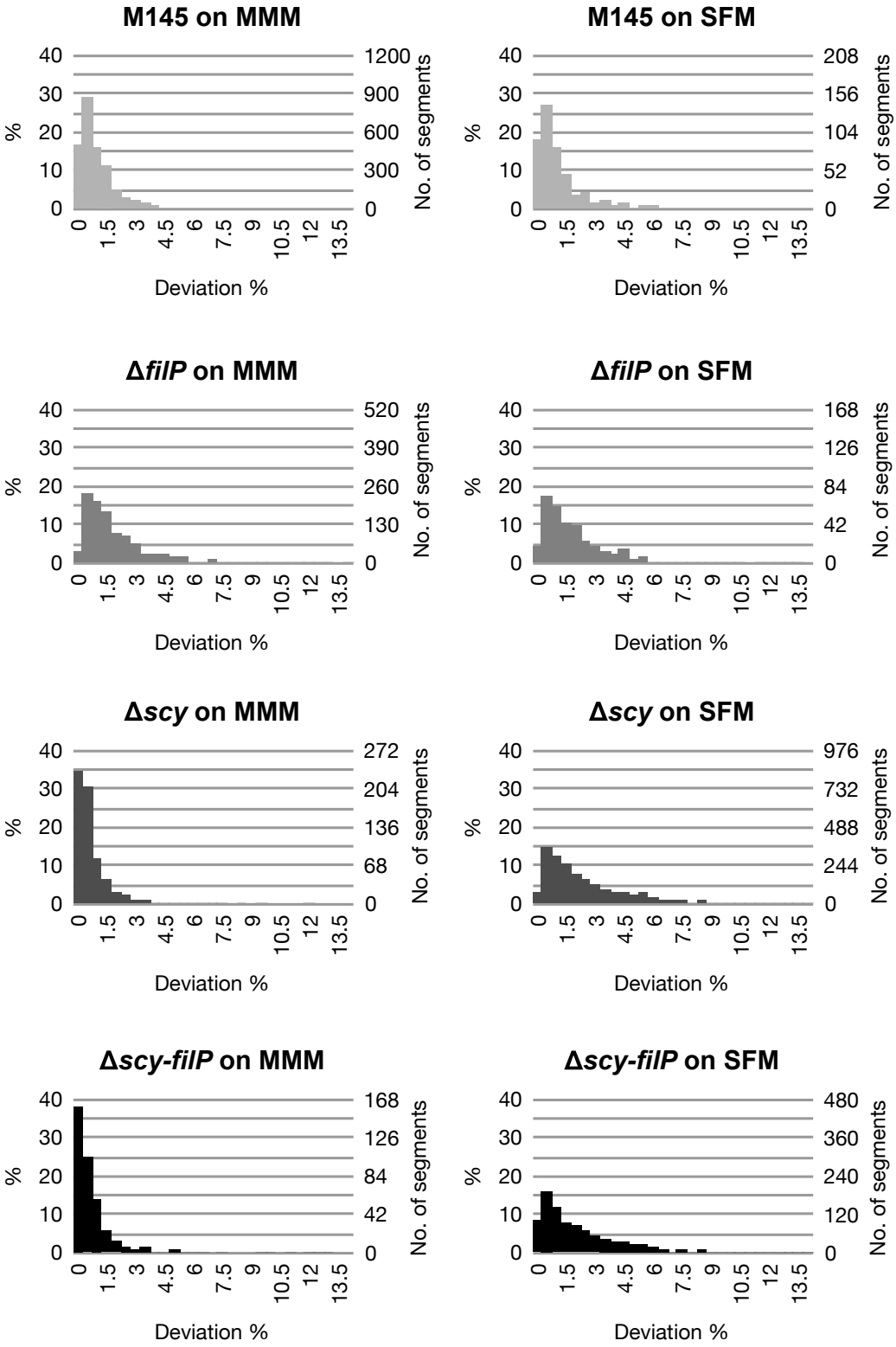

Figure 5.18: Histograms of normalised segment deviation, created using all internal segment length measurements. To normalise, each segment's calculated deviation percentage is divided by the length (in µm) of the segment.

Bacteria	Media	Mean (µm)	χ^2	two tailed p-value	Significant? ($p < 0.04$)
wild-type	MMM	43.83			
wild-type	SFM	29.56	31.98	0.7431	No
Δ*filP*	MMM	29.40	32.52	0.7205	No
Δ*filP*	SFM	21.59	94.52	0.0001	Yes
Δ*scy*	MMM	48.51	4.96	1.0000	No
Δ*scy*	SFM	17.01	190.43	0.0001	Yes
Δ*scy-filP*	MMM	49.33	18.85	0.9961	No
Δ*scy-filP*	SFM	22.66	100.88	0.0001	Yes

Table 5.11: Summary table for pairwise distance histograms, showing mean distance and chi-squared comparisons between the wild-type on MMM distribution and each of the other experimentally derived distributions. For the chi-squared test, the number of bins equates to 38 degrees of freedom and we use the convention of assuming statistical significance when $p < 0.5$.

5.14 Pairwise distances

For a given bacteria, the pairwise distance histogram is obtained by measuring the Euclidian (straight line) distance from each tip to every other tip (Section 5.14) and plotting a distribution of these values. The histograms of all samples within a dataset are combined to produce an overall histogram for a given bacteria growing on a given media. Such histograms provide a glimpse into the overall compactness of the bacterial morphology. A tall, narrow, peak at short lengths indicates tips are close to each other and segment lengths are small, while a wider peak indicates a range of segment lengths and tips not as closely spaced. Figure 5.19 shows histograms for all bacteria/media combinations and Table 5.11 provides summary data.

The graphs indicate that all the bacteria formed more compact colonies on SFM than on MMM - shown by a narrower peak towards the lower end of the graph. This result provides support for the observations reported in Chapter 2 that *Streptomyces* branch less frequently in poorer media, as their tips search out richer sources of nutrients [61]. For the Δ*scy* mutant, we see a slightly more spread out morphology than the wild-type on MMM, but a more compact morphology on SFM, something which we would expect given the segment length data in Section 5.7.

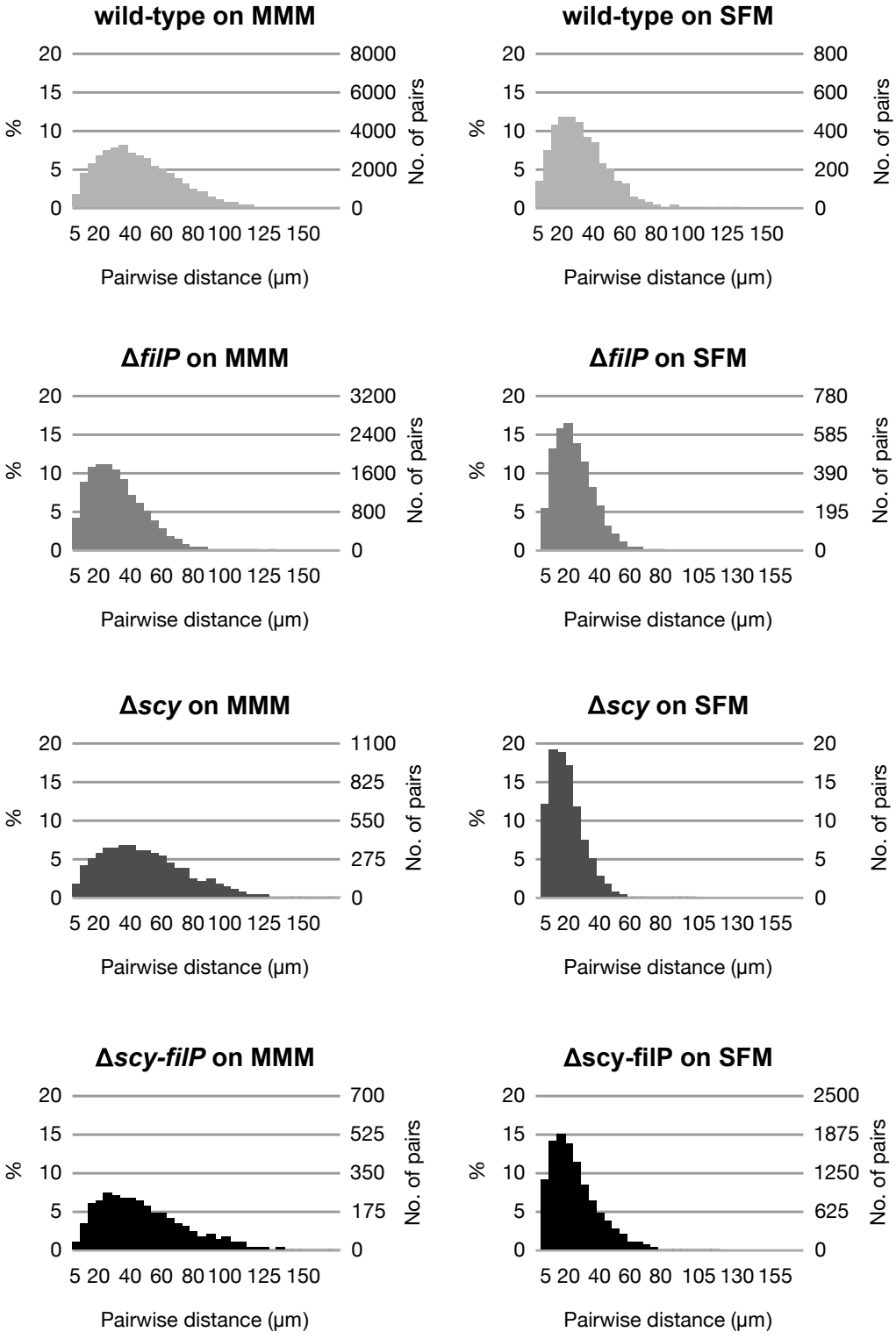

Figure 5.19: Histograms of pairwise distances, with bin size 5 μm.

5.15 Discussion

Though some attempts at quantitive analysis of the early growth and morphology of wild-type *S. coelicolor* have been reported in the past, we believe the work presented here represents the most comprehensive work to date. As well as quantifying the morphology of the wild-type, we have analysed three cytoskeletal mutants with the aim of shedding light on the function of the *scy* and *filP* genes.

Our experimental results have demonstrated that the removal of the *scy* gene has a significant effect on the morphology of *S. coelicolor*. The results show that the removal of the *filP* gene also has a noticeable effect, but it is much less significant than the removal of *scy*. Thus, we find that for many metrics, the wild-type and the Δ*filP* mutant display similar profiles and the Δ*scy* and Δ*scy-filP* mutants also display similar profiles.

The differences in the morphologies of the wild-type and mutants are most apparent when the bacteria are grown on SFM media. Here, we find that the Δ*scy* mutant forms much more compact structures than the wild-type, with more frequent branching and hence shorter segment lengths. The relative positioning of branches varies considerably between the Δ*scy* mutant and the wild-type. The Δ*scy* mutant also displays apical branching when grown on SFM, but not on MMM. There is evidence of curlier hyphae in both the Δ*filP* and Δ*scy* mutants, though it is more easily observed in Δ*filP* due to it's longer segment lengths.

The results contained within this chapter are interesting in and of themselves, as a quantitative description of early hyphal morphology. Some of the results provide support for observations which are apparent from manual examination of microscope images, but many are not immediately obvious and provide new morphological insights. The data is also useful as a means of assessing the ability of models to capture *Streptomyces* growth. In the next chapter, we describe three different models that we have developed to help better understand the data presented in this chapter.

Chapter 6

Modelling

6.1 Summary

In Chapters 3 to 5, we presented details of our experimental work, image processing and statistics gathering. The techniques described were used to gather a large set of experimental data and to produce a quantitative description of the early stage growth, branching and morphology of *Streptomyces coelicolor* and three knockout mutants. Of particular interest to us was the Δscy mutant, because of our group's involvement in the identification of the *scy* gene.

In parallel with the experimental work, we have created models of *Streptomyces* growth, as such models provide further insights into our experimental data and allow us to explore hypotheses about the internal mechanisms of early stage growth and branching. In this chapter, we describe the development of our models and the results they have produced to date.

The chapter begins with a review of previous work, describing published models of *Streptomyces* growth. We also describe some more general models of filamentous organisms, as well as relevant models of filamentous fungi that are pertinent to this thesis.

We then move on to describe three different models of *Streptomyces* growth which we have developed through the course of this work. The first adopts a mathematical formulation to describe the balance of three different types of hyphal element (Section 6.3). The second model uses an agent-based approach to provide a spatial

representation of *Streptomyces* growth, with a simple set of probabilistic rules used to determine growth and branching of filaments (Section 6.4). The last model is mechanistic and assumes that tip extension and branching is driven by the transport of a key wall building component which is manufactured at chromosome sites (Section 6.5).

6.2 Previous models

6.2.1 Types of Model

Though the number of specialised models of *Streptomyces* is limited, several models of filamentous fungi and generic filamentous microbes have been published. These models range in scale from models of single hyphal tips [5, 25, 79] up to models of large colony dynamics in industrial bioreactors [52, 57]. Useful reviews of models of filamentous microorganisms are provided by Bezzi and Ciliberto [7] and Nielsen [62].

In the discussion that follows, we have divided previous models into three classes. We call the first class *quantity models* because they seek to study the evolution of important quantities on the scale of a whole colony. These quantities can include the total hyphal length, the biomass, or the ratios of different types of hyphal element. As such, these models do not seek to provide a spatial representation of the developing mycelia.

The second class of models is those that deal solely with tip extension or tip shape. These models are not concerned with septation or branching, but seek only to model the chemical or mechanical processes involved in the extension of tips. This class includes models of 3-dimensional tip shape, as well as 1-dimensional and 2-dimensional models of the growth of individual hyphae.

The final class of models are those that attempt to model whole colonies, including tip extension and branching. These models are often implemented as simulations that provide a spatial representation of the development of the colony over time.

6.2.2 Quantity models

Nielsen [61] describes a two-part model of filamentous growth composed of what the author calls a morphology part and a population part. The morphology part identifies three morphological forms - apical cells, sub-apical cells and hyphal cells - and provides a set of equations to describe the processes of transition from one form to another within a filament. The population part is based around three differential equations describing the average properties of the hyphal elements. These are:

- The hyphal element balance - or rate of change of total number of hyphal elements with time.
- The hyphal mass balance - or rate of change of average hyphal mass with time.
- The balance for actively growing tips - or rate of change of number of actively growing tips with time.

The model is applied to the simulation of fungi and also to *Strepromyces hygroscopicus* grown in liquid culture. In the later case, model parameters were fitted to previously published experimental data. Simulation plots of hyphal growth unit length, hyphal growth unit volume and hyphal diameter are compared favourably with the experimental data.

Liu *et al.* build on the Nielsen model in order to apply it to industrial fermentation processes [52]. They note that an advanced culture of filamentous microorganisms contains several types of hyphae. Examples are newly formed hyphae containing only the apical compartment, small hyphae containing the apical and subapical compartment, old hyphae that contain only the hyphal compartment. Each of these different types of hyphae display different modes of growth and rate of metabolism. The authors modified the morphological component of Nielsen's model in order to take account of these different types of hyphae.

The final model, which incorporates branching, substrate consumption and product formation, is used to simulate the batch fermentation process of streptomycin production. The model predicts high-level time-based parameters, such as mycelial concentration, substrate concentration and product concentration, but, like Nielsen's

model, does not provide for spatial modelling or graphic representation of the growing organism.

Other related models of fungal growth include those of Christiansen *et al.* [12], Ferret *et al.* [16] and Grimm *et al.* [30].

6.2.3 Models of tip extension

Goriely and Tabor [25] describe a model of *Streptomyces* tip growth in which the cell wall is modelled as a stretchable and growing elastic membrane. The model only captures tip shape, without considering sporulation, branching or septation, but it is able to recreate realistic, experimentally observed, 3-dimensional tip profiles.

In fungi, the Vesicle Supply Centre (VSC) model of Bartnicki-Garcia *et al.* [5] has gained much support. This model proposes that vesicles (self-contained packages of wall building material) are manufactured throughout the hyphae and transported first to the Spitzenkörper (described in Section 2.3), which acts as an organisational hub. From here, vesicles are released to fuse with the cell membrane at the site of the growing tip. A number of computer implementations of this model in 2-dimensions [5] and 3-dimensions [22, 81] have been published. These provide visualisations of the growing tip, but are not yet able to model complete branching filamentous structures. Such a model does not easily transfer to *Streptomyces* because, as it is currently understood, it has no Spitzenkörper or vesicles. However, it is conceivable that there are other mechanisms of tip organisation and wall building material transport which parallel the fungal mechanism.

Sugden *et al.* describe a 1-dimensional model of hyphal growth (but not branching) of filamentous fungi [79], which models vesicle transport to the tip with the use of a statistical mechanical method called Totally Asymmetric Simple Exclusion Process (TASEP). In this model, the filament is pictured as a lattice of sites which can be either occupied or empty. Particles hop in one direction, without overtaking, towards the tip and once at the tip, they act to extend it. The model is able to capture in a limited way some of the observed growth properties of the fungus *Neurospora crassa*.

6.2.4 Models of colonies

Yang *et al.* describe a colony model composed of a deterministic part and a random part, which they applied to fungi and bacteria [85]. The deterministic part models hyphal tip extension and septation, while branching is modelled as a random process. The key components of the model are as follows:

- Tip extension is assumed to be driven by a 'key component' which is produced along the hypha and diffuses towards the tip. The tip extends by an amount proportional to the flow of the key component into the tip.
- Septation is modelled as a process that depends on the amount of nuclear material in a segment - once this reaches a critical concentration, septation occurs and the segment is divided. The key component is unable to flow through septa boundaries.
- Choice of branching sites is random, but normally distributed around septa with predetermined standard deviation. Branching is timed to occur after septation with a delay set to be a normally distributed random value.

The authors were able to apply their model to grow 2-dimensional virtual bacteria. Values for the thirteen model parameters were obtained from previous experimental data for *S. tendae* published in the PhD thesis of Reichl (1990). Plots of total hyphal length and number of branches against time show close fits between simulation and experimental data, though this is perhaps unsurprising considering the model parameters include experimentally derived values for linear extension rate and branching parameters.

At the largest scale, filamentous organisms may produce pellets - densely packed networks of hyphae. Meyerhoff *et al.* describes a pellet growth model [57], based on the earlier work of Yang *et al.* [85] and applied to the fungus *Penicillium chrysogenum.* The model is extended to take into account substrate limitations, oxygen depletion and shearing effects - these are not significant effects in younger mycelia, but become much more important factors when considering pellet morphology.

Laszlo and Silman describe a set of simple cellular automata models of fungal growth which produces realistic growth patterns at a macroscopic level, without

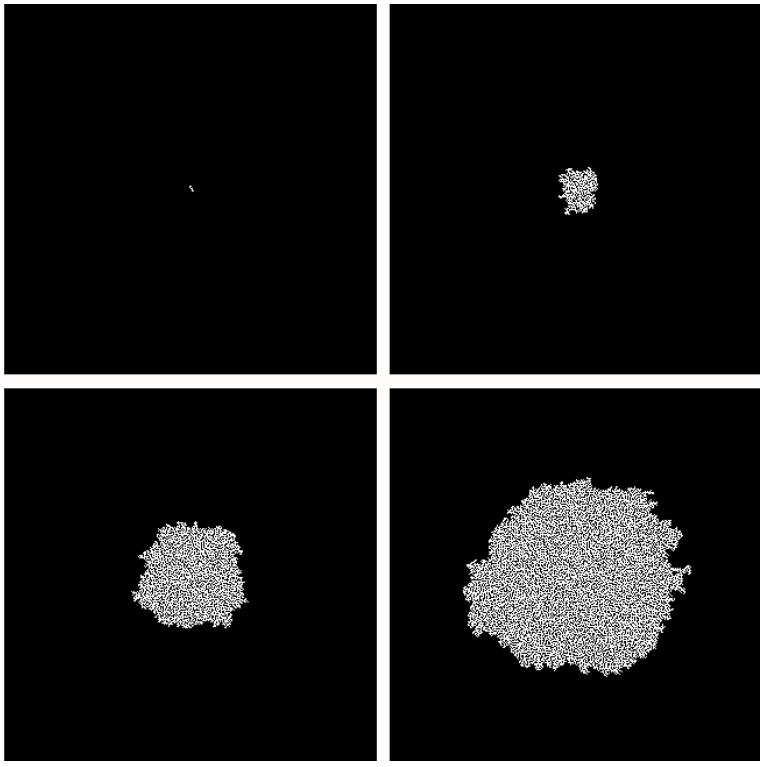

Figure 6.1: Frames from a single run of our own implementation of the Laszlo and Silman cellular automata, reported in [48].

modelling individual hyphae [48]. The model represents the growth medium as a two-dimensional grid of squares which can be either occupied or unoccupied. In the simplest version of the model, at each tick of the clock, every unoccupied square in the grid is evaluated according to a set of probabilistic rules which are dependent on the number of neighbours in the 8-neighbourhood around the square:

- If there is 1 neighbour, then there is a $\frac{1}{8}$ probability that the empty square will become occupied.
- If there are 2 neighbours, then there is a $\frac{1}{4}$ probability that the empty square will become occupied.
- If there are 3 neighbours, then there is a $\frac{1}{2}$ probability that the empty square will become occupied.
- If there are 4 or more neighbours, the square is considered overcrowded, so there is a 0 probability that it will become occupied.

Using this very simple set of rules, surprisingly realistic looking colonies emerge. Figure 6.1 shows the results of our own implementation of this model.

The authors suggest a number of modifications to increase the sophistication of the model:

- Ageing can be introduced by making unoccupied sites which border occupied sites unavailable for expansion after a while. This could be used as a way to model nutrient depletion or growth inhibitors.
- The initial model allows simultaneous growth on multiple empty sides, which is unrealistic. The authors introduce a concept from particle physics cellular automata models, where unoccupied sites cycle through eight stages representing the eight directions of growth. Only when the direction of the unoccupied site matches that of its occupied neighbour can the empty site become occupied.
- The idea of spore production is implemented by allowing the occupied sites to move through a number of states representing levels of maturity from young vegetative hyphae through to spore-producing aerial hyphae.

Other relevant models of filamentous fungi colonies include those of Lejeune and Baron [49], Moore *et al.* [59] and Soddell *et al.* [75].

6.3 A population balance model

6.3.1 Model description

One of our earliest approaches to modelling *Streptomyces* growth was to develop a non-spatial population dynamics model. In Section 6.2.2, we described some similar types of model that have been developed for fungi and, in one instance, applied to *S. hygroscopicus* grown in liquid culture. However, growth on solid media is different to that in liquid culture and *S. coelicolor* has different growth properties to *S. hygroscopicus*. In addition to these limitations, we also wanted a model which could be directly compared to our experimental data.

Our model consists of a set of ordinary differential equations (ODEs) to represent the balance of three types of hyphal element:

- Growing hyphal tips, T.
- Stable subapical hyphal segments which will not exhibit lateral branching, W.

- Subapical hyphal segments which could either become a new lateral branch or become a stable hyphal segment, P.

We assume each tip grows at the same constant velocity, v, so that the rate of change of colony length L is given by

$$\frac{dL}{dt} = vT \ .$$

Integrating this equation with respect to t gives

$$L = \int_0^\tau vT(t)\mathrm{d}t \ .$$

Now, there are two types of transition that occur as the organism grows:

- P-to-T transitions occur when P-type segments (the subapical segments) turn into T-type segments (growing hyphal tips) because of the initiation of a new lateral branch.
- P-to-W transitions occur when P-type segments turn into stable W-type segments, either because of age or because of lateral branches initiated closer to the tip.

We define c to be the P-to-T conversion rate and α to be the P-to-W conversion rate. We also introduce a tip death rate, d. Using these definitions, we can define three equations for the rate of change of the three types of hyphal section:

$$\frac{dT}{dt} = cP - dT \ ,$$

$$\frac{dW}{dt} = \alpha P \ ,$$

$$\frac{dP}{dt} = vT - cP - \alpha P \ .$$

Tip death only becomes a factor in more mature colonies, where depletion of nutrients and proximity of filaments causes tips to stop growing. Because we are interested in understanding the growth of young bacteria, we set $d = 0$. We can

then obtain the following analytic expressions for T, P and W:

$$T = \frac{1}{2\sqrt{\beta}}\left[\exp\left(-\frac{1}{2}t\left[c+\alpha+\sqrt{\beta}\right]\right)\left(-c-\alpha+\exp\left(t\sqrt{\beta}\right)\left(c+\alpha+\sqrt{\beta}\right)+\sqrt{\beta}\right)\right] , \tag{6.1}$$

$$W = -\frac{\alpha}{c}+\frac{\alpha}{2c\sqrt{\beta}}\left[\exp\left(\frac{1}{2}t\left[c+\alpha+\sqrt{\beta}\right]\right)\left(-c-\alpha+\exp\left(t\sqrt{\beta}\right)\left(c+\alpha+\sqrt{\beta}\right)+\sqrt{\beta}\right)\right] , \tag{6.2}$$

$$P = \frac{1}{\sqrt{\beta}}\exp\left(-\frac{1}{2}t\left[c+\alpha+\sqrt{\beta}\right]\right)\left(\exp\left(t\sqrt{\beta}\right)-1\right) , \tag{6.3}$$

where

$$\beta = 4c+(c+\alpha)^2 . \tag{6.4}$$

Note that this model suggests that the parameters α and c should be constant across a given species of bacteria grown under specified conditions. If this were the case, we could potentially use these parameters as a means of classifying the differences between different bacterial strains.

6.3.2 Model results

We obtained values for the model parameters α and c by fitting our experimental data to Equation 6.2. For each experiment, we plotted a scatter graph of W against t and used the Matlab curve fitting toolbox [53] to find values of α and c that produced the closest fit to the data.

For each bacterium, the value for W was calculated as the sum of all internal segment lengths - that is, the total hyphal length excluding tip segments (Figure 6.2). The value to use for time, t, is less straightforward to capture - though we do record data at 2-hourly time points, the bacteria are not sufficiently synchronised to accurately know how long they have been growing. Therefore, we used the primary filament length for the x-axis, as this value is proportional to the length of time the organism has been growing and appears to be a more reliable measure.

Figure 6.3 shows an example curve fit - in this instance, for one of the wild-type on MMM experiments. Curve fits for all experiments are provided in Appendix E, while Table 6.1 provides values for α and c for all experiments, along with the 95% confidence bounds.

In order to understand the parameter space that emerged from the fitting, we

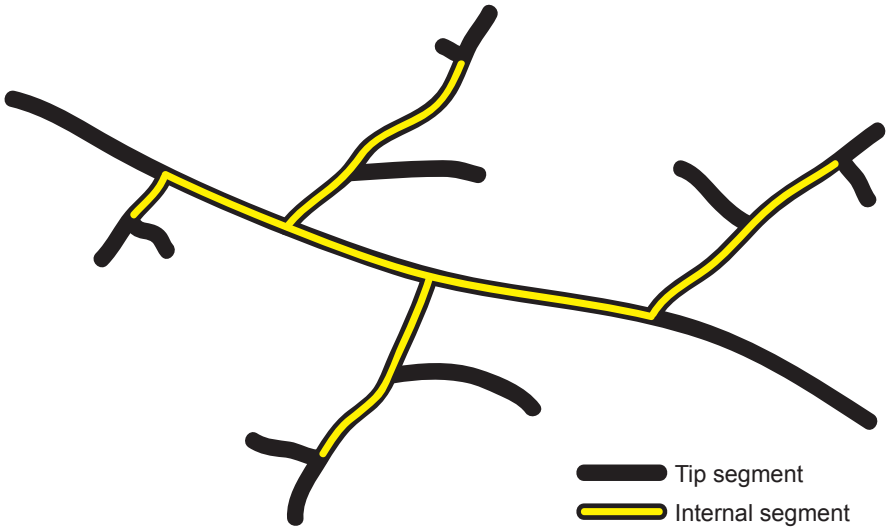

Figure 6.2: The sum of internal segment lengths includes all segment lengths apart from tip segments. In this diagram of an example bacterium, the internal segment lengths are those shaded yellow, while tip segments are entirely black.

				95% Confidence			95% Confidence	
Date	Bacteria	Media	α	Lower	Upper	c	Lower	Upper
18 Mar 08	M145	MMM	0.0297	0.0230	0.0365	0.0009	0.0008	0.0010
29 May 08	M145	MMM	0.0456	0.0317	0.0594	0.0018	0.0017	0.0019
11 Jun 08	M145	SFM	0.0080	0.0055	0.0104	0.0013	0.0006	0.0019
20 Jun 08	M145	SFM	0.0095	0.0065	0.0125	0.0020	0.0014	0.0026
29 May 08	Δ*scy*	MMM	0.0086	0.0063	0.0109	0.0008	0.0006	0.0009
2 Jul 08	Δ*scy*	MMM	0.0041	0.0032	0.0049	0.0005	0.0004	0.0006
11 Jun 08	Δ*scy*	SFM	0.2392	0.1172	0.3612	0.0240	0.0192	0.0288
20 Jun 08	Δ*scy*	SFM	2.0000	-13.3181	17.3179	0.0132	-0.0813	0.1077
2 Jul 08	Δ*scy*	SFM	0.3421	-0.0724	0.7566	-0.0001	-0.0016	0.0013
10 Jul 08	Δ*filP*	MMM	0.0646	0.0394	0.0898	0.0009	0.0008	0.0011
17 Jul 08	Δ*filP*	SFM	0.0084	0.0067	0.0100	0.0004	0.0004	0.0005
10 Jul 08	Δ*scy-filP*	MMM	0.0133	0.0097	0.0169	0.0025	0.0020	0.0031
17 Jul 08	Δ*scy-filP*	SFM	0.0690	0.0362	0.1017	0.0005	0.0003	0.0008

Table 6.1: Model fit parameters.

produced a scatter plot with α along the x-axis and c along the y-axis (Figure 6.4). If our population balance model is capable of capturing differences between the bacterial strains, we would expect to see experiments that use the same bacterial strain and medium occupying a similar area of parameter space. We would also expect to see different bacterial strains occupying different areas of parameter space.

Examining Figure 6.4, we observe that both experiments for the wild-type on SFM are located very close to each other, as are both experiments for the Δ*scy* mutant on MMM. The wild-type on MMM experiments are not quite as close together, but are still in the same region of parameter space. However, there are currently too few experiments to draw firm conclusions. Further experimental data would allow

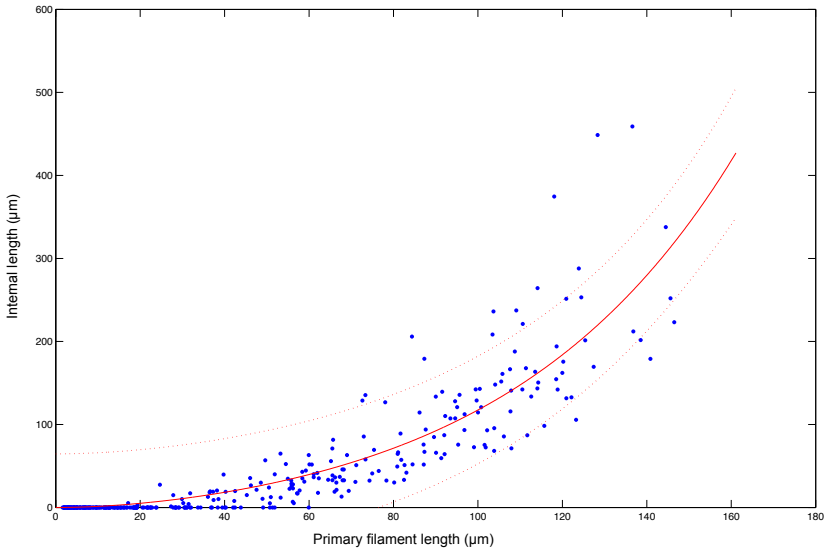

Figure 6.3: Example model fit: a graph of internal segment length against primary filament length for 18 March 2008 M145 on MMM data. Red line shows best fit curve, dashed lines show 95% confidence intervals.

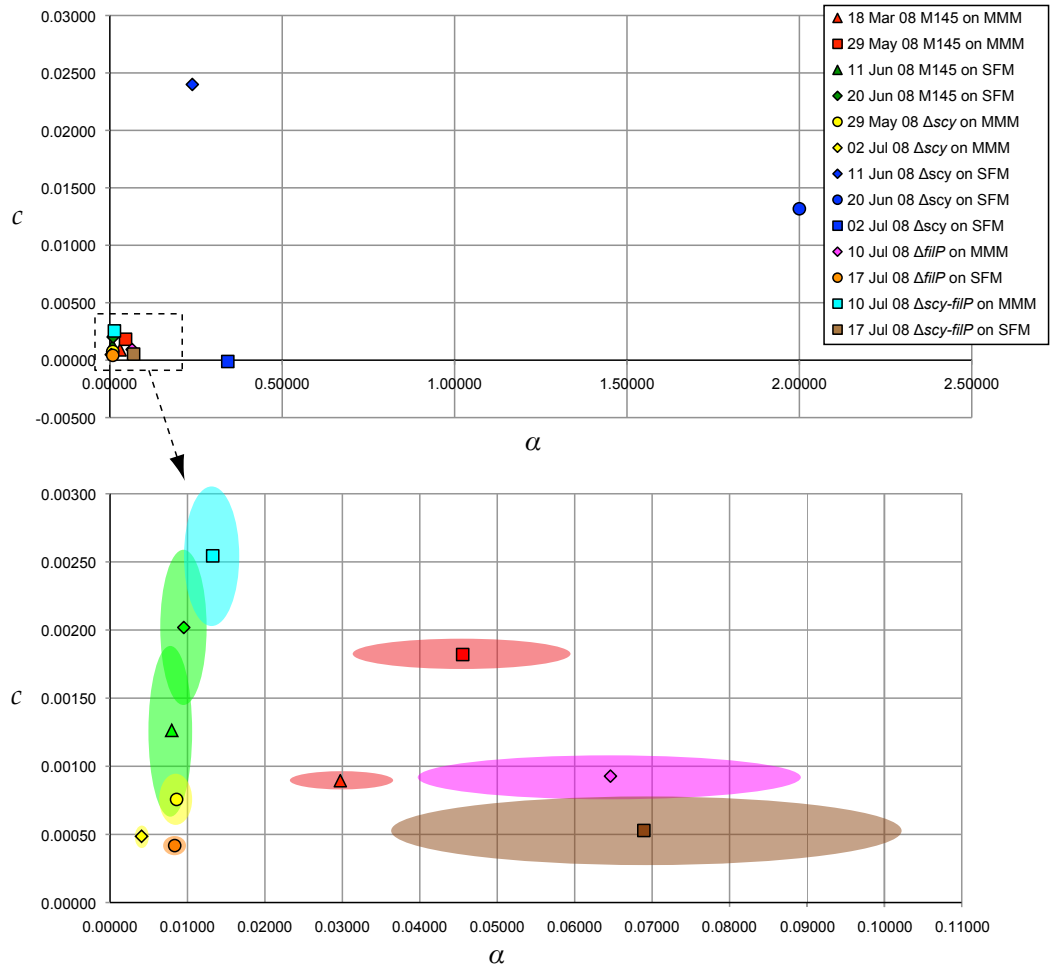

Figure 6.4: Graph of population balance model fit parameters, α and c. The bottom graph shows results for all experiments except the Δscy mutant, which can be seen in the top graph. Shaded areas show the 95% confidence bounds.

Date	Bacteria	Media	Model fit RMSE	Simple fit RMSE	Closest Fit
18 Mar 08	M145	MMM	32.83	33.30	Model
29 May 08	M145	MMM	28.87	29.29	Model
11 Jun 08	M145	SFM	6.36	6.51	Model
20 Jun 08	M145	SFM	12.88	13.00	Model
29 May 08	Δ*scy*	MMM	19.15	19.35	Model
2 Jul 08	Δ*scy*	MMM	16.65	16.81	Model
11 Jun 08	Δ*scy*	SFM	11.70	11.84	Model
20 Jun 08	Δ*scy*	SFM	22.10	21.94	Simple
2 Jul 08	Δ*scy*	SFM	15.46	15.65	Model
10 Jul 08	Δ*filP*	MMM	29.30	30.09	Model
17 Jul 08	Δ*filP*	SFM	22.14	22.38	Model
10 Jul 08	Δ*scy-filP*	MMM	14.08	14.13	Model
17 Jul 08	Δ*scy-filP*	SFM	27.46	27.42	Simple

Table 6.2: Comparison of root mean squared error between model fit and simple exponential fit.

us to determine if clusters develop, which could mean the model would have a useful role in classification of bacteria.

Perhaps surprisingly, the Δ*scy* mutant on SFM experiments are not obviously clustered together and are far apart in parameter space. Indeed, the Δ*scy* on SFM experiments are located quite some distance away from all the other experiments, having much higher values of α and c. These high values are probably a reflection of the Δ*scy* mutant's significantly increased level of branching.

6.3.3 Evaluation of model

The fact that we found that model parameters for different bacteria occupy broadly distinct parts of parameter space is encouraging. However, this in itself is not necessarily an indication of how well the model is capturing reality. To try to assess this, we fitted a simple exponential function to the experimental data and compared the fits with those obtained for our model. We used the function

$$y = \gamma(e^{bx} - 1) \ ,$$

where γ and b are constants and the curve of the function passes through the origin. We compared the root mean squared error (RMSE) of the model fit and the simple exponential fit, to see which fitted the data most closely (Table 6.2).

In all but two cases (one of the Δscy on SFM experiments and the Δscy-*filP* on SFM experiment), we found the model gave a closer fit to the experimental data than the simple function. However, the RMSE in the simple fit was smaller than we would have expected in comparison to the model RMSE. This could be because the data is so noisy that it is not possible to get a significantly closer fit for so few parameters. Adding more parameters to the model would likely produce closer fits to this experimental data, but may just end up producing a closer fit to the noise.

Instead of revising our population balance model, we decided instead to move on to examine different kinds of model. The next section describes a probabilistic agent-based model of *Streptomyces*. In some ways, it can be viewed as an evolution of the population balance model, as it captures spatially the probabilistic branching behaviour described in the population balance equations.

6.4 An agent-based model

6.4.1 Model description

Based predominantly on observation of growing bacteria, we created a probabilistic spatial model of *Streptomyces* growth using an agent-based approach. As far as we are aware, this is the first instance of agent-based techniques being applied to the modelling of filamentous microbes.

Agent-based models represent a system as a set of independent, semi-autonomous agents which operate and interact according to a precise set of rules. From these individually defined microscopic behaviours, it is possible to explore emergent macroscopic phenomena.

The concept of agent-based modelling is a loose one and there are no strict definitions of what constitutes an agent. When constructing an agent-based model of *Streptomyces* bacteria, there are a range of approaches to structuring the model. These include treating each individual septa-separated cell as an agent or treating individual sub-cellular components as agents. In our model, the agents are defined as individual filaments, with new agents created when child filaments are formed by lateral branching. Each filament obeys a set of rules which govern its nutrient

consumption, growth and branching.

We imagine our bacteria growing in a virtual Petri dish on a substrate which provides them with the nutrients needed for their extension. We define the substrate as a 2-dimensional array of pixels, with each pixel possessing a nutrient concentration ranging from 0 to 127. To start with, the substrate is populated randomly, so that each pixel has a concentration somewhere between 100 and the maximum value. Over time, as the bacteria consumes nutrients, the substrate gets depleted and the strength value falls toward zero.

Each filament agent maintains an internal list of the following:

- the pixels making up its total length;
- the co-ordinates of its tip;
- a growth rate;
- a direction of growth.

A cycle of the model involves four phases: filament extension, nutrient depletion, filament branching and germ tube initiation.

Filament extension: During the filament extension phase, each filament extends its tip by an increment equivalent to its growth rate. However, the tip does not necessarily continue in its current direction of growth. In choosing where to extend the tip, the filament examines the location one unit ahead and also 10 degrees to the left and the right of this location. The filament grows into the location where the substrate concentration is strongest and the direction of growth is then adjusted accordingly. This rule was implemented in an attempt to model the autotropism behaviour described in Section 2.3, which prevents filaments from growing into one another. We discuss whether or not this succeeded in Section 6.4.2.

If the substrate concentration is zero at all three potential growth locations, then the filament ceases growing altogether.

Nutrient depletion: Once the tip has extended, the substrate concentration at the new tip location is reduced to model the consumption of nutrients by the bacterium. We define a circle of radius r around the tip and reduce the concentration

at any location within that radius by an amount

$$\Delta S = \frac{r - d}{r} \ ,$$

where d is the distance from the centre of the circle. Thus, for example, the concentration at the centre is reduced by 1 unit, the concentration at half radius by 0.5 and the concentration at the edge of the circle by zero.

Branching: At the start of each cycle, there is a chance that a filament will begin a child branch. Assuming the filament has reached a minimum length, the model determines whether a branch will occur according to a simple probability. If a new branch is initiated, its position is chosen randomly according to a normal distribution about the central position between the current tip and the last branch. However, a branch position parameter allows the position probability function to be skewed towards the branch or the tip. The initial direction of the new branch is chosen to be perpendicular to the parent filament, but with a random variation of up to 5 degrees. The side of branch, left or right of the parent filament, is chosen randomly with equal probability either side.

Germ tube initiation: Each simulation starts with a single germ tube. However, after a minimum time has elapsed, there is a probability that a second germ tube will be initiated.

Table 6.3 provides a complete list of the model parameters. We have implemented the model in a Java application which allows adjustment of these parameters and very quick growth of virtual bacteria. Figure 6.5 shows some example runs of the model.

Parameter	Description
L_B	Minimum length before branch
α	Branch probability
b	Branch position parameter
R	Nutrient consumption radius
t_g	Second germ tube delay
γ	Second germ tube probability

Table 6.3: Agent-based model parameters.

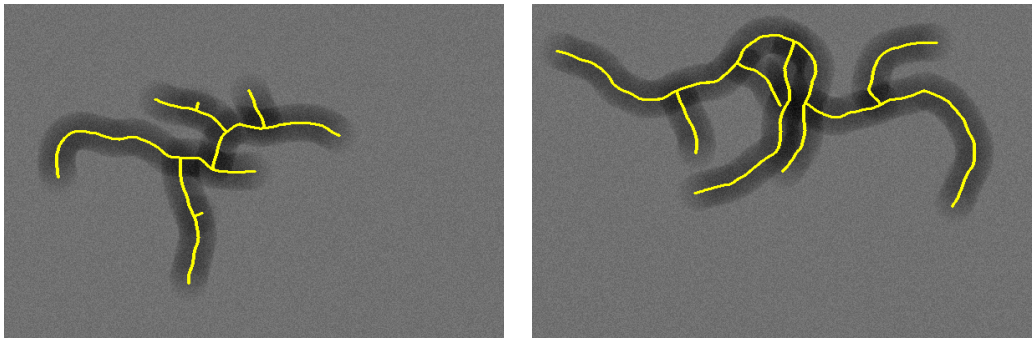

(a) (b)

Figure 6.5: Two example runs of the model described in Section 6.4. The intensity of the grey background pixels shows substrate strength, ranging from black (no substrate left) to light grey (no depletion).

6.4.2 Model results

As can be seen from Figure 6.5, the agent-based model grows virtual bacteria which display morphologies reminiscent of the microscope images of *Streptomyces* shown in previous chapters.

Our attempts at modelling autotropism by using the nutrient depletion to influence the direction of filament growth appear successful. In 6.5b, it is clearly possible to see filaments which have, in effect, steered away from nearby filaments. This is even more obvious when watching the growing virtual bacteria. Biologically, the mechanisms of autotropism are unclear and it is possible that it is achieved through the secretion of chemical signals rather than the sensing of nutrient depletion. However, the way we have modelled nutrient depletion is very similar to how we might model chemical signalling and so it seems reasonable to assume that the results would be the same.

In order to see how well our agent-based model can capture the differences between the bacterial strains, we used our experimental data to derive values for the model parameters. This involved a brute-force approach in which the software stepped through a range of different values for the parameters, grew 20 virtual bacteria for each parameter set and compared the resulting virtual bacteria with each experimental data set. In order to perform the comparison, we generated pairwise distance histograms (Section 5.14) for each set of virtual bacteria and calculated the root mean squared error (RMSE) compared to the eight experimentally derived

pairwise distance histograms. For reasons of efficiency, we restricted our search of parameter space to a few discrete values for each parameter (Table 6.4). Even so, this involved 4,320 combinations of parameters, 86,400 virtual bacteria grown and six days of processing by a dual core PC.

Figure 6.6 shows the best fit histograms obtained for each bacteria/media combinations and Table 6.5 lists the corresponding parameter values. Very close fits are obtained for all bacteria on SFM and for the Δ*filP* mutant on MMM. For the wild-type, Δ*scy* and Δ*scy-filP* mutants on MMM, our limited brute force search failed to produce fits as close as for the SFM data. A more targeted search of parameter space may improve on this. Even so, there are clear differences between the virtual bacteria generated with the wild-type on MMM parameter set and the Δ*scy* on SFM parameter set (Figure 6.7)

The brute-force approach resulted in the same parameter values for Δ*scy* and Δ*scy-filP* on MMM and the same values for Δ*scy* and Δ*scy-filP* on SFM. This is probably unsurprising given the similarity of the respective pairwise distance histograms. We believe that a longer search of parameter space, or the use of different histograms for comparison (eg. segment length, branch position) could result in differences in the parameters.

The model parameter results highlight some of the differences we observed experimentally. The shorter segment lengths we observed in the Δ*scy* and Δ*scy-filP* mutants (Section 5.7) are reflected in smaller values for L_B, the minimum length before branching. The tendency of new branches to appear towards the previous branch for wild-type on SFM and Δ*scy* on MMM (Section 5.10) is reflected in a branch position value of +20, though for Δ*filP* on SFM, which exhibits the same pattern, the fitting process produces a neutral branch position value of 0. Finally, the delayed secondary germ tube development of the Δ*scy* and Δ*scy-filP* on MMM

Parameter	Description
L_B	50, 100, 150, 200, 250, 300, 350, 400
α	0.01, 0.02, 0.05, 0.1, 0.2, 0.5
b	-20, 0, +20
t_g	50, 150, 250, 350, 450
γ	0.01, 0.02, 0.05, 0.1, 0.2, 0.5

Table 6.4: Agent-based model parameter search space.

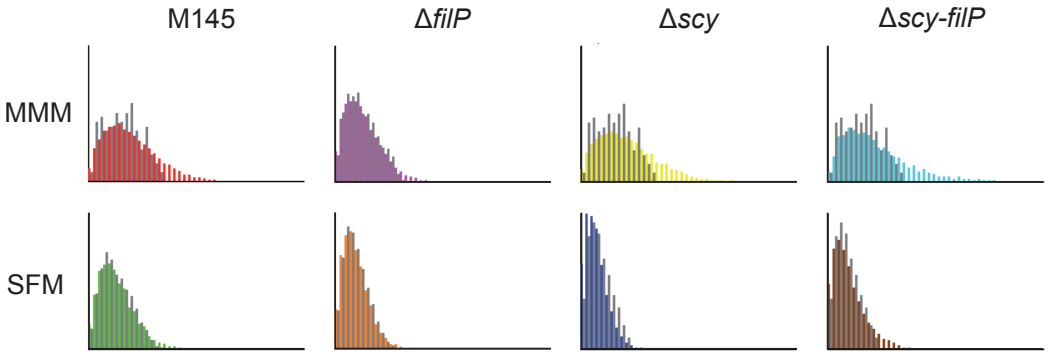

Figure 6.6: Pairwise distance histograms showing best fit model data (coloured bars) against corresponding experimental data (grey bars). Each model histogram is generated by growing 20 virtual bacteria. Best fit parameters (Table 6.5) were chosen using a brute-force search of parameter space.

Bacteria	Media	L_B	α	b	t_g	γ	RMSE
M145	MMM	350	0.02	+20	50	0.01	1.46
M145	SFM	250	0.5	+20	50	0.05	0.53
Δ*filP*	MMM	250	0.05	+20	50	0.02	0.57
Δ*filP*	SFM	50	0.01	0	250	0.02	0.27
Δ*scy*	MMM	350	0.02	+20	50	0.01	1.77
Δ*scy*	SFM	150	0.02	0	450	0.2	1.23
Δ*scy-filP*	MMM	350	0.02	+20	50	0.01	1.66
Δ*scy-filP*	SFM	150	0.02	0	450	0.2	0.94

Table 6.5: Best fit parameters for the agent-based model. Parameters chosen using a brute-force search of parameter space, with best fits determined by comparison of pairwise distance histograms. Positive values for branch position indicate bias towards branch, negative values a bias towards tip.

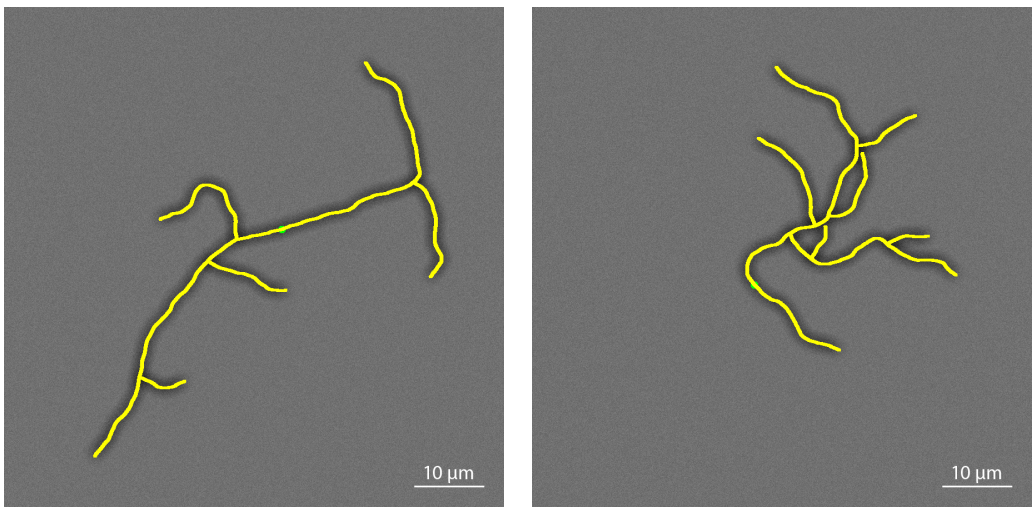

(a) (b)

Figure 6.7: Results of varying agent-based model parameters: (a) Virtual bacterium grown using the model fit parameters for M145 on MMM. (b) Virtual bacterium grown using the model fit parameters for the Δ*scy* mutant. Both models were run for the same length of time. Note the increased branching and more compact structures displayed by the mutant.

(Section 5.8) is reflected in a much lower value for γ, the second germ tube probability, than is found for SFM.

6.5 A mechanistic model of tip extension and branching

6.5.1 Overview

Our basic agent-based system was a phenomenological model which sought to capture the branching behaviour of *Streptomyces* through the application of a simple set of rules which were determined through microscopic observation of the bacterium. It was successful in so far as it was able to capture many of the observed differences in growth between the bacteria - such as the more compact morphology of the Δscy mutant on SFM. However, we wish to move beyond a purely descriptive model and to try to suggest a mechanism which could be responsible for the observed behaviour. This led us to develop a more sophisticated model of tip extension and branching based on ideas about the internal processes within filaments.

As discussed in Section 6.2.3, the Vesicle Supply Centre model of Bartnicki-Garcia *et al.* [5] best reflects current understanding of fungal tip growth. Though fungi and bacteria are fundamentally different, with the latter not possessing vesicles, it is reasonable to conclude there must be some kind of analogous process taking place in bacteria.

Our new system seeks to model the transport of a cell wall building component through the bacterial filament as a reaction-diffusion system. We do not specify the component, because very little is understood biologically. It may be that it represents cell wall precursors, which are eventually converted into cell wall at the tip. Or it may represent a collection of proteins that incorporate the cell wall precursors at the tip. We therefore refer to it in the rest of this chapter as *the key component*, adopting the terminology used by Yang *et al.* [85]. Whatever the key component composition, our model views chromosomes as machinery which are indirectly responsible for production of it.

The key component is transported towards the tip by a mixture of diffusion and active transport. As it arrives at the tip, it is converted to cell wall material and,

if enough has amassed, the tip is able to extend. The model also uses the build-up of the key component further back in the hypha as a trigger for production of new lateral branches.

The model consists of three parts. In Section 6.5.2, we derive a partial differential equation to describe the transport of the key component through the filament and to provide for production of it at chromosome sites. In Section 6.5.3, we describe the system for movement and duplication of chromosomes. Finally, in Section 6.5.4, we describe the rules implemented for tip extension and branching.

6.5.2 Transport of key component

In our model, we assume that the transport of the key component through the hypha is achieved through a combination of diffusive and active transport processes. We also assume that the production of the key component is dependent upon the number of chromosomes and their location along the filament. Using these assumptions, we now derive an equation to model the change in key component density due to transport and production.

Consider a 1-dimensional filament with a key component density given by the function $\rho(x,t)$. Fick's law [3] gives the change in density due to diffusion as

$$\frac{\partial \rho}{\partial t} = D\frac{\partial^2 \rho}{\partial x^2} \ ,$$

where D is a diffusion coefficient.

In a diffusive system, the diffusion distance is proportional to the square root of time (Figure 6.8). Given this, the relatively high growth rate of *Streptomyces*, the long length of filaments and typical biological diffusion coefficients in the range 10^{-7} to 10^{-10} $\mathrm{m^2 s^{-1}}$ [21, 60, 73, 82], it is unlikely that diffusion alone could account for sufficiently rapid transport of the key component along the whole length of the filament. Therefore, we introduce an active transport term to the above equation, giving

$$\frac{\partial \rho}{\partial t} = D\frac{\partial^2 \rho}{\partial x^2} - v\frac{\partial \rho}{\partial x} \ ,$$

where v is the velocity. This equation is known as Burgers' equation [8] and has

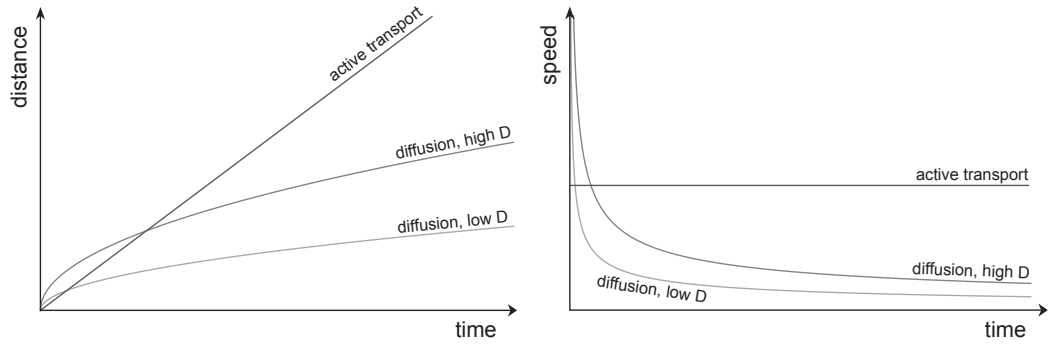

Figure 6.8: Graphs comparing the transport speed of diffusive and active processes. In diffusive processes, the diffusion distance is proportional to the square root of time, so initially quick transport soon rapidly declines in speed, even for high diffusion coefficient (D). This makes diffusive transport over longer distances an extremely slow process. In contrast, an active transport process is able to maintain speed, independent of distance.

been used to model many different kinds of flow, including that of liquids, gasses and vehicle traffic. However, the new term models a flow at a steady velocity. It is more likely that the active transport is dependent on key component density and either increases or decreases depending on the local density. There are examples of both of these relationships in nature. In eukaryotic cells, kinesin motors move along microtubules to transport vesicles to the tip and in areas of high density, the speed of transport is restricted because there are more vesicles to be transported than there are kinesins [34, 84]. Conversely, in plant root hairs, PIN proteins are thought to mediate transport of the growth hormone Auxin and this transport increases in areas of greater PIN density [9, 29]. Furthermore, it is believed that production of PINs is in turn regulated by Auxin, resulting in a positive feedback mechanism [51].

Returning to the equation above, to make the active transport dependent on density, we rewrite it as follows:

$$\frac{\partial \rho}{\partial t} = D\frac{\partial^2 \rho}{\partial x^2} - v_0 v(\rho)\frac{\partial \rho}{\partial x} \ ,$$

where

$$v(\rho) = 1 + \rho(x) \ , \tag{6.5}$$

for a transport speed which increases with density, or

$$v(\rho) = \frac{1}{1 + \rho(x)} \ , \tag{6.6}$$

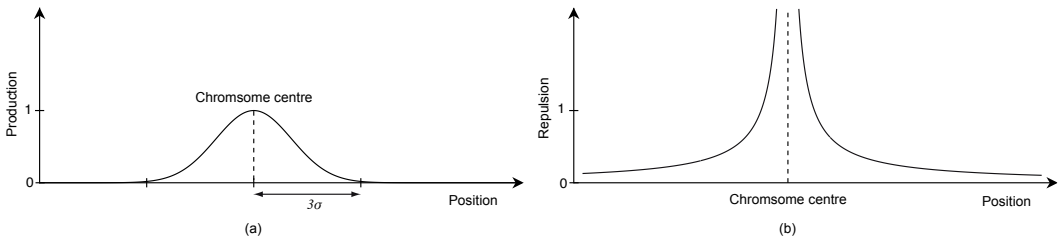

Figure 6.9: (a) Graphical representation of the function used to model the input of the key component at chromosome sites. The width of the chromosome is equal to 6σ. (b) Graphical representation of the chromosome repulsion energy function used to prevent chromosomes occupying the same position.

for a transport speed which decreases with density. The constant v_0 is chosen to be the speed of transport of the key component when $\rho(x) = 0$.

In *Streptomyces*, there are reasons to believe that the tip exerts a form of polar attraction. This is evidenced by experimental work which has imaged the build-up of wall precursors at the tip [14]. It is believed that these precursors either travel towards the tip, or that enzymes responsible for their production travel towards the tip from the chromosomes where they are created. Additionally, the protein DivIVA has been found to have an attraction to the curved surfaces of hyphal tips, which could also provide a concentration gradient [50]. We express the tips polar attraction as a modification to the transport velocity which is dependent upon a local concentration gradient, yielding

$$\frac{\partial \rho}{\partial t} = D\frac{\partial^2 \rho}{\partial x^2} - v_0 e^{-\lambda(l-x)} v(\rho)\frac{\partial \rho}{\partial x} \ , \tag{6.7}$$

where l is the length of the filament and λ is a decay constant which allows controls of the steepness of decay.

As stated in Section 6.5.1, we consider chromosomes to be the engines responsible for production of the key component. Each filament will have $N(t)$ chromosomes with centres located at positions x_1,...,x_N along the 1-dimensional hypha. We represent the key component production of each chromosome as a Gaussian distribution centred around the chromosome centre (Figure 6.9a), given by

$$P(x) = \frac{1}{\sqrt{2\pi\sigma^2}} e^{-\frac{1}{2\sigma^2}(x_i - x)^2} \ ,$$

where x_i is the centre of the chromosome and σ is related to the chromosome width. Because 99% of any Gaussian distribution is located within 3σ of its centre, we set σ equal to

$$\sigma = \frac{w}{6} \ ,$$

where w is the width of the chromosome. Thus, we introduce a new term into equation 6.7 to sum the contributions of all N chromosomes, giving

$$\frac{\partial \rho}{\partial t} = D\frac{\partial^2 \rho}{\partial x^2} - v_0 e^{-\lambda(l-x)} v(\rho)\frac{\partial \rho}{\partial x} + \rho_0 \sum_{i=1}^{N} \frac{1}{\sqrt{2\pi\sigma^2}} e^{-\frac{1}{2\sigma^2}(x_i - x)^2} \ , \tag{6.8}$$

where ρ_0 determines the rate of key component production.

6.5.3 Chromosome movement and replication

In the model, chromosomes move up and down the filament in a biased random walk. In order to ensure two chromosomes do not occupy the same space, we represent the space occupied by them with a repulsive force and use this to influence the walk.

Consider N chromosomes centred at position x_1,...,x_N along the 1-dimensional hypha. We define a chromosome energy function, $E(x)$, given by

$$E(x) = \sum_{i=1}^{N} \frac{R}{|x_i - x|} \ , \tag{6.9}$$

where R determines the level of repulsion. Figure 6.9b provides a graph of the energy function for a single chromosome.

For each chromosome, at every tick of the model clock, a possible move is selected by picking, with equal probability, a neighbouring location on either side of the current location. The decision on whether to accept the move is inspired by a concept from statistical mechanics known as the Boltzmann factor, which calculates the probability of a system under thermodynamic equilibrium moving into a given state [31]. Our variation of the concept works as follows. The energy at the current location, E_c, and at the proposed location, E_p, is calculated according to Equation 6.9. The difference in the two energies, ΔE is thus

$$\Delta E = E_p - E_c \ .$$

If ΔE is less than zero, indicating that the proposed location is at a lower energy than the current location, then the move is always accepted. However, if ΔE is greater than zero, indicating that the proposed location is at a greater energy, then the move is accepted with a probability given by

$$p = e^{-\frac{\Delta E}{E_0}} ,$$

where E_0 is a constant chosen such that around half of all proposed moves in the system are accepted. If this was a standard Boltzmann factor calculation, then $E_0 = k_B T$, but for simplicity, we do not consider temperature to be significant. If a move is not accepted, the chromosome stays where it is.

As the tip extends, chromosome duplication occurs. The biological reasons for the timing of chromosome duplication are unclear, so, in our model, duplication is tied to the overall chromosome density in the filament. Once this reduces to a threshold level, a chromosome is picked at random for duplication. The new chromosome is initially located at the same position as the original, but the repulsive energy quickly causes a separation between the two.

6.5.4 Tip extension and branching

The filament grows by a unit length every time the the key component level close to the tip reaches a threshold value. Before the tip extends, the key component level at the tip is reduced to reflect the consumption necessary to build the new cell wall.

Lateral branches are initiated when there is a build-up of the key component further back behind the tip. This will occur when the key component is being produced faster than it can be transported to, and used by, the tip. Rather than implement a simple threshold level, we generate a branch probability. For any position, x, along the filament, the probability of a branch, $p(x)$, is given by

$$p(x) = 1 - e^{-\frac{\rho(x)}{\rho_1}} ,$$

where $\rho(x)$ is the key component density at position x and ρ_1 is a constant which makes branching occur more or less frequently. More specifically, when $\rho(x) = \rho_1$,

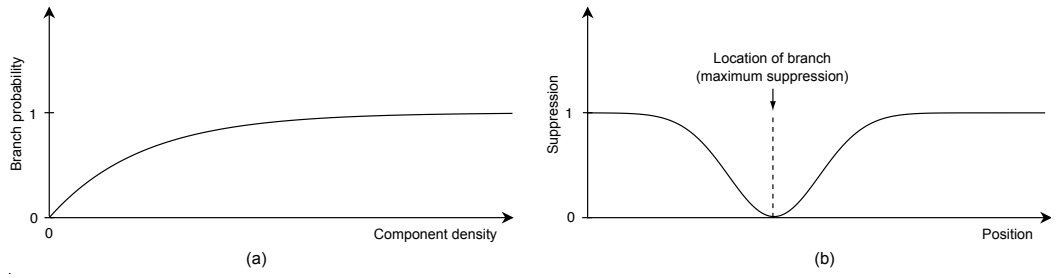

Figure 6.10: (a) Graph of branch probability function, with the steepness of the curve determined by the constant ρ_1. (b) Graph of suppression function for an example branch point, with the width of the curve determined by the constant x_0. Maximum suppression occurs at $y = 0$.

$p(x) = 0.63$. Thus ρ_1 it is the key component density at which there is a 63% chance of a branch forming at any given tick of the clock. Figure 6.10a provides a graphical representation of the branch probability function.

In wild-type *Streptomyces*, new branches rarely form close to an existing lateral branch. This can be seen in the segment length histograms for the wild-type, given in Section 5.7, which have their peak at around 7 µm. It has been suggested that a protein such a Scy, which localises to new tips and co-localises with DivIVA, might perform a branch suppression function [39]. We model the (inverse) suppression as an exponential function which is centred on the branch location (Figure 6.10b). Thus, we can modify the equation for p_x to represent the (inverse) suppression, giving

$$p_x = \left(1 - e^{-\frac{\rho(x)}{\rho_1}}\right) \prod_{i=1}^{N} 1 - e^{-x_0(b_i - x)^2} \ , \tag{6.10}$$

where b_i is the location of the ith branch on this filament and x_0 is a suppression distance constant.

6.5.5 Implementation

In our implementation of the model, a filament is represented as an array of values representing the key component level at each position within the hypha. At each tick of the model, the following sequence of events occurs:

1. **Chromosome copying** - if the chromosome density has reached the threshold value, make a new chromosome by selecting one of the current chromosomes, at random, for duplication.

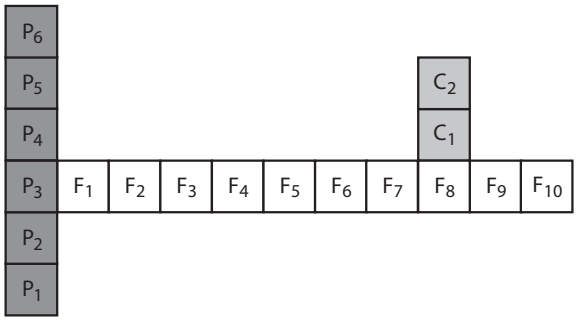

Figure 6.11: In this figure, the diagram represents a filament F, its child C and its parent P. After carrying out the modelling steps for filament F, position C_1 is set to equal the key component level at position F_8 and position P_5 is set to equal the key component level at position F_1.

2. **Chromosome movement** - each chromosome is evaluated for a move one place up or down the hypha.

3. **Branch initiation** - we apply Equation 6.10 at each point to determine if a new branch is to be initiated.

4. **Tip extension** - if the key component level at the tip has reached the threshold value, then extend the tip.

5. **Transport of the key component** - the level at each position in the filament is updated by evaluating Equation 6.8.

This basic model is easily extended to facilitate multiple filaments. In this scenario, a sixth step is carried out for each filament to handle the transport of key component between parent and child filaments. This is achieved by equalising the key component density across connected filaments. Consider the example in Figure 6.11, which represents a filament F, its parent P and a child branch C. Locations C_1 and F_8 represent the same physical location, so after performing the key component transport in F, we set the density at C_1 to equal that at F_8. Similarly, locations P_3 and F_1 represent the same physical location, so the density at P_3 is set to the density at F_1.

As well as the continual equalisation of branch points between parent and child filaments, we apply a once-only depletion of nutrients in the parent filament at the point of the branch. This is achieved by setting the the key component density at

the branch point to half its level at the time the branch is initiated. In order to avoid numerical instabilities, we spread the depletion over an area defined by an exponentially decaying depletion function. Thus, we multiply the key component by the factor

$$\frac{1}{2}e^{-x_1(b_x-x)^2} \ ,$$

where b_x is the location of the branch and x_1 is a constant which defines the depletion width.

6.5.6 Numerical methods

Equation 6.8 is a non-linear partial differential equation which cannot be solved analytically. It is also an initial value problem - we know the nutrient densities, $\rho(x)$, at time $t = 0$ and we wish to understand how these densities change over time. To solve numerically, we divide the spatial and temporal domains into discrete units - size h for space and Δt for time.

We need a way to compute the spatial derivatives and to move the initial value problem forward in time. Examining first the temporal domain, we note that many functions can be written in the form

$$f(t) = f(0) + \int_0^t \frac{df}{dt} dt \ .$$

The integral may be approximated using the trapezium rule. For a sufficiently small interval, Δt, we shall use the approximation

$$f(t) \approx f(0) + \sum_{i=0}^{N} \frac{df(i)}{dt} \Delta t \ . \tag{6.11}$$

The application of this approximation is known as Euler's method. Given an initial value, Euler's method allows us to approximate a curve that satisfies a known differential equation. To use Equation 6.11 to solve our model equation (Equation 6.8), we need to be able to numerically compute spatial derivatives. This we do using finite difference formulae. These seek to approximate the derivative by using two or more closely spaced values from a function to calculate its local gradient. If we have a function, $f(x)$, then the two point central difference at point x is given

by

$$\frac{df}{dx} \approx \frac{f(x+h) - f(x-h)}{2h} \ ,$$

where h is the step size, or distance between neighbouring values. Selection of this value is important and it is desirable to pick a value as small as possible without chosing one so small that rounding errors are introduced or computation time is too long. Figure 6.12 pictures three runs of the model using different step sizes which illustrate the issues connected with selection of step size.

Note that care needs to be taken with approximation of end point derivatives because at $x = 0$ we don't know $f(x-h)$, while at $x = n$ (where n is the size of the filament), we don't know $f(x+h)$.

In our problem, at $x = 0$, if we set $f(x-h)$ to be greater than $f(x+h)$, then the end point will in effect act as a key component producer. Alternatively, if we set $f(x-h)$ to be less than $f(x+h)$, then the end point will act as a sink. So, instead, we set $f(x-h)$ to be $f(x+h)$, so that the gradient is always zero at this point and it neither contributes to, or subtracts from, the key component level.

The point $x = n$ (where n is the size of the filament) represents the apex of the tip and here we do want the key component to reduce. Therefore, we use a single point approximation for the derivative as follows

$$\frac{df}{dx} \approx \frac{f(x) - f(x-h)}{h} \ .$$

Finally, we compute second derivatives using

$$\frac{d^2f}{dx^2} \approx \frac{f(x+h) - 2f(x) + f(x-h)}{h^2} \ .$$

6.5.7 Simulation results

In the preceding sections, we have derived a model which links the tip extension and branching processes within *Streptomyces* to the movement through the filament of a chromosome-produced key component by a combination of diffusive and active transport. The model consists of a partial differential equation which expresses the change in key component density due to transport and new production, along with

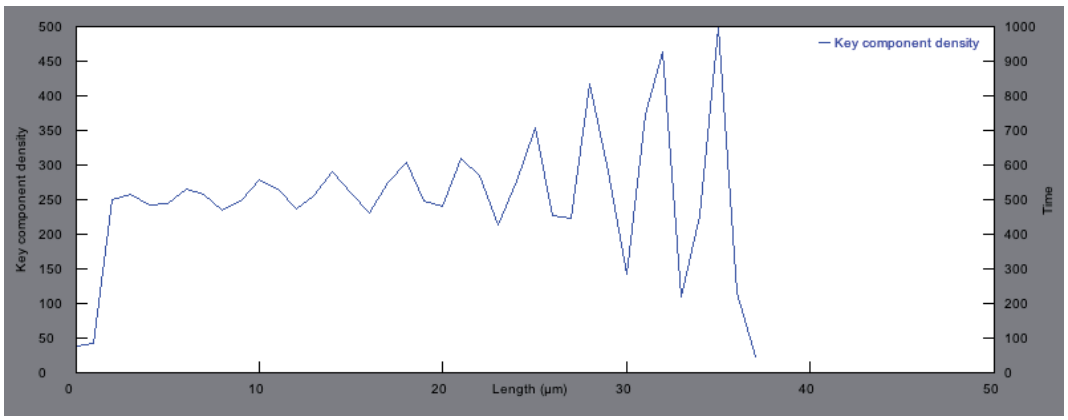

(a) h=1 µm

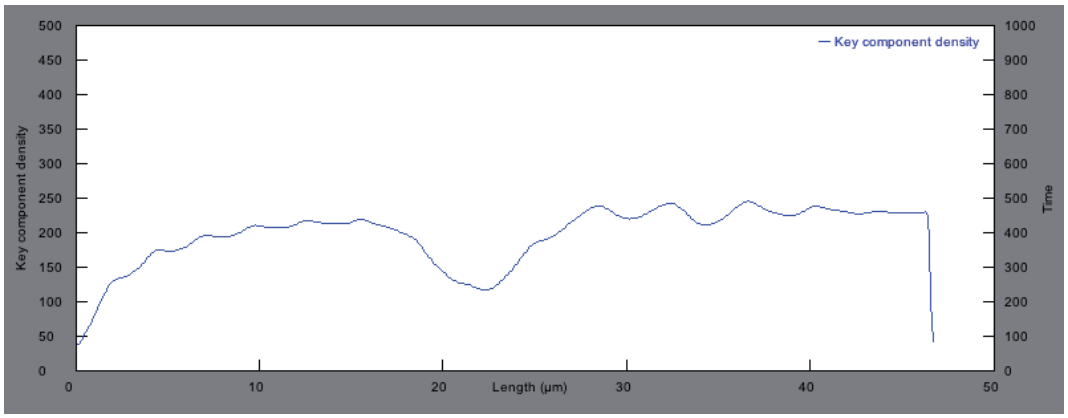

(b) h=0.1 µm

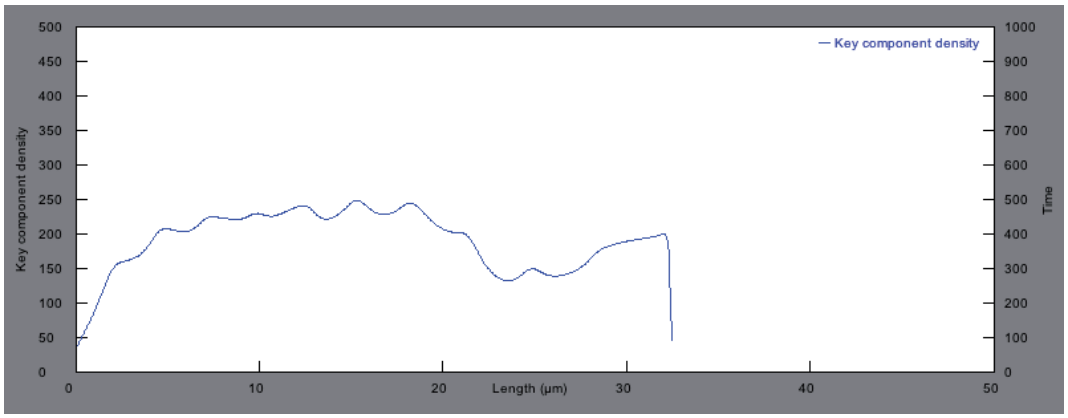

(c) h=0.05 µm

Figure 6.12: The three images show three runs of the model, each with identical parameters and random number generator seed, but with different step sizes: (a) A step size of 1 µm is too large, resulting in numerical instabilities. (b) We used a step size of 0.1 µm, small enough to remove numerical instabilities, but large enough to reduce rounding errors and speed up processing time. (c) Smaller step sizes run the risk of introducing rounding errors and may take too long to process.

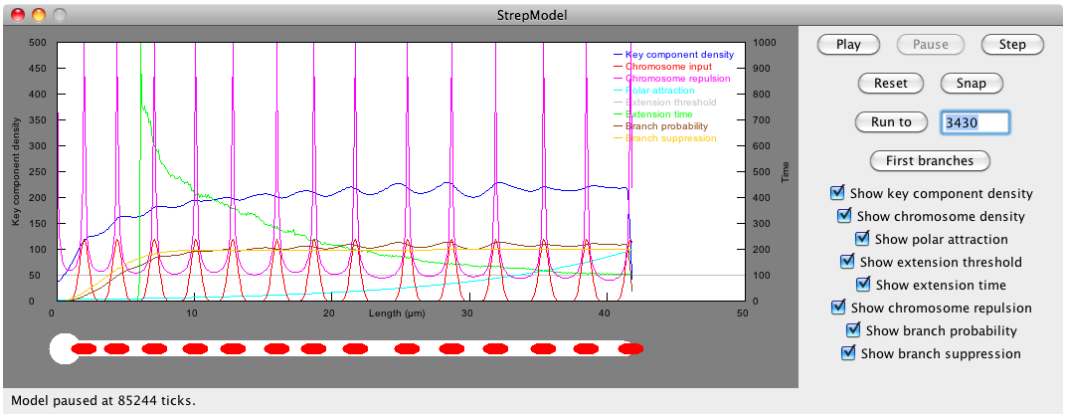

Figure 6.13: The Java implementation of the model running. The bottom part of the image is given over to a graphical representation of the growing filament, with chromosomes shown in red. The graph shows the concentration of key component (blue line), as well as the levels of other important parameters, such as chromosome production (red line) and tip extension time (green line).

rules for the movement and duplication of chromosomes and the creation of new branches. We have also introduced techniques for solving the equations. We now describe the results of running the simulation and the effect that parameter variation has on these results.

A typical simulation run

The model was implemented in a Java application which provides graph traces of the key component level, tip extension time, chromosome movement and a range of other attributes as the simulation proceeds (Figure 6.13).

Figure 6.14 show graphs of a typical simulation run, from development of the primary germ tube until initiation of the first branch. The key component density (blue trace) builds gradually, as the tip extends. As the density increases, so the probability of a branch also increases. When a branch occurs, the key component density around the branch is depleted, resulting in a lower density behind the branch. This means that it is much more likely that a second branch will occur between the first branch and the tip - reflecting what is observed experimentally.

Initially, the tip extension time (green trace) starts off high, as the chromosomes begin production of the key component and it is transported towards the tip. However, as the density of the key component increases and the number of producing chromosomes increase, the tip extension time decreases until eventually reaching a

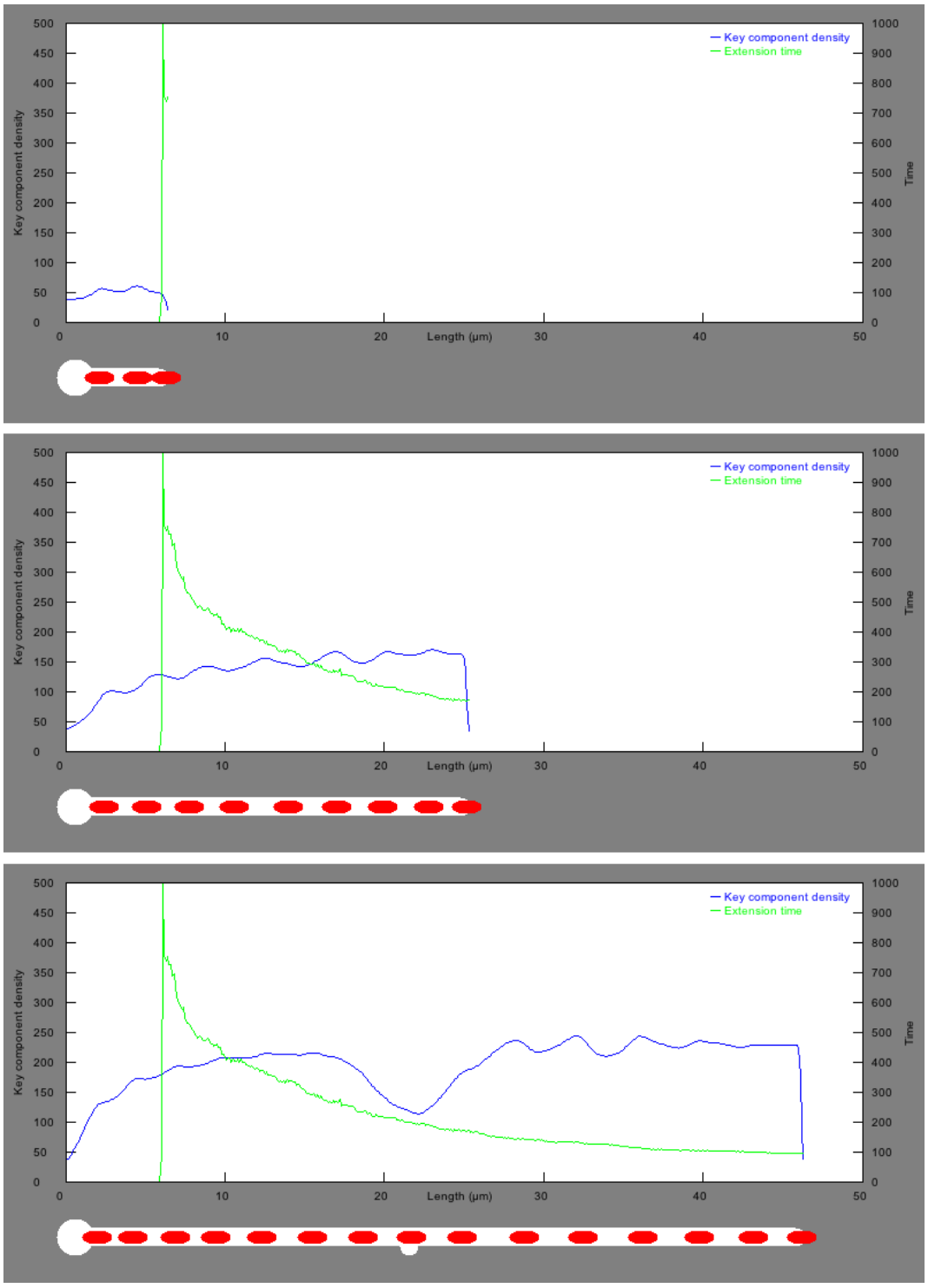

Figure 6.14: A typical model run: The filament starts small and extension rate is slow (top image). Gradually, the tip extends and the rate of extension increases (middle image). The extension rate reaches a maximum and new branches are initiated (bottom image). At the site of the branch, the key component level is depleted.

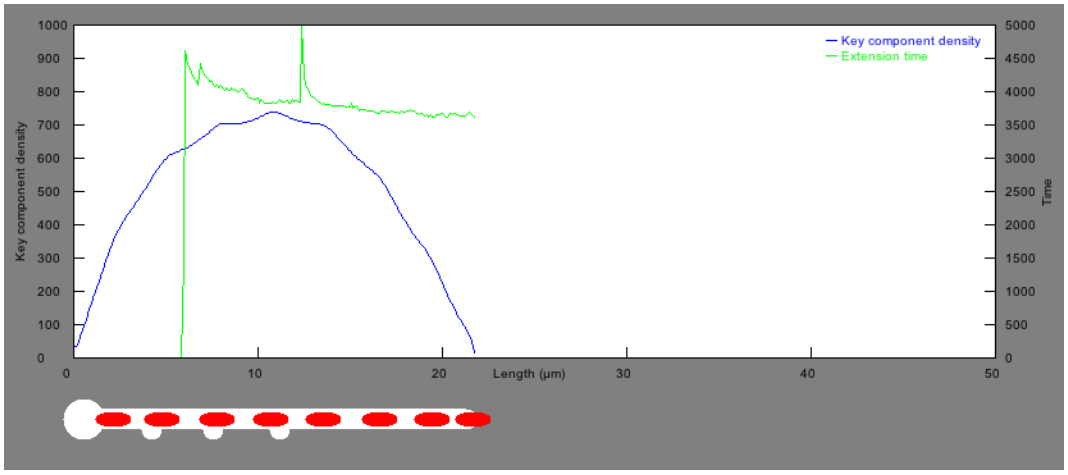

Figure 6.15: Example simulation run for the condition that active transport speed decreases with increasing key component density. This results in a single large key component density peak, increased tip extension times and less convincing branching patterns.

relatively steady state. This same phenomenon has been observed experimentally, with a time of between 2-4 hours needed for a germ tube to achieve a steady rate of extension [2].

Two different approaches to active transport

Our model derivation allows for two approaches to active transport, depending on whether we assume that the speed of transport increases or decreases with increasing key component density. The figures presented so far are based on simulation runs which adopt the first assumption. However, we also explored the model behaviour under the assumption that transport speed decreases with increasing key component density. This generally resulted in less convincing results, as illustrated in Figure 6.15. This figure was generated from a simulation run using the same parameter set as for Figure 6.14, with the only difference being the change of active transport condition. This results in a single large key component density peak, much increased tip extension times, much closer branching and an increase in the number of branches appearing before the previous branch. With changes to some model parameters, it was possible to reduce problems, but unconvincing behaviour remained.

As a result, in the absence of any contrary biological evidence, the simulations that follow are all based on the assumption that speed of transport increases with increasing key component density. This assumption means that over time, the peaks

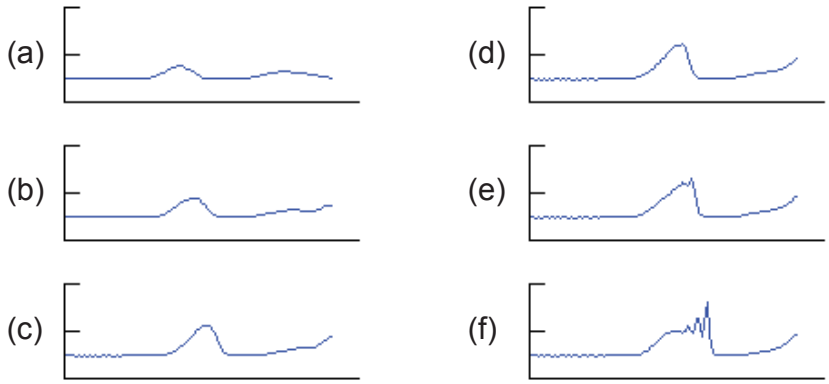

Figure 6.16: Numerical instability created by active transport process: in (a) to (c), a peak gradually builds. In (d) to (e), we can see the peak moving forward faster than the trough until in (f), it overtakes causing a numerical instability.

catch up with the troughs and larger peaks consume shorter ones. This can sometimes mean that numerical instabilities occur as the top of a peak overtakes the bottom (Figure 6.16). In nature, we observe this phenomenon in ocean waves as they crash onto a beach. However, in our model, it presents a problem which is very difficult to solve numerically. Initially we had wondered if the shocks that formed at this point could be the trigger for branching activity, but we were unable to achieve any convincing results under this assumption. We have therefore chosen to avoid model parameters that create such instabilities. Although we acknowledge that this could mean we are missing out on exploring a potentially important area of parameter space, we believe that the results presented in the next section suggest that convincing solutions of the model are to be found in the parameter space which we are able to access.

Comparison with experimental data

In order to compare the performance of the model with our experimental data, we grew a set of 80 virtual bacteria and measured the segment lengths, the relative position of each branch and the length of segments at the point of branch initiation. We plotted histograms of these values and compared them with the distributions obtained experimentally (given in Chapter 5). The model histograms are shown along with the experimental ones in Figure 6.17 and the model parameters used are given in Table 6.6.

The model segment length histogram shows a similar shaped distribution to the

Parameter	Description	Value
D	Diffusion coefficient	1×10^{-4} µm$^2 s^{-1}$
v_0	Active transport speed constant	1×10^{-5} µm$^2 s^{-1}$
λ	Concentration gradient decay constant	0.008
ρ_0	Key component production rate	0.01
w	Width of chromosome	2 µm
R	Chromosome repulsion level	20
ρ_C	Minimum chromosome density	0.33 per µm
E_0	Energy constant	0.1
ρ_1	Branching rate constant	1×10^9
x_0	Suppression distance constant	0.05
T	Tip extension threshold	50

Table 6.6: Model parameters used for comparisons with experimental data.

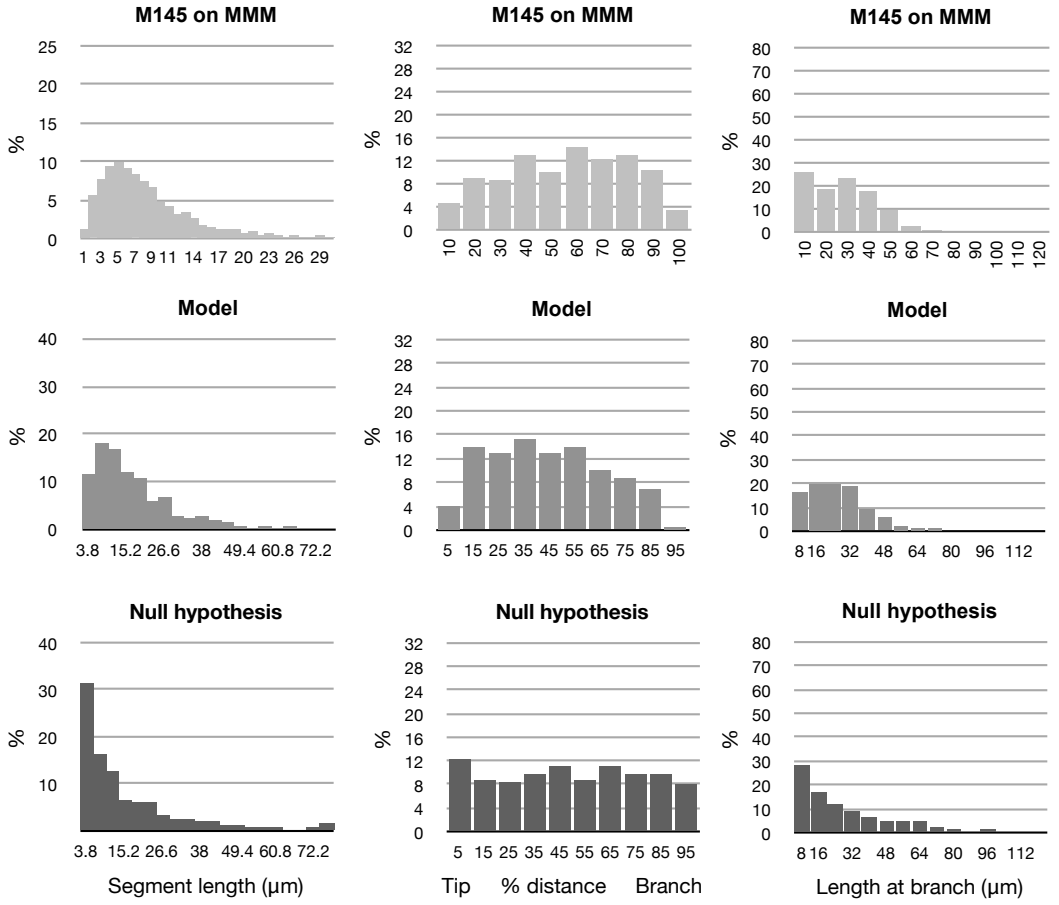

Figure 6.17: Comparison of model data with experimental data: The top graphs show histograms for segment length, relative branch position and length of segment at branch, obtained experimentally for the wild-type *Streptomyces* grown on MMM. The middle set of graphs show histograms produced from 80 runs of the standard model. The bottom set of graphs show another 80 runs of the model, but this time the branching is set to an even probability throughout the filament instead of linked to key component density.

experimental one, with a steeper slope on one one side of the peak and a gentler one on the other. The model branch position histogram also displays a similar distribution to the experimental one, with very little in the first and last 10% and a relatively even distribution in the central 80%. The histograms of length at branch are also similarly shaped.

We wanted to get some idea if this fit to the experimental data could be attributed to our model, or if a less sophisticated model of branching would lead to similar distributions. Therefore, we set up a null hypothesis model, exactly the same as the current model except that branch initiation was set to the same probability throughout the filament length and not linked to key component density. We again grew 80 virtual bacteria and generated histograms from the simulation results (also Figure 6.17). These results show clearly different distributions to the standard model and the experimental data. The segment length distributions and length at branch distributions no longer have the same shape as the experimental data. As we would expect, the branch position histogram shows an even distribution, with branches equally likely at all positions. However, in both the experimental data and the model data, we see slight dips at either end of the graph, something not captured in the null hypothesis graphs.

Removal of suppression term

In Section 6.5.5, we introduced the branch suppression term by stating that a protein such as Scy might be responsible for suppression of additional branches at existing branching sites. We were therefore interested to see if removal of this aspect of the model creates branching behaviour more like that seen in the Δscy mutant.

Figure 6.18 shows histograms of segment length, relative branch position and length of segment at branch for another 80 runs of the model, this time with the branch suppression functionality removed. For comparison, the experimental data for the Δscy mutant on SFM is also shown. The removal of the suppression has a significant effect on the model results, with a larger number of small branches leading to a different shape for the segment length distribution. Additionally, the relative branch position distribution is changed, with a slight bias towards tip branching.

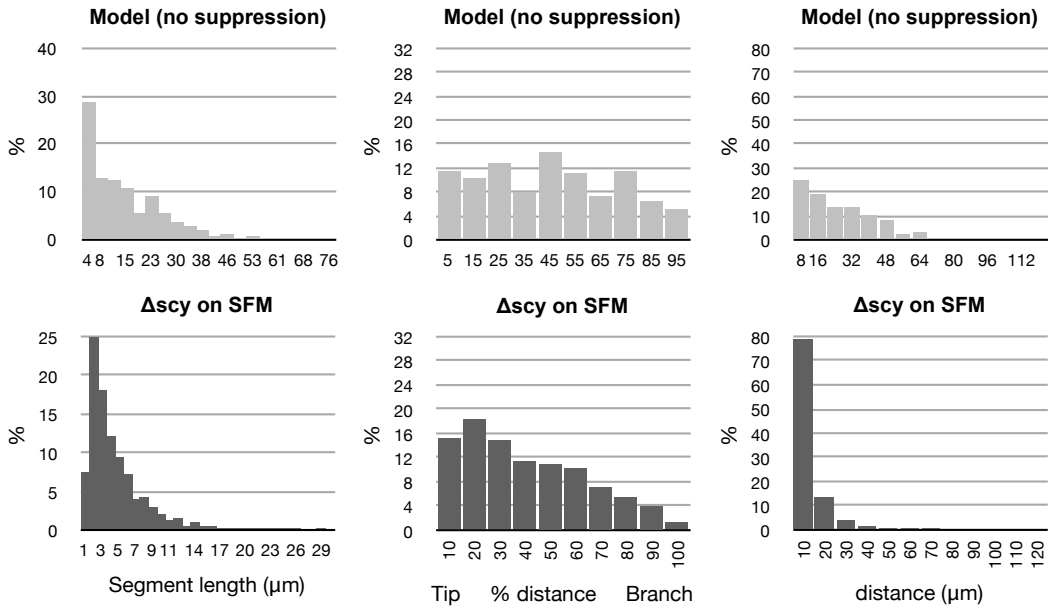

Figure 6.18: Effect of removal of suppression term from the model: The top three graphs show histograms of segment length, relative branch position and length of segment at branch for 80 runs of the model with the suppression term removed. The bottom graphs show the corresponding experimentally obtained data for the Δscy mutant grown on SFM media.

Both of these histograms take on similarly shaped distributions to those we found for the Δscy on SFM. This would seem to add plausibility to our suggestion that Scy has some sort of inhibitory effect on branching. However, at this stage, the experimental evidence is tentative and it is likely that there are many complex protein interactions involved in determining and preventing new branch initiation.

6.6 Discussion

In this chapter, we have presented three different approaches to the modelling of *Streptomyces coelicolor* growth and branching.

Our first approach was to use a set of population balance equations to model the balance of three different types of hyphal element - static sections of filament, branching filament sections and sections which will either branch or become static. We were able to fit our experimental data to the model to obtain values for the model parameters. Experiments using the same bacteria and media combination occupied a similar area of parameter space to each other. By calculating the root mean squared error of fit, we found the model usually resulted in a smaller error

than fitting to a simple exponential function. However the difference in error was not large and we suggested that a reason for this may be that the data used for the fit is relatively noisy.

Our second model uses an agent-based approach to understand the spatial organisation of *S. coelicolor*. Simple rules govern the extension of tips and initiation of new branches, yet realistic images of growing bacteria can be produced. We used a brute-force approach to fit model parameters based on our experimental data. While we were able to capture differences in the observed morphologies, the model was unable to provide mechanistic insights.

With our final model, we made some suggestions about mechanisms that might be at work within a growing filament and wanted to understand if these could be responsible for producing the branching behaviour we observed. We model the transport and production of a key component through the filament and determine branching sites based on the density of this component. We found the model produced similar shape segment length distributions and branching site distributions to experimentally obtained data for the wild-type bacteria. By removing a branch suppression term from the model, we found it exhibited similar behaviour to the Δscy mutant, which provided support to the idea that Scy may be involved in selection and suppression of branching sites.

Chapter 7

Conclusions and Future Work

7.1 Summary

In the previous chapters, we have described our work analysing and modelling the early stage morphology of the filamentous bacterium *Streptomyces coelicolor*. It is an important bacterium and, despite its usefulness to medicine and industry, there is still much to understand about the mechanisms of its growth and branching.

We have described laboratory techniques and image processing algorithms which have enabled us to produce a thorough analysis of the morphology of wild-type *S. coelicolor* and three mutant strains. As far as we are aware, this is the most comprehensive quantitative analysis of the wild-type bacterium and contributes significantly to the understanding of its growth. Additionally, we have been able to compare the analysis of the wild-type with the same analysis of mutants with the *filP* and *scy* genes deactivated. This has enabled us to understand specific differences in morphology and to provide evidence to support ideas about the function of these genes.

We have also described the design of a software tool, JFilamentAnalyser, for providing semi-automatic analysis of filamentous microbes. We believe this tool will be of long-term use to the *Streptomyces* community and will help to facilitate the increased use of quantitative data in the description of mutant phenotypes.

In the previous chapter, we introduced three new models of *Streptomyces* growth. With each of the models, we were able to link them to our experimental data and, through parameter changes, we demonstrated that the models were able to quan-

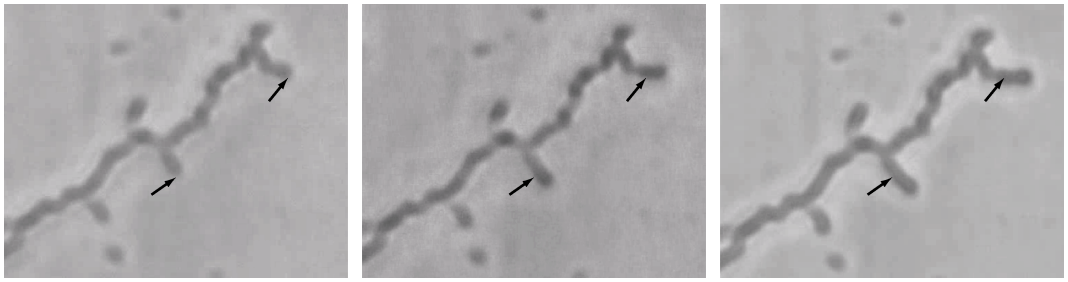

Figure 7.1: Three frames from a 40 minute long live imaging movie of *S. coelicolor* growth. Extension of individual tips can clearly be seen. The arrows are positioned at the same place in each frame and show the location of the tips in the first frame.

titatively capture some of the observed differences in the bacterial strains. Of the three models, the mechanistic model of key component production and transport offers great potential for further development.

7.2 Future work

7.2.1 Live imaging

All the experimental data presented in this thesis was obtained using the static imaging techniques described in Chapter 3. Part of the staining process involves fixing the bacteria, which means that images are only ever a snapshot at a moment in time. Unlike static imaging, live imaging offers the prospect of watching an individual bacterium as it grows and branches over time.

Techniques for live imaging of *Streptomyces* are not yet well established. Indeed it was only during late 2008 that the first significant study of *Streptomyces* using live imaging was published [38] and movies are still relatively rare and short. There are many problems to be overcome, particularly around maintaining oxygen supply, humidity and nutrient supply, while also allowing the microscope objective to be close enough for useful images to be obtained.

During our experimental work, we started to develop our own techniques for live imaging. These enabled us to produce short movies of approximately 40-60 minutes in length and to watch individual tips extending (Figure 7.1). We believe that with further development, our approach could be refined and longer movies should be possible. There now follows a brief description of the method we adopted.

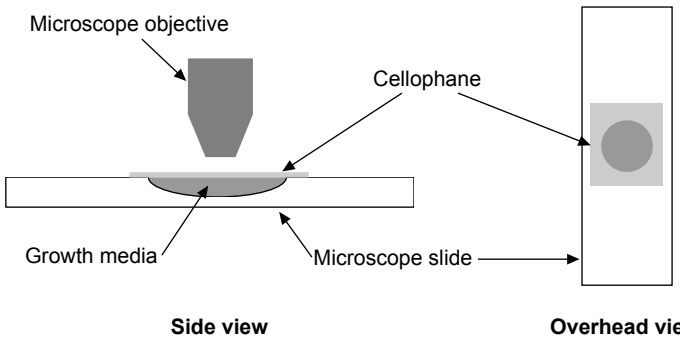

Figure 7.2: Experimental setup for live imaging: a microscope slide with a central well filled with liquid medium is used. A piece of cellophane with a bacterial sample on it is placed on the slide resting on top of the media with access to the air.

Sample preparation

Samples are initially grown in a Petri dish before being transferred after early growth to the microscope. As with static imaging, the Petri dish is filled with a medium such as MMM and a slip of cellophane is placed on top of the medium. The plate is covered and placed in an incubator at 30℃.

After a period of time, typically 5-10 hours, the Petri dish is removed and a razor blade used to cut a small (approximately 2 cm $\times$ 1.5 cm) portion of the cellophane away from the surface. The cellophane is then mounted on to a special microscope slide which contains a small well in its centre (Figure 7.2). This well is filled with clear liquid medium and the piece of cellophane rests on top of the medium, supported by, and level with, the sides of the slide. The bacteria on the cellophane should be able to continue to grow, as long as they have access to the medium and to air. The cellophane is fixed with tape and the sample is then ready for live imaging.

Microscopy

The slide is placed under the microscope objective, taking care not to make contact between the sample and the objective. The need to avoid interference with the sample makes it impossible to use oil-based objectives, as the oil prevents the bacteria receiving the oxygen needed for growth. This makes good images difficult to obtain and is further complicated by the fact that the microscope light has to be transmitted through the liquid medium.

As live imaging progresses, the medium in the well is gradually depleted due to evaporation. Unless this is topped up, the bacteria will cease growing. Additionally, the cellophane tends to droop into the well as the medium evaporates.

Live imaging outlook

Using these techniques, we were able to capture videos of up to an hour in length and were able to watch the extension of individual hyphal tips. Image quality was acceptable but suffered from constantly changing focus. We believe this was due to evaporation of the liquid medium and the consequent drooping of the cellophane. After around an hour, the bacteria seem to stop growing and we believe this is due to a number of factors:

- Lack of access to nutrients, due to evaporation of liquid medium.
- Possible heat damage from the bright microscope light. This problem is reduced by shuttering while images are not being taken, but we suspected damage was still occurring.
- Loss of humidity.
- Lack of control over temperature.

We have experimented with the use of an inverted microscope, but were not able to substantially improve results. We believe that use of a temperature and humidity controlled chamber should help to increase the lifespan of the bacteria and enable longer videos to be captured. Additionally, identification of suitable fluorescent markers which do not require fixing would improve things considerably.

7.2.2 Analysis and statistics

Our software, JFilamentAnalyser, has proven to be a very effective tool for analysis of our experimental dataset of microscope images. We believe it could be a valuable tool for use by the whole *Streptomyces* research community and perhaps by those interested in other filamentous microbes.

There are a number of enhancements that could be made to the software which would increase its suitability for use by biologists. The following is a list of possible changes.

- Statistics presentation - after batch analysis, the tool currently writes CSV files of data, which the user has to manipulate using a spreadsheet or other package such as Matlab. The tool could be enhanced to include the ability to present histograms and tables of data without the need to use a third-party application.
- Automatic identification of spore - currently this is selected manually.
- Unstained images - the image processing techniques are designed to work using images that have been stained in a way which increases the contrast between cell wall and background. However, there are some experiments where we may not wish to stain the cell walls, so the image processing techniques could be enhanced to work in such situations.
- Live imaging - as live imaging becomes more common, the tool will need to be enhanced to cope with movies of growing bacteria. It could examine periodic frames and present data to show how statistics are changing over time.

As well as these general changes, there are a number of additional biometrics and statistics which it would be useful for the tool to measure. These include:

- Measurements of hyphal diameter.
- Do new branches form on the inside or outside of curves? This has been commented on in [33], but it would be useful to quantify it.
- Is the branch nearest the tip always the shortest one? If so, this provides evidence that new tips always form between tip and previous branch, as implied in [45].
- Measurements of spore area.
- Identification of septa, in suitably stained images.

- Measurements of chromosome area, in suitably stained images.
- A measure to differentiate between different morphologies - for example long, thin versus wide, fat.

7.2.3 Modelling

Agent-based model

The agent-based model implements a naive scheme of nutrient consumption which largely ignores the composition of the growth medium and its effect on bacterial morphology and growth. The two media used in our experimental work had mannitol concentrations of 27.45 mM and 658.73 mM and, although there were other compositional differences too, the availability of this sugar alcohol would likely play a key part in explaining morphological differences such as the decreased length of filament segments on the richer SFM media. It would be interesting to extend the current model in two ways. Firstly, replacing the basic model of nutrient depletion around the organism by a diffusion based model. The result would be a better estimate of the nutrient concentration as neighbouring hyphae grow close to one another. The second would be to drive cell growth rates by the total local nutrient available to each cell. The result would be that as nutrient is consumed around each cell so growth rates would reduce. In such a model, growth and branching would be directly linked to the concentration of nutrients in the medium surrounding the filaments and one would expect the morphology of a given genotype to be different in the different media. There would be more branching and cells would be closer together in media with high nutrient concentrations.

Some further experimental work could enable the hypothesis to be tested. This might involve creating media with a mannitol concentration lying somewhere between MMM and SFM, as well as one with a higher concentration than SFM and one with a lower concentration than MMM. Examining the total hyphal length, segment lengths and number of branches for bacteria grown with such media could provide support for the hypothesis and enable direct comparison with simulation results. It might also be possible to chemically buffer the concentration of nutrient by having a high concentration of reactant that cannot be metabolised by the bacteria

and an enzyme system that breaks it down to a metabolisable nutrient. By choosing a suitable system it should be possible to effectively remove (or reduce) the diffusion barrier and allow a dense pattern of cells to emerge.

Mechanistic model

We believe the mechanistic model of key component production and transport also holds much promise. As well as further exploring the parameter space of the model as it stands, there are a number of possible improvements that could be made:

- Merging with the agent-based model - because the agents are filaments, it would be relatively easy to change their rules to obey extension and branching according to the mechanistic model of key component transport. Partly this would be a cosmetic change, providing a 2-D representation of the growing virtual bacteria, but additionally this would incorporate substrate depletion into the model.

- Modelling septa - currently, we do not model septa formation. This could have a significant effect on the model, depending on the assumptions we make about what happens as the key component reaches a septum. Would the septa prevent movement of the component from one compartment to another, or would some form of transport be allowed?

- Modelling other components - we have already suggested that Scy may have a suppressing effect on new branches. But, as discussed in Chapter 2, the protein DivIVA seems to have a role in selection of branching sites. It would be possible to incorporate DivIVA aggregation into our model. Additionally, it might be more realistic to model the build up of Scy, rather than having instant suppression as in the current model.

7.3 Conclusion

Streptomyces coelicolor is a fascinating model organism with a complex lifecycle. There is still much to discover about the mechanisms of its growth and branching and the opportunity to study it for the last three years has been both challenging

and rewarding. We hope that the work contained within this thesis will contribute towards a better understanding of the bacterium's early stage morphological development. It will be interesting to see how models develop in the future, as research sheds more light on the function of key proteins such as Scy, FilP, DivIA, and still others that remain to be characterised.

Bibliography

[1] H.L. Adams and C.R. Thomas. The use of image analysis for morphological measurements of filamentous microorganisms. *Biotechnology and Bioengineering*, 32:707–712, 1988.

[2] E.J. Allan and J.I. Prosser. Mycelial growth and branching of *Streptomyces coelicolor* A3(2) on solid medium. *Journal of General Microbiology*, 129:2029–2036, 1983.

[3] M. Alonso and E.J. Finn. *Physics*. Addison Wesley, 1992.

[4] S. Bagchi, H. Tomenius, L. M. Belova, and N. Ausmees. Intermediate filament-like proteins in bacteria and a cytoskeletal function in *Streptomyces*. *Molecular Microbiology*, 70(4):10371050, 2008.

[5] S. Bartnicki-Garcia, F. Hergert, and G. Gierz. Computer simulation of fungal morphogenesis and the mathematical basis for hyphal (tip) growth. *Protoplasma*, 153:46–57, 1989.

[6] S.D. Bentley, K.F. Chater, A.M. Cerdeo-Trraga, G.L. Challis, N.R. Thomson, K.D. James, D.E. Harris, M.A. Quail, H. Kieser, D. Harper, A. Bateman, S. Brown, G. Chandra, C.W. Chen, M. Collins, A. Cronin, A. Fraser, A. Goble, J. Hidalgo, T. Hornsby, S. Howarth, C.H. Huang, T. Kieser, L. Larke, L. Murphy, K. Oliver, S. O'Neil, E. Rabbinowitsch, M.A. Rajandream, K. Rutherford, S. Rutter, K. Seeger, D. Saunders, S. Sharp, R. Squares, S. Squares, K. Taylor, T. Warren, A. Wietzorrek, J. Woodward, B.G. Barrell, J. Parkhill, and D.A. Hopwood. Complete genome sequence of the model actinomycete *Streptomyces coelicolor* A3(2). *Nature*, 417:141–147, 2002.

[7] M. Bezzi and A. Ciliberto. Modeling growth of filamentous microorganisms. *Comments on Theoretical Biology*, 8(6):563–585, 2003.

[8] J. Billingham and A.C. King. *Wave Motion*. Cambridge University Press, 2001.

[9] I. Blilou, J. Xu, M. Wildwater, V. Willemsen, I. Paponov, J. Friml, R. Heidstra, M. Aida, K. Palme, and B. Scheres. The PIN auxin efflux facilitator network controls growth and patterning in *Arabidopsis* roots. *Nature*, 433:39–44, 2005.

[10] S. Bradbury and B. Bracegirdle. *Introduction to Light Microscopy*. BIOS Scientific Publishers, Oxford, 1998.

[11] K.F. Chater and R. Losick. Mycelial life style of *Streptomyces coelicolor* A3(2) and its relatives. In *Bacteria as Multicellular Organisms*. Oxford University Press, 1997.

[12] T. Christiansen, A.B. Spohr, and J. Nielsen. On-line study of growth kinetics of single hyphae of *Aspergillus oryzae* in a flow-through cell. *Biotechnology and Bioengineering*, 63(2):147–153, 1998.

[13] P.W. Cox, G.C. Paul, and C.R. Thomas. Image analysis of the morphology of filamentous micro-organisms. *Microbiology*, 144:817–827, 1998.

[14] R.A. Daniel and J. Errington. Control of cell morphogenesis in bacteria: Two distinct ways to make a rod-shaped cell. *Cell*, 113:767–776, 2003.

[15] J.F. Drouin, L. Louvel, B. Vanhoutte, H. Vivier, M.N. Pons, and P. Germain. Quantitative characterization of cellular differentiation of *Streptomyces ambofaciens* in submerged culture by image analysis. *Biotechnology Techniques*, 11(11):819–824, 1997.

[16] E. Ferret, J.H. Siméon, P. Molin, H. Jorquera, G. Acuña, and R. Giral. Macroscopic growth of filamentous fungi on solid substrate explained by a microscopic approach. *Biotechnology and Bioengineering*, 65(5):512–522, 1999.

[17] K. Flärdh. Essential role of DivIVA in polar growth and morphogenesis in *Streptomyces coelicolor* A3(2). *Molecular Microbiology*, 49(6):15231536, 2003.

[18] K. Flärdh. Growth polarity and cell division in *Streptomyces*. *Current Opinion in Microbiology*, 6:564–571, 2003.

[19] K. Flärdh and M.J. Buttner. *Streptomyces* morphogenetics: dissecting differentiation in a filamentous bacterium. *Nature Reviews Microbiology*, 7:36–49, 2009.

[20] F. Flett, J. Platt, and S.G. Oliver. Isolation and characterization of temperature-sensitive mutants of *Streptomyces coelicolor* A3(2) blocked in macromolecular synthesis. *Journal of General Microbiology*, 138:579–585, 1992.

[21] M.H. Friedman. *Principles and Models of Biological Transport*. Springer, 2nd edition, 2008.

[22] G. Gierz and S. Bartnicki-Garcia. A three-dimensional model of fungal morphogenesis based on the vesicle supply center concept. *Journal of Theoretical Biology*, 208:151–164, 2001.

[23] R.C. Gonzalez and R.E. Woods. *Digital Image Processing*. Pearson Prentice-Hall, 3rd edition, 2008.

[24] A. Goriely, G. Károlyi, and M. Tabor. Growth induced curve dynamics for filamentary micro-organisms. *Journal of Mathematical Biology*, 51:355–366, 2005.

[25] A. Goriely and M. Tabor. Biomechanical models of hyphal growth in actinomycetes. *Journal of Theoretical Biology*, 222:211–218, 2003.

[26] N.A.R. Gow and G.M.Gadd. *The Growing Fungus*. Chapman & Hall, 1995.

[27] N. Grantcharova, W. Ubhayasekera, S.L. Mowbray, J.R. McCormick, and K. Flärdh. A missense mutation in *ftsZ* differentially affects vegetative and developmentally controlled cell division in *Streptomyces coelicolor* A3(2). *Molecular Microbiology*, 47:645–656, 2003.

[28] D.I. Gray, G.W. Gooday, and J.I. Prosser. Apical hyphal extension in *Streptomyces coelicolor* A3(2). *Journal of General Microbiology*, 136:1077–1084, 1990.

[29] V.A. Grieneisen, J. Xu, A.F.M. Mareé, P. Hogeweg, and B. Scheres. Auxin transport is sufficient to generate a maximum and gradient guiding root growth. *Nature*, 449(25):1008–1013, 2007.

[30] L.H. Grimm, S. Kelly, R. Krull, and D.C. Hempel. Morphology and productivity of filamentous fungi. *Applied Microbiology and Biotechnology*, 69:375–384, 2005.

[31] T. Guénault. *Statistical Physics*. Chapman & Hall, 1995.

[32] B. Gust, G.L. Challis, K. Fowler, T. Kieser, and K.F. Chater. PCR-targeted *Streptomyces* gene replacement identifies a protein domain needed for biosynthesis of the sesquiterpene soil odor geosmin. *Proceedings of the National Academy of Sciences USA*, 100:1541–1546, 2003.

[33] A.M. Hempel, S. Wang, M. Letek, J.A. Gil, and K. Flärdh. Assemblies of DivIVA mark sites for hyphal branching and can establish new zones of cell wall growth in *Streptomyces coelicolor*. *Journal of Bacteriology*, 190(22):7579–7583, 2008.

[34] N. Hirokawa. Kinesin and dynein superfamily proteins and the mechanism of organelle transport. *Science*, 279:519–526, 1998.

[35] D.A. Hodgson. Glucose repression of carbon source uptake and metabolism in *Streptomyces coelicolor* A3(2) and its perturbation in mutants resistant to 2-deoxyglucose. *Journal of General Microbiology*, 128:2417–2430, 1982.

[36] D.A. Hopwood. Phase-contrast observations on *Streptomyces coelicolor*. *Journal of General Microbiology*, 22:295–302, 1960.

[37] D.A. Hopwood. *Streptomyces in Nature and Medicine*. Oxford University Press, 2007.

[38] V. Jyothikumar, E.J. Tilley, R. Wali, and P.R. Herron. Time-lapse microscopy of *Streptomyces coelicolor* growth and sporulation. *Applied and Environmental Microbiology*, 74(21):6774–6781, 2008.

[39] G.H. Kelemen, J. Walshaw, A. Thibessard, N. Holmes, K.A. Dalton, R.M. Leggett, M. Gillespie, A. Hemmings, B. Gust, and J. Hunter. Scy, a novel

bacterial protein scaffold for polarised growth, tip architecture and hyphal geometry. In preparation.

[40] T. Kieser, M.J. Bibb, M.J. Buttner, K.F. Chater, and D.A. Hopwood. *Practical Streptomyces Genetics*. The John Innes Foundation, 2000.

[41] A.L. Koch. The problem of hyphal growth in *Streptomyces* and fungi. *Journal of Theoretical Biology*, 171:137–150, 1994.

[42] S. Kretschmer. Stepwise increase of elongation rate in individual hyphae of *Streptomyces granaticolor* during outgrowth. *Journal of Basic Microbiology*, 28:35–43, 1988.

[43] S. Kretschmer. Septation behaviour of the apical cell in *Streptomyces granaticolor* mycelia. *Journal of Basic Microbiology*, 29(9):587–595, 1989.

[44] S. Kretschmer. Correlation between branching and elongation in germ tubes of *Streptomyces granaticolor*. *Journal of Basic Microbiology*, 31(4):259–264, 1991.

[45] S. Kretschmer. Location of branches within the apical hyphal region of *Streptomyces granaticolor* mycelia. *Journal of Basic Microbiology*, 32:35–42, 1992.

[46] C. Kummer and S. Kretschmer. DNA replication is not restricted to specific regions in young vegetative *Streptomyces* mycelia. *Journal of Basic Microbiology*, 26(1):27–31, 1986.

[47] L. Lam, S. Lee, and C.Y. Suen. Thinning methodologies - a comprehensive survey. *IEEE Transactions on Pattern Analysis and Machine Intelligence*, 14(9):869–885, 1992.

[48] J.A. Laszlo and R.W. Silman. Cellular automata simulations of fungal growth on solid substrates. *Biotechnology advances*, 11:621–633, 1993.

[49] R. Lejeune and G.V. Baron. Simulation of growth of a filamentous fungus in 3 dimensions. *Biotechnology and Bioengineering*, 53:139–150, 1997.

[50] R. Lenarcic, S. Halbedel, L. Visser, M. Shaw, L.J. Wu, J. Errington, D. Marenduzzo, and L.W. Hamoen. Localisation of DivIVA by targeting to negatively curved membranes. *The EMBO Journal*, 28(15):2272–2282, 2009.

[51] O. Leyser. Dynamic integration of auxin transport and signalling. *Current Biology*, 16:R424–33, 2006.

[52] G. Liu, M. Xing, and Q. Han. A population-based morphologically structured model for hyphal growth and product formation in streptomycin fermentation. *World Journal of Microbiology and Biotechnology*, 21:1329–1338, 2005.

[53] The Mathworks. Matlab R2008b Curve Fitting Toolbox. Product website at `http://www.mathworks.co.uk/products/curvefitting/`.

[54] P. Mazza, E.E. Noens, K. Schirner, N. Grantcharova, A.M. Mommaas, H.K. Koerten, G. Muth, G.P. Flärdh, K. amd van Wezel, and W. Wohlleben. MreB of *Streptomyces coelicolor* is not essential for vegetative growth but is required for the integrity of aerial hyphae and spores. *Molecular Microbiology*, 60(4):838–852, 2006.

[55] J.R. McCormick, E.P. Su, A. Driks, and R. Losick. Growth and viability of *Streptomyces coelicolor* mutant for cell division gene *ftsZ*. *Molecular Microbiology*, 14(2):243–254, 1994.

[56] M. McIntyre, D.R. Berry, J.K. Eade, P.W. Cox, C.R. Thomas, and B. McNeil. Manual and semi-automated morphological analysis of *Penicillium chrysogenum* chemostat cultures. *Biotechnology Techniques*, 12(9):671–675, 1998.

[57] J. Meyerhoff, V. Tiller, and K.-H. Bellgardt. Two mathematical models for the development of a single microbial pellet. *Bioprocess Engineering*, 12:305–313, 1994.

[58] E.M. Miguélez, C. Martín, C. Hardisson, and M.B. Manzanal. Synchronous germination of *Streptomyces antibioticus* spores: Tool for the analysis of hyphal growth in liquid cultures. *FEMS Microbiology Letters*, 109:123129, 1993.

[59] D. Moore, J. McNulty, and A. Meškauskas. Branching in fungal hyphae and fungal tissues: Growing mycelia in a desktop computer. In J.A. Davies, editor, *Branching Morphogenesis*, chapter 4. Springer-Verlag, New York, 2005.

[60] C.W. Mullineaux, A. Nenninger, N. Ray, and C. Robinson. Diffusion of green fluorescent protein in three cell environments in *Escherichia Coli*. *Journal of Bacteriology*, 188:3442–3448, 2006.

[61] J. Nielsen. A simple morphologically structured model describing the growth of filamentous microorganisms. *Biotechnology and Bioengineering*, 41:715–727, 1993.

[62] J. Nielsen. Modelling the morphology of filamentous microorganisms. *Trends in Biotechnology*, 14:438–443, 1996.

[63] E.E. Noens, V. Mersinias, J. Willemse, B.A. Traag, E. Laing, K.F. Chater, C.P. Smith, H.K. Koerten, and G.P. van Wezel. Loss of the controlled localization of growth stage-specific cell-wall synthesis pleiotropically affects developmental gene expression in an *ssgA* mutant of *Streptomyces coelicolor*. *Molecular Microbiology*, 64(5):1244–1259, 2007.

[64] J.R. Parker. *Practical Computer Vision Using C*. Wiley, 1994.

[65] G.C. Paul and C.R. Thomas. Characterisation of mycelial morphology using image analysis. *Advances in Biochemical Engineering/Biotechnology*, 60:1–59, 1998.

[66] M.N. Pons, J.F. Drouin, L. Louvel, B. Vanhoutte, H. Vivier, and P. Germain. Physiological investigations by image analysis. *Journal of Biotechnology*, 65:3–14, 1998.

[67] J.I. Prosser and A.J. Tough. Growth mechanisms and growth kinetics of filamentous microorganisms. *Critical Reviews in Biotechnology*, 10:253–274, 1991.

[68] U. Reichl, T.K. Buschulte, and E.D. Gilles. Study of the early growth and branching of *Streptomyces tendae* by means of an image processing system. *Journal of Microscopy*, 158:55–62, 1990.

[69] C. Reynaga-Peña, G. Gierz, and S. Bartnicki-Garcia. Analysis of the role of the Spitzenkörper in fungal morphogenesis by computer simulation of apical

branching in *Aspergillus niger*. *Proceedings of the National Academy of Sciences USA*, 94:9096–9101, 1997.

[70] M. Riquelme and S. Bartnicki-Garcia. Key differences between lateral and apical branching in hyphae of *Neurospora crassa*. *Fungal Genetics and Biology*, 41:842–851, 2004.

[71] M. Riquelme, C. Reynaga-Peña, G. Gierz, and S. Bartnicki-Garcia. What determines growth direction in fungal hyphae? *Fungal Genetics and Biology*, 24:101–109, 1998.

[72] G. Robson. *Molecular fungal biology*. Cambridge University Press, 1999.

[73] E.D. Salmon, W.M. Saxton, R.J. Leslie, M.L. Karow, and J.R. McIntosh. Diffusion coefficient of fluorescein-labeled tubulin in the cytoplasm of embryonic cells of a sea urchin: video image analysis of fluorescence redistribution after photobleaching. *The Journal of Cell Biology*, 99:2157–2164, 1984.

[74] J. Schwedock, J.R. McCormick, E.R. Angert, J.R. Nodwell, and R. Losick. Assembly of the cell division protein FtsZ into ladder-like structures in the aerial hyphae of *Streptomyces coelicolor*. *Molecular Microbiology*, 25(5):847–858, 1997.

[75] F. Soddell, R. Seviour, and J. Soddell. Using Lindenmayer systems to investigate how filamentous fungi may produce round colonies. *Complexity International*, 2, 1995.

[76] M. Sonka, V. Hlavac, and R. Boyle. *Image Processing, Analysis, and Machine Vision*. PWS Publishing, 1999.

[77] S.R. Sternberg. Biomedical image processing. *IEEE Computer*, January 1983.

[78] P. Stevens and R. Pooley. *Using UML: Software engineering with Objects and Components*. Addison Wesley, 2000.

[79] K. Sugden, M.R. Evans, and W.C.K. Poon. A stochastic model for hyphal growth. Technical Report NI06027-PDS, Isaac Newton Institute for Mathe-

matical Sciencs programme on Principles of the Dynamics of Non-Equilibrium Systems, 2006.

[80] C.R. Thomas and G.C. Paul. Applications of image analysis in cell technology. *Current Opinion in Biotechnology*, 7:35–45, 1996.

[81] S.H. Tindemans, N. Kern, and B.M. Mulder. The diffusive vesicle supply center model for tip growth in fungal hyphae. *Journal of Theoretical Biology*, 238:937–948, 2006.

[82] G.A. Truskey, F. Yuan, and D.F. Katz. *Transport phenomena in biological systems*. Pearson Prentice-Hall, 2009.

[83] K.G. Tucker, T. Kelly, P Delgrazia, and C.R. Thomas. Fully-automatic measurement of mycelial morphology by image analysis. *Biotechnology Progress*, 8(4):353359, 1992.

[84] R.D. Vale. The molecular motor toolbox for intracellular transport. *Cell*, 112:467–480, 2003.

[85] H. Yang, R. King, U. Reichl, and E.D. Gilles. Mathematical model for apical growth, septation and branching of mycelial microorganisms. *Biotechnology and Bioengineering*, 39:49–58, 1992.

[86] T.Y. Zhang and C.Y. Suen. A fast parallel algorithm for thinning digital patterns. *Communications of the ACM*, 27(3):236–239, 1984.

[87] R.W. Zhou, C. Quek, and G.S. Ng. A novel single-pass thinning algorithm and an effective set of performance criteria. *Pattern Recognition Letters*, 16:1267–1275, 1995.

Appendix A

Media Recipes

A.1 MMM - Minimal Medium Mannitol

The following ingredients are for making four 400 ml bottles:

L-asparagine	0.8 g	0.5 g/l	3.78 mM
K_2HPO_4	0.8 g	0.5 g/l	2.87 mM
$MgSO_4.7H_2O$	0.32 g	0.2 g/l	0.81 mM
$FeSO_4.7H_2O$	0.016 g	0.01 g/l	0.04 mM
Mannitol	8.0 g	5 g/l	27.45 mM
Deionized H_2O	1 l		
Agar	16 g	10 g/l	

Procedure for making medium:

1. Weigh all chemicals using an analytical balance and dissolve in 1 litre of deionized water.
2. Adjust pH to 7.0-7.2 by addition of small amounts of Phosphoric Acid.
3. Make solution up to 1.6 litres with deionized water.
4. Prepare 4 bottles and measure 4 g agar into each.
5. Decant 400 ml of solution into each bottle.
6. Sterilise in autoclave.

A.2 SFM - Soya Flour Mannitol Medium

The following ingredients are for 500 ml bottles:

Mannitol	60 g	120 g/l	658.73 mM
Agar	6 g	12 g/l	
Soya flour	6 g	12 g/l	
Tap water	300 ml		

Procedure for making medium:

1. Add 6 g of agar and soya flour to each bottle.
2. Dissolve mannitol in the tap water.
3. Add 300 ml of dissolved mannitol to each bottle.
4. Sterilise in autoclave.
5. Swirl contents of bottle
6. Autoclave for a second time.

A.3 LB - Lennox Broth Medium

The following ingredients are for making four 400 ml bottles:

Bacto tryptone	16 g	10 g/l	
Yeast extract	8 g	5 g/l	
NaCl	8 g	5 g/l	85.56 mM
Glucose	1.6 g	1 g/l	5.55 mM
Deionized H_2O	1.6 l		

Procedure for making medium:

1. Weigh all chemicals using an analytical balance and dissolve in 1.6 litres of deionized water.
2. Prepare 4 bottles and measure 4 g agar into each.
3. Decant 400 ml of solution into each bottle.
4. Sterilise in autoclave.

Appendix B

Skeletonization Algorithms

B.1 Terminology

In this appendix, we provide a more detailed definition of the two skeletonization algorithms referred to in Chapter 4. The descriptions are based on those provided in [86] and [87].

In the descriptions that follow, we assume that we have a monochrome image represented by an m-by-n array of pixels, $P_{m,n}$, in which a pixel is either set (1) or clear (0). In the case of the Zhou *et al.* algorithm only, there is also a corresponding flag map, $Q_{m,n}$, used to mark pixels for future removal.

When considering a single pixel, we use the symbol P_0 to denote the pixel $P_{i,j}$ and the symbols P_1, P_2, P_3, P_4, P_5, P_6, P_7 and P_8 to denote the pixels in the 8-neighbourhood around P_0. In the Zhou *et al.* algorithm, the correponding locations in the flag map are denoted by the symbols Q_0 to Q_8 (Figure B.1).

Figure B.1: Symbols used in the sksletonization algoritms: (a) Symbols used to represent a pixel, P_0, in the bitmap and its 8 neighbours. (b) For the Zhou *et al.* algorithm, symbols used to represent corresponding positions in the flag map.

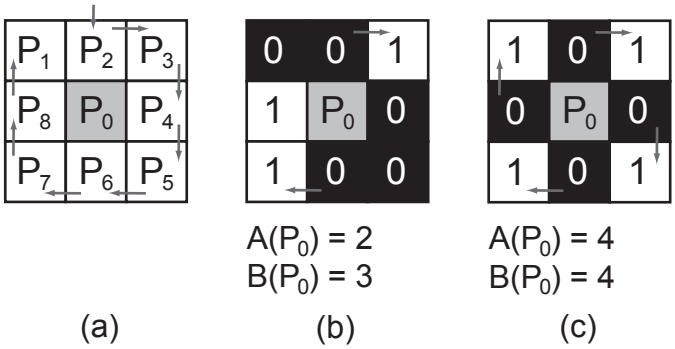

Figure B.2: Calculation of $A(P_0)$ and $B(P_0)$: (a) $A(P_0)$ is the number of 01 patterns moving clockwise from P_2 back round to P_1, while $B(P_0)$ is the number of set pixels in the 8-neighbourhood. (b) and (c) show example calculations.

B.2 Zhang and Suen algorithm

Zhang and Suen define the following two functions:

- $A(P_0)$ is the number of 01 patterns in the ordered set P_2, ..., P_8, P_1 that are the neighbours of P_0 (Figure B.2).
- $B(P_0)$ is the number of set neighbours of pixel P_0 in the 8-neighbourhood.

The algorithm proceeds as follows:

1. For each set pixel P in the bitmap do the following:
   (a) Compute $A(P)$ and $B(P)$.
   (b) Delete pixel P if the following conditions are all met:
      - Condition 1: $2 \leq B(P_0) \leq 6$
      - Condition 2: $A(P_0) = 1$
      - Condition 3: $P_2 * P_4 * P_6 = 0$
      - Condition 4: $P_4 * P_6 * P_8 = 0$
   (c) Or delete pixel P if the following conditions are all met:
      - Condition 1: $2 \leq B(P_0) \leq 6$
      - Condition 2: $A(P_0) = 1$
      - Condition 3: $P_2 * P_4 * P_8 = 0$
      - Condition 4: $P_2 * P_6 * P_8 = 0$
2. Repeat until no pixel can be deleted.

B.3 Zhou *et al.* algorithm

Unlike the previous algorithm, this one makes use of a flag map. To begin, every position in the flag map Q is set to 1. During execution of the algorithm, a position may be set to zero to indicate the corresponding pixel is flagged for deletion. Zhou *et al.* define the following three functions:

- $CN(P)$ is the current neighbourhood function. It is the number of set pixels in the 8-neighbourhood around pixel P.

$$CN(P_0) = \sum_{i=1}^{8} P_i \times Q_i \tag{B.1}$$

  where $\times$ denotes the logical 'and' operator and is included to indicate exclusion of flagged pixels in Q from the count.

- $PN(P)$ is the previous neighbourhood function. It is the number of set pixels in the 8-neighbourhood around pixel P on the previous iteration of the algorithm.

$$PN(P_0) = \sum_{i=1}^{8} P_i \tag{B.2}$$

- $Trans(P)$ is the "$0 \rightarrow 1$" transition function, used to measure the connectivity within the immediate neighbourhood of the pixel.

$$Trans(P_0) = \sum_{i=1}^{8} count(P_i) \tag{B.3}$$

  where $count(P_i)$ is 1 if $(P_i \times Q_i) = 0$ and $(P_{i+1} \times Q_{i+1}) = 1$, or 0 otherwise. and $P_9 = P_1, Q_9 = Q_1$.

The algorithm then proceeds as follows:

1. For each set pixel P in the bitmap do the following:

   (a) Count $PN(P)$, $CN(P)$ and $Trans(P)$.

   (b) If P satisfies Condition 1 and (Condition 2 or Condition 3) of the following conditions, then it is a boundary pixel, so flag it.

   - Condition 1: $(CN(P) > 1)$ and $(CN(P) < 6)$
   - Condition 2: $(Trans(P) == 1)$
   - Condition 3: P and its neighbours match one of the templates in Figure B.3

2. Delete the flagged pixels.

3. Repeat steps 1 and 2 until no pixel can be deleted.

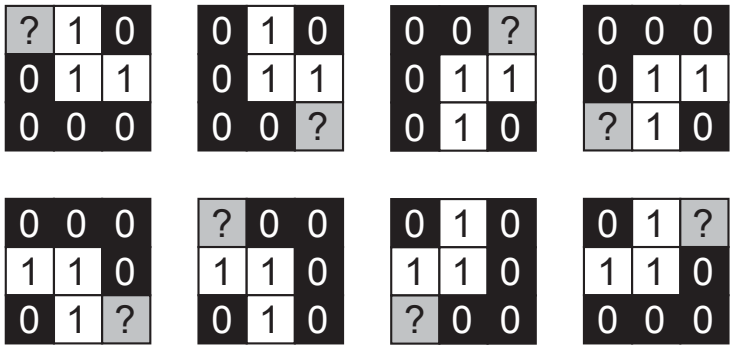

Figure B.3: Templates used in the Zhou *et al.* algorithm: These represent special cases which are not collected by conditions 1 and 2 of algorithm step 2. For each location in the template marked with a 1 or 0, we must find the same value in the corresponding position in P and its neighbours for the template to match. Locations marked with ? may be either set or clear. If a template match is found, the central pixel P can be removed without affecting connectivity.

Appendix C

JFilamentAnalyser

C.1 Summary

This appendix contains additional information on the design and implementation of the JFilamentAnalyer tool which was described briefly in Chapter 4.

Section C.2 provides further description on the use of the application, along with a number of screenshots of it running. Sections C.3 and C.4 provide descriptions of the format of the various files used to store filament data and biometrics.

C.2 Use of the tool

Figure C.1 shows the initial screen presented to the user after loading JFilamant-Analyser. After clicking on the Wizard icon in the toolbar, the user moves through the screens shown in Figures C.2 to C.7.

Filament files (Section C.3) are used to store the location of all pixels that make up the filament skeleton, as well as locations of all tip, branch and spore points. Statistics and biometrics are not contained within filament files, but are contained within a separate set of files (Section C.4). This separation is maintained for two reasons. Firstly, it makes it easier to add new biometrics to the tool and to obtain the results without repeating the initial supervised image processing steps. Secondly, some statistics make most sense at an experiment level across multiple bacteria, rather than at the level of an individual bacterium.

Because of the separation of filament file and statistics file, a batch tool is pro-

vided, which allows the user to re-run the biometric and statistics gathering over a series of filament files and to save the output into one set of statistics files. The dialog box for this is shown in Figure C.8. Typically the results from one experiment's microscope images will be stored in one set of statistics files.

C.3 Filament files

Once images have been processed through the filament Wizard, the skeleton and point information is saved into a filament file with a .fil extension. This is a plain text file made up of the following elements:

- A header - the first line contains the phrase `FILAMENT_ANNONTATION`.
- A filename - the second line contains the filename of the image used to create the filament file.
- X scaling factor - multiplier to turn pixels into microns, eg. `XSCALING=0.07`.
- Y scaling factor - for our microscope, always the same as the X scaling factor.
- Skeleton pixels - a complete list of the co-ordinates of all pixels in the skeleton of the filament, beginning with the keyword `PIXELS`.
- Tip points - a list of the co-ordinates of all tip points, beginning with the keyword `TIP POINTS`.
- Branch points - a list of the co-ordinates of all branch points, beginning with the keyword `JUNCTION POINTS`.
- Spore point - the location of the spore point, beginning with the keyword `SPORES`.
- An end tag - the keyword `END` indicates the end of the file.

An example file is shown in Figure C.9. The filament file only contains descriptions of the points that make up the filament and not the biometrics and statistics for a given filament. Instead, these are saved into a separate file, either by selecting a menu option and specifying a filename, or by using the batch tool (C.8) which will

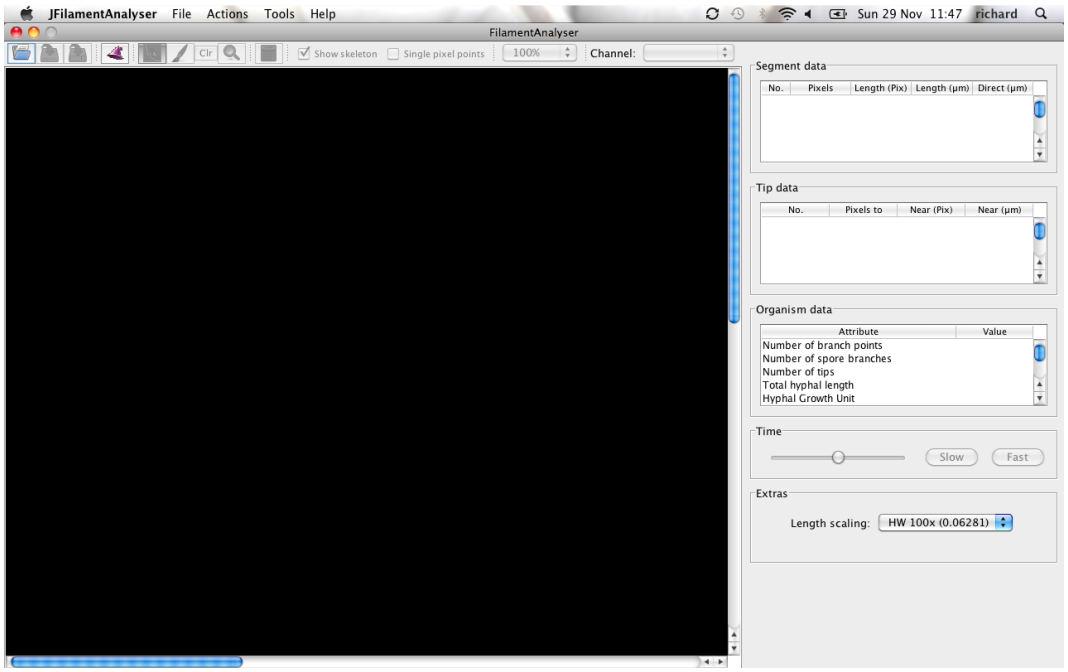

Figure C.1: The initial screen presented to the user after loading JFilamentAnalyser. The toolbar at the top of the screen lets the user load a previously analysed image, or to select the 'Wizard'.

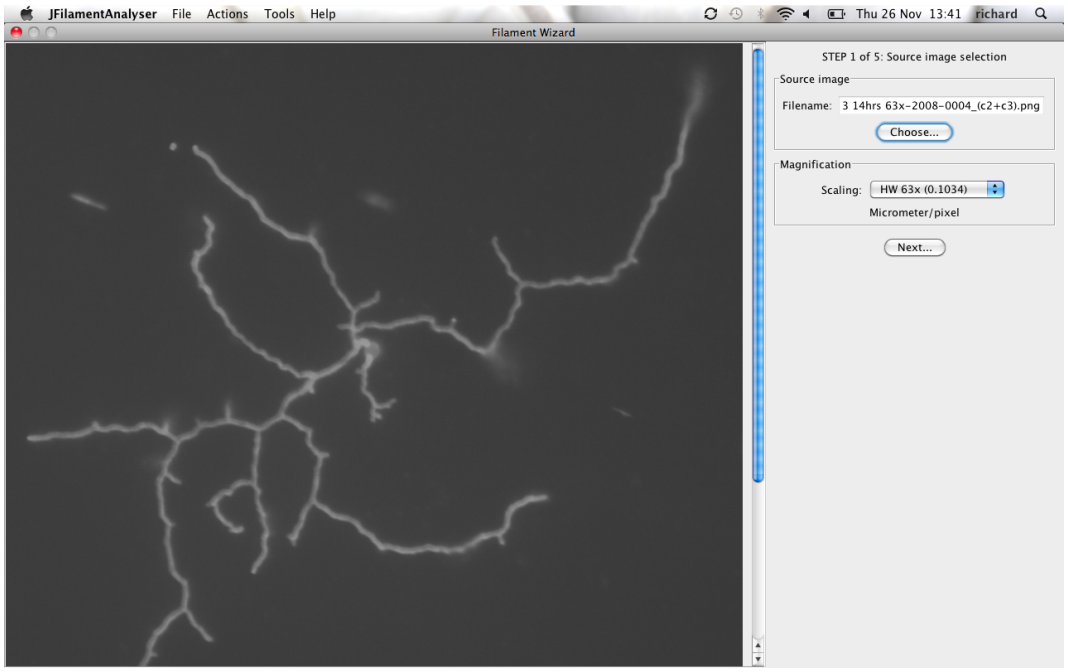

Figure C.2: Wizard step 1: The image is selected through a file browser dialog and the microscope magnification can be selected through a drop down menu. Clicking the Next icon moves to the next stage.

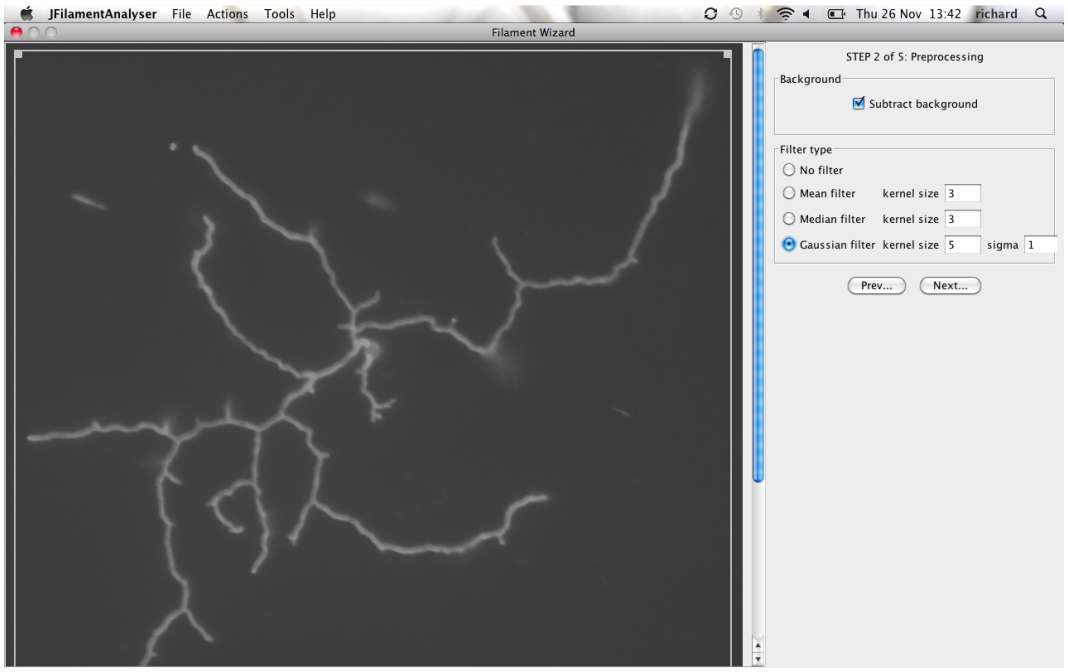

Figure C.3: Wizard step 2: The user can chose a cropping area by dragging the edges of the highlight rectangle. Pre-processing options are provided on the right hand side, but the defaults are usually appropriate.

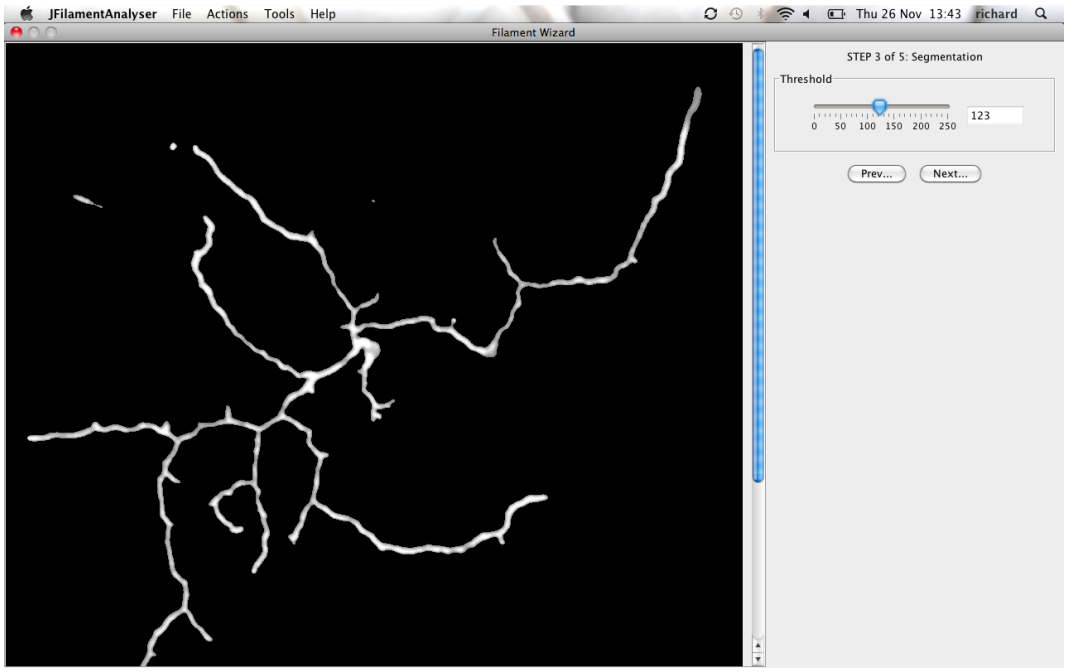

Figure C.4: Wizard step 3: The user selects the best segmentation threshold by dragging the slider. The main image updates in real-time as the threshold is changed.

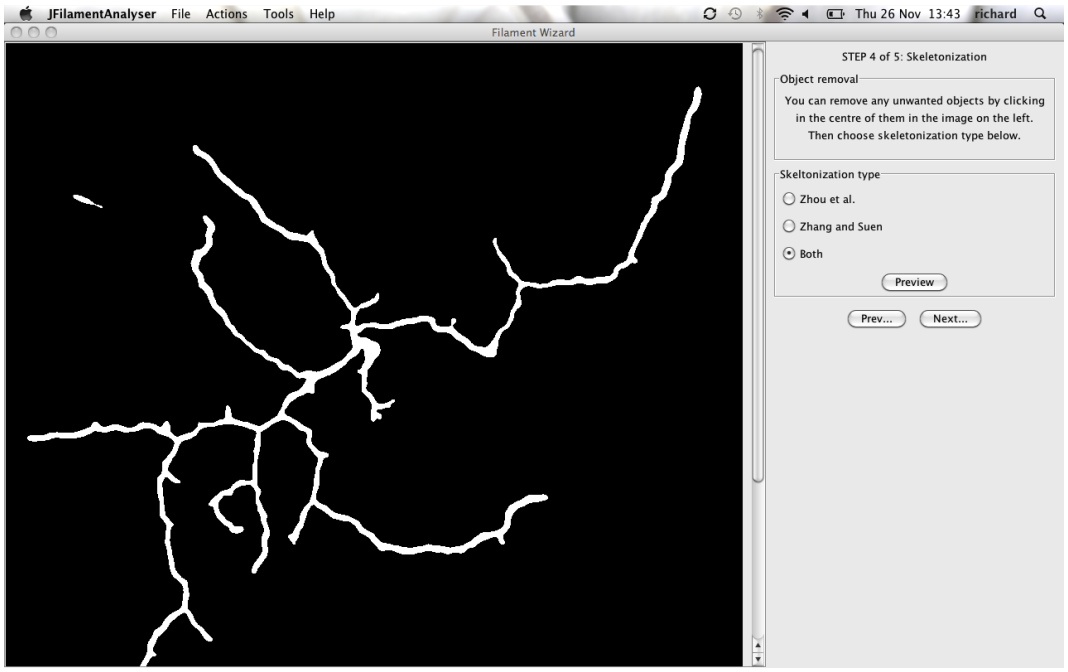

Figure C.5: Wizard step 4: Selection of skeletonization algorithms. It is usually appropriate to keep the default values. Clicking the Next button moves to the next stage.

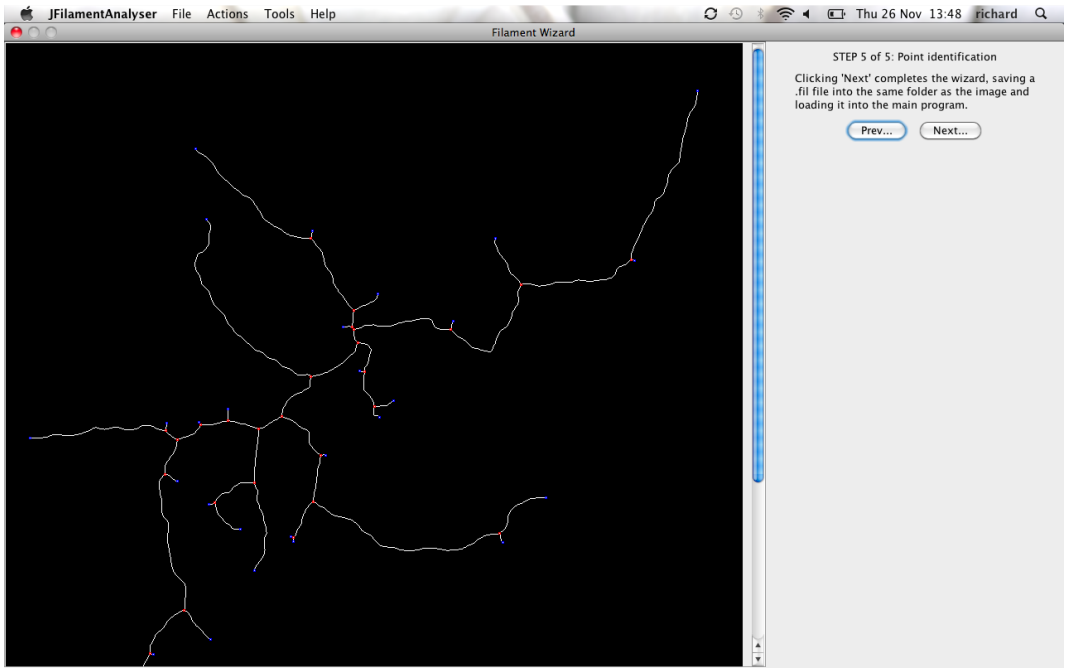

Figure C.6: Wizard step 5: The last stage of the Wizard. Tip points and branch points are highlighted. The user clicks the Next button if they are satisfied with the results, or can go back to previous stages if necessary.

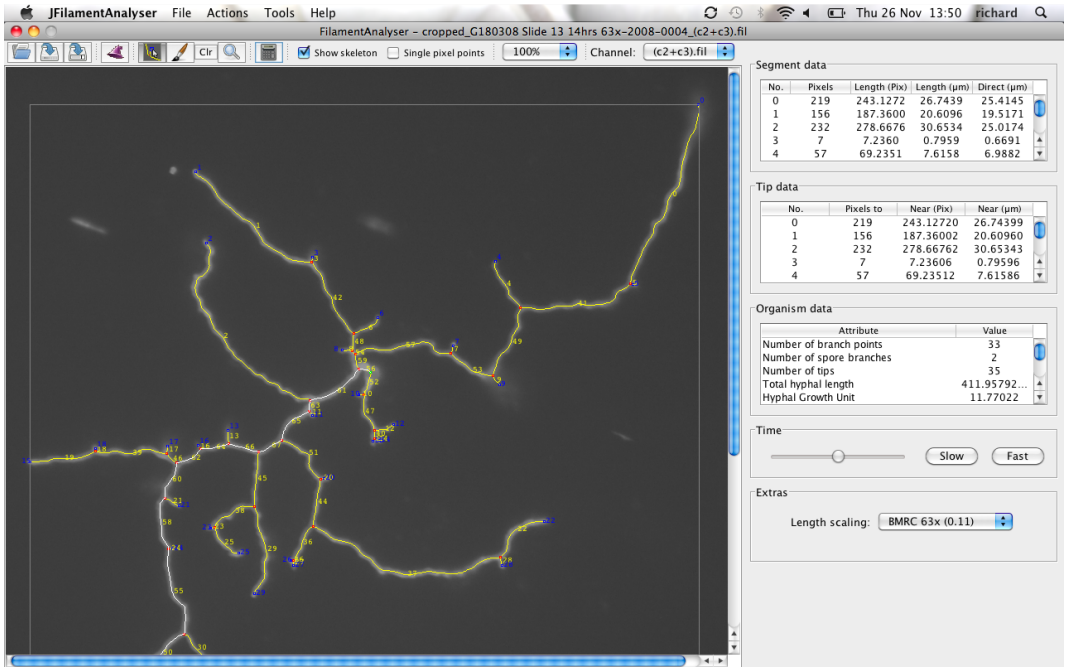

Figure C.7: After the Wizard completes, the user is returned to the main screen with the bacterium image loaded. The toolbar at the top of the screen provides a number of tools for editing the skeleton, changing the location of branch points and tip points and zooming in to the image. A drop down menu to the right of the toolbar allows the user to select a different channel image to view, with the skeleton overlaid on top.

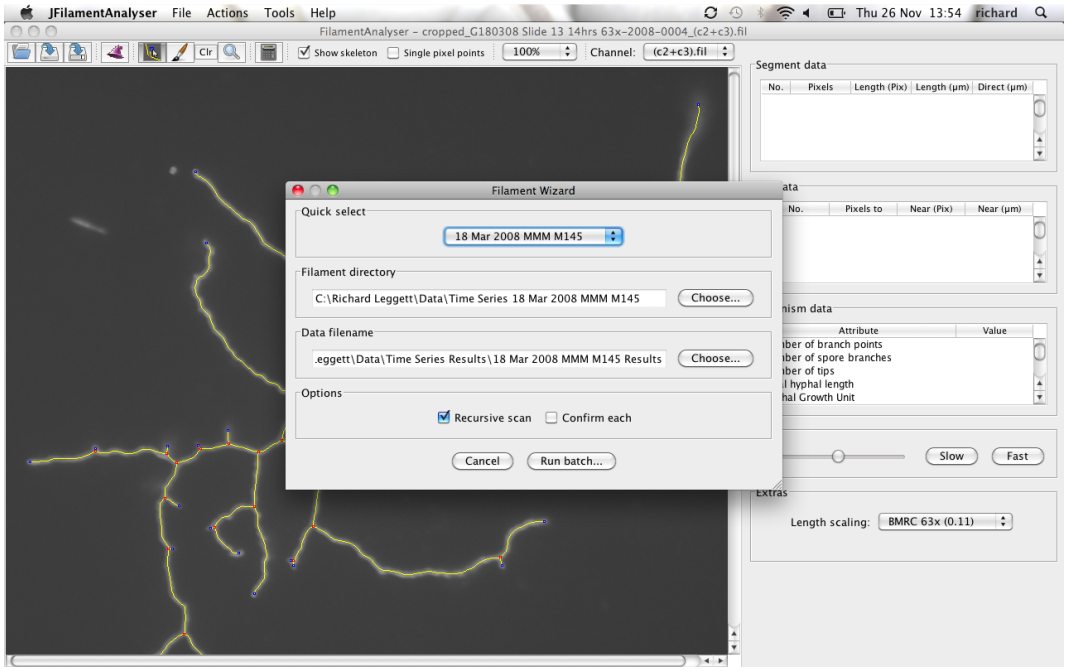

Figure C.8: The batch processing dialog box. In batch mode, the software will load a series of filament files, perform analysis and then append the results to a single file.

```
FILAMENT ANNOTATION
cropped_G180308 Slide 7 10hrs 100x-2008-0001_c1.png
XSCALING=0.07
YSCALING=0.07
PIXELS
64,34
65,34
...
92,219
92,220
TIP POINTS
69,35
92,220
100,89
JUNCTION POINTS
56,36
80,78
SPORES
56,36
END
```

Figure C.9: Example filament file. Note, skeleton pixels co-ordinates have been truncated to fit figure.

generate statistics for a set of filament files. The separation of the statistics into a separate file from the filament data allows the way statistics are calculated to be changed, or new statistics added, without the need to reanalyse microscope images.

C.4 Statistics files

When the user selects the option to write statistics data, the results are saved into a set of seven files. If the files already exist, results will be appended, otherwise a new set of files will be created. The files created or appended are:

- Results.csv - the main results file, consists of 35 columns of data, each containing a different biometric for the organism.
- Results_segments.csv - a file containing the segment length data.
- Results_subapical.csv - a file containing only subapical segment data.
- Results_tips.csv - a file containing tip to nearest branch data.
- Results_emergingtips.csv - a file containing emerging tip data.
- Results_apicalbranch.csv - a file containing apical branch data.
- Results_pairwise.csv - a file containing pairwise distance data.

```
Hour,FilamentName,NumBranches,NumSporeBranches,NumTips,TotalHyphalLen,HGU,InternalLength,MeanSegme...
10,G020708 I070708 MMM dscy 10hrs 100x-2008-0025,0,1,1,28.05347593012471,28.05347593012471,0.0,28....
10,G020708 I070708 MMM dscy 10hrs 100x-2008-0026a,0,1,1,12.735135249860678,12.735135249860678,0.0,...
...
18,G020708 I140708 MMM dscy 18hrs 63x-2008-0051,7,2,9,173.10251251283339,19.23361250142593,68.5030...
18,G020708 I140708 MMM dscy 18hrs 63x-2008-0054,2,1,3,115.7346588711113,38.57821962370377,33.61205...
```

(a)

```
FilamentName,Hour,SegmentLen,DirectLen,SubApical,THL
G020708 I070708 MMM dscy 10hrs 100x-0025,10,28.05347593012471,23.29912377013565,0,28.05347593012471
G020708 I070708 MMM dscy 10hrs 100x-0026a,10,12.735135249860678,9.50487773145978,0,12.735135249860678
...
G020708 I140708 MMM dscy 18hrs 63x-0054,18,13.664756704809387,11.056549960995971,0,115.7346588711113
G020708 I140708 MMM dscy 18hrs 63x-0054,18,33.612052377532784,25.304496209172,1,115.7346588711113
```

(b)

Figure C.10: Example statistics files: (a) The main results file contains multiple columns of biometrics, one line per organism. (b) The segments file contains length measurements for all segments, so there are multiple lines per organism.

Typically, we would append all the results from one time series experiment into one set of seven files, all sharing the same prefix - for example, `18Mar08_MMM_scy_Results`. The batch tool facilitates this by allowing the user to select a folder which is then recursively scanned for filament files. Each file found is analysed and the results appended to the statistics files. Generating statistics on a complete experimental set of a few hundred images typically takes around 30-60 minutes. Unlike the initial image processing stage, this process does not have to be supervised, so the computer may be left unattended.

C.4.1 The main results file

This file consists of a header row, followed by one row of data for each image. Figure C.10a shows an example section from a file, though it has been truncated to fit. The first and second columns specify the hour point and image filename respectively. The next 35 columns consist of various biometrics about the organism - for example, number of tips, total hyphal length, length of primary filament and so on.

C.4.2 The segments, tips and subapical files

The segments file (Figure C.10b) consists of a header row, followed by one row of data for each segment described. Thus, for anything but the simplest structure, there will be multiple rows of data per image. The file contains the following columns:

- FilamentName - the filename of the filament file, minus the .fil extension.
- Hour - the hour number for a time series, or 0 if not known.
- SegmentLen - the length, in microns, of the segment.
- DirectLen - the direct Euclidian distance, in microns, from one end of the segment to the other.
- SubApical - a flag field set to 1 if this is a subapical segment, or 0 if one of the ends is a tip point.
- THL - the total hyphal length of the organism this segment was taken from.

The subapical file and the tips file are subsets of the segments file, containing just the subapical and tip segments respectively. The only difference is the removal of the SubApical flag field which is thus rendered redundant.

C.4.3 The emerging tips file

The emerging tips file consists of a header row, followed by zero or more rows of data for each image. Each row contains information on one detected emerging tip. The file contains the following columns:

- FilamentName - the filename of the filament file, minus the .fil extension.
- Hour - the hour number for a time series, or 0 if not known.
- EmergingBranchLen - the length of the emerging tip, in microns.
- DistanceToTip - the distance, in microns, from the point of emergence to the tip of the parent filament.
- DistanceToBranch - the distance, in microns, from the point of emergence to the previous node on the parent filament.
- IsFirst - a flag indicating if it is the first branch on a germ tube (1) or not (0).
- THL - the total hyphal length of the organism this segment was taken from.

C.4.4 The apical branch file

The apical branch file consists of a header row, followed by zero or more rows of data for each image. Each row contains information on one pair (or trio) of apical tips that share the same branch point. The file contains the following columns:

- FilamentName - the filename of the filament file, minus the .fil extension.
- Hour - the hour number for a time series, or 0 if not known.
- THL - the total hyphal length of the organism this segment was taken from.
- NumTips - the number of tips that share the branch point.
- TipLength0..n - the length, in microns, of tip n.

C.4.5 The pairwise distance file

The pairwise file consists of a header row, followed by one row of data for each image. The file consists of the following columns:

- FilamentName - the filename of the filament file, minus the .fil extension.
- Hour - the hour number for a time series, or 0 if not known.
- THL - the total hyphal length of the organism this segment was taken from.
- NumTips - the number of tips for this organism.
- NumItems - the number of items of pairwise data.
- Items - NumItems columns of pairwise distance data.

Appendix D

Further Experimental Results

D.1 Bounding box area

The bounding box area is an alternative approach to the mean distance to centre (Section 5.12) for understanding the extent of the area covered by the bacteria. We define it to be the smallest rectangle capable of fitting the bacteria in its entirety. Figure D.1 provides graphs of bounding box area against total hyphal length.

Unsurprisingly, the bounding box area follows a similar pattern to the mean distance to centre (Section 5.12) and pairwise distances (Section 5.14), with the compact nature of the Δ*scy* and Δ*scy-filP* mutants manifesting as smaller bounding box areas than the wild-type on SFM.

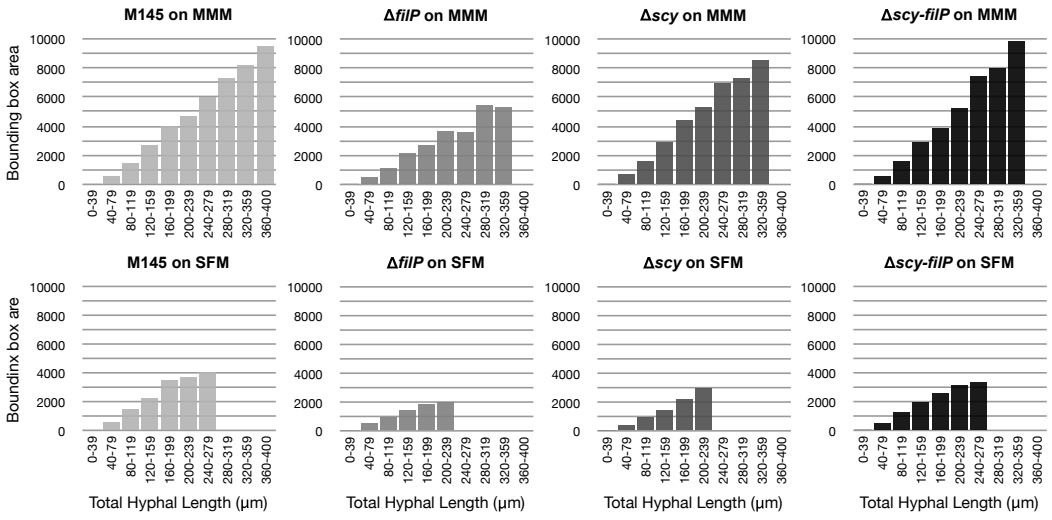

Figure D.1: Graph of bounding box area against total hyphal length.

D.2 Emerging tips

Figure D.2 provides histograms of the distances from emerging tips to the parent's tip. Figure D.3 provides histograms of the distances from emerging tips to the parent's previous branch. Table D.1 provides summary data, including mean values.

Jyothikumar *et al.* reported that branches formed on average 10.94 µm behind the tip [38] when growing *S. coelicolor* on a minimal medium. Though not an identical medium, this results is similar to our own value of 12.21 µm when growing on MMM.

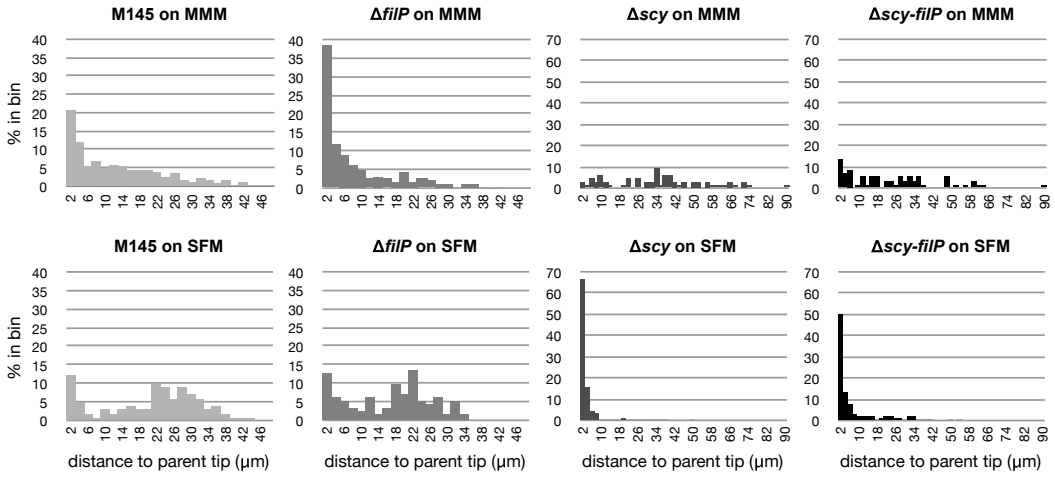

Figure D.2: Histograms of distances from emerging tips to the parent tip. Note different scales used for M145, Δ*filP* and Δ*scy*, Δ*scy-filP*.

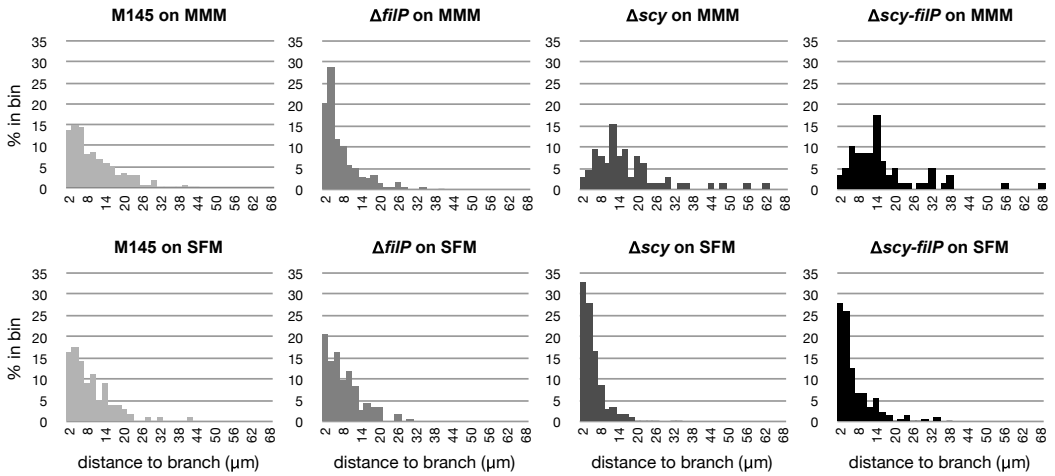

Figure D.3: Histograms of distances from emerging tips to the parent filament's previous branch.

Bacteria	Media	Emerging tip to parent tip Mean (µm)	Emerging tip to parent tip Longest (µm)	Emerging tip to previous node Mean (µm)	Emerging tip to previous node Longest (µm)
M145	MMM	12.21	46.13	9.96	43.77
M145	SFM	19.92	42.27	8.14	41.53
Δ*filP*	MMM	8.13	40.66	6.67	39.11
Δ*filP*	SFM	15.48	33.22	7.21	28.56
Δ*scy*	MMM	34.69	88.18	15.65	61.04
Δ*scy*	SFM	3.24	49.58	4.37	33.30
Δ*scy-filP*	MMM	23.31	89.59	15.51	67.29
Δ*scy-filP*	SFM	7.10	53.57	6.14	37.75

Table D.1: Table showing mean and longest distances from emerging tip to previous branch and from emerging tip to parent tip.

D.3 First branch position

Figure D.4 provides histograms of the length of the germ tube at the point of emergence of the first branch. As described in Section 4.4.2, our software looks for a small tip (less than 1.5µm) connected to a branch point, which in turn is connected to a spore point and a tip point. Figure D.5 provides histograms of relative position of the new branch, calculated in the same manner as for the emerging tips graphs in Section 5.10.

As we are only interested in the first branch, there is much less data available for this graph than for the emerging tips histogram. Thus, there are some holes, where data points are not available. Allowing for this, the graphs show a relatively similar distribution to the emerging tip graphs, but with slightly more bias towards shorter lengths for M145 on MMM.

D.4 Primary filament length

The length of the primary filament is calculated according to the method described in Section 4.4.1. Figure D.6 provides graphs of primary filament length against total hyphal length.

On MMM, M145 and the Δ*filP* mutant show similar rates of growth of the primary filament, while the Δ*scy* and Δ*scy-filP* mutants show slightly faster rates of growth. This may relate to the delayed onset of second germ tubes, described in

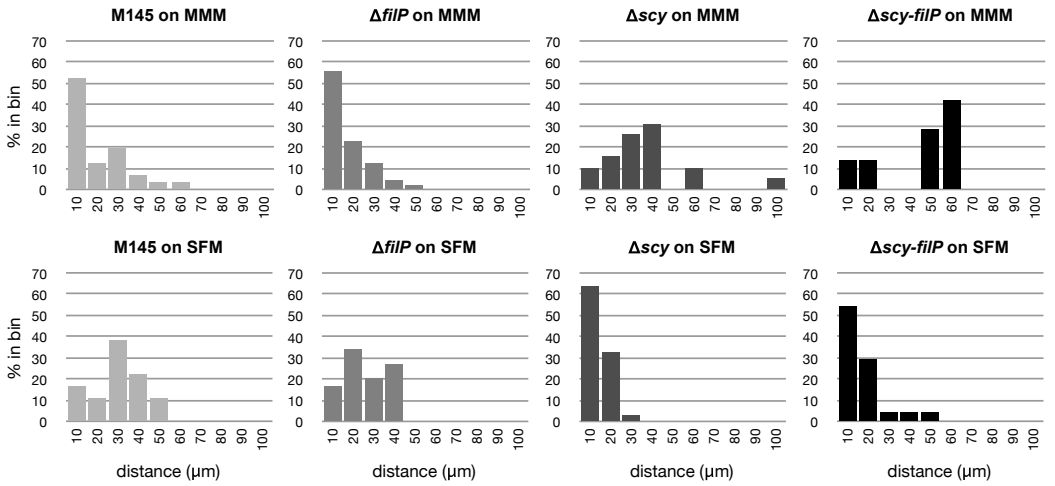

Figure D.4: Histograms of germ tube length at point of first branch emergence.

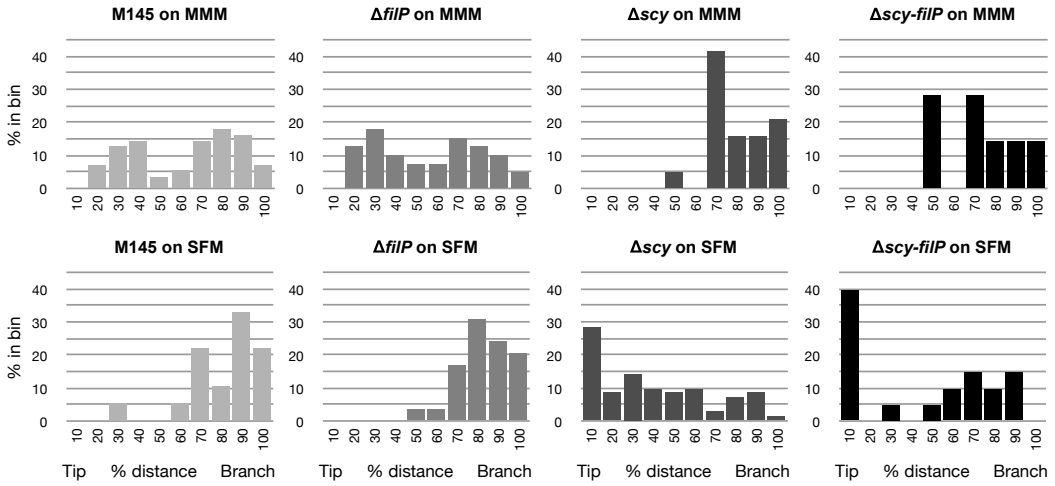

Figure D.5: Histograms of first branch position, relative to germ-tube length.

Section 5.8. On SFM, the Δ*scy* displays a lower rate of growth of primary filament than the wild-type, though surprisingly, the Δ*scy-filP* mutant seems similar.

D.5 Primary filament branches

Figure D.7 provides graphs of the number of branches on the primary filament against total hyphal length.

On MMM, we see substantially fewer branches on the primary filament for the Δ*scy* and Δ*scy-filP* mutants than for the wild-type and Δ*filP* mutant. This is the same as was observed for the overall total number of branches in Section 5.6. On SFM, the graphs seem slightly uncertain, with the Δ*scy* and Δ*scy-filP* mutants displaying more branches at lower THL (less than 160 μm) and a similar number at

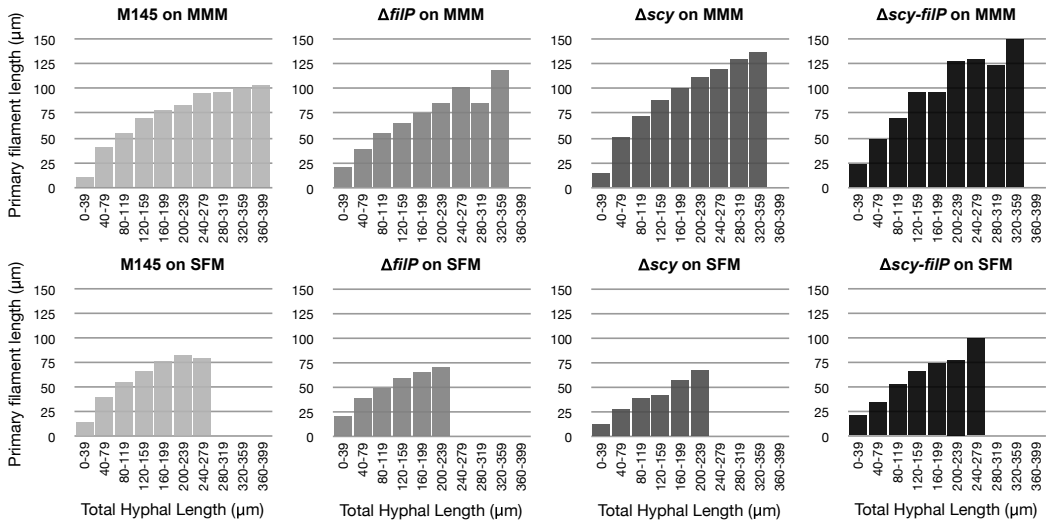

Figure D.6: Graphs of primary filament length against total hyphal length.

higher THL. It may be that the rate of branching is slowed by the delayed development of a second germ tube in the mutants (Section 5.8).

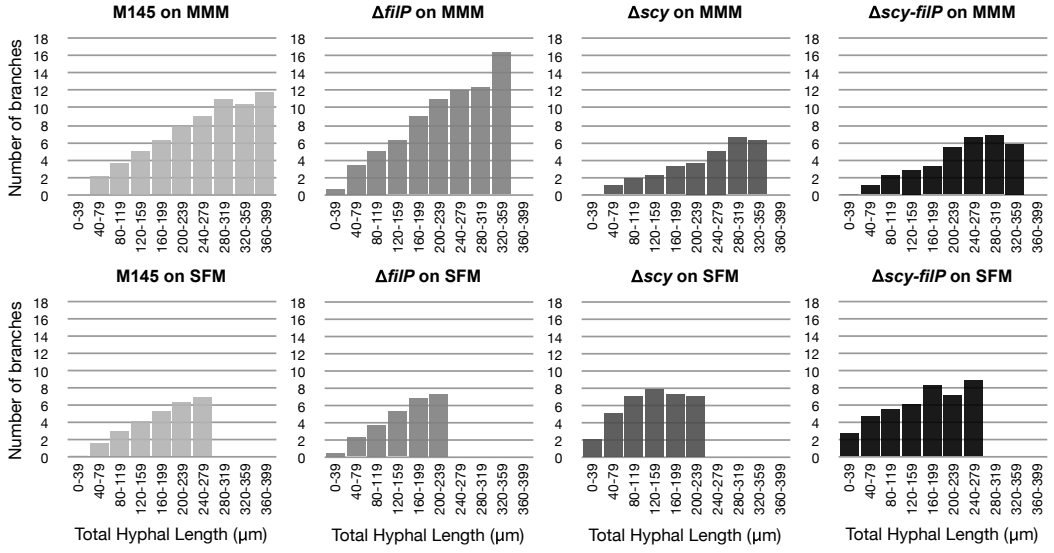

Figure D.7: Graphs of number of branches on primary filament against total hyphal length.

D.6 Tip to nearest branch

Figure D.8 shows histograms of distances from tips to their closest branch points. Table D.2 provides a numerical summary of the histogram data, providing mean values and standard error calculations.

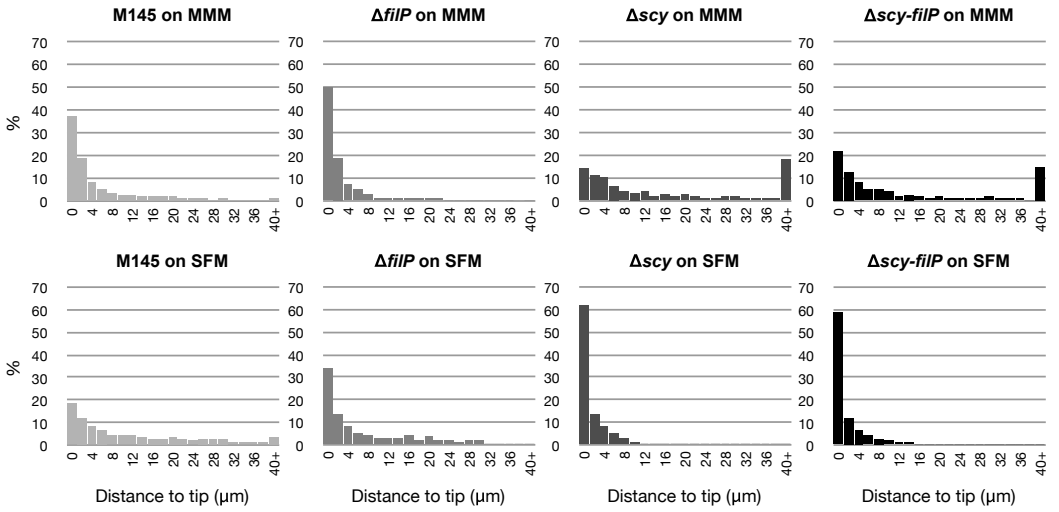

Figure D.8: Histograms of tip to nearest branch distances, with bin size 2 µm.

Bacteria	Media	Number of segments	Mean (µm)
M145	MMM	4342	7.74
M145	SFM	1189	13.38
Δ*filP*	MMM	1724	5.29
Δ*filP*	SFM	861	8.98
Δ*scy*	MMM	1502	20.22
Δ*scy*	SFM	3436	3.15
Δ*scy-filP*	MMM	746	17.30
Δ*scy-filP*	SFM	1617	4.79

Table D.2: Summary table for tip to nearest branch histogram.

Appendix E

Model fitting results

E.1 Population balance model parameter fitting

Figures E.1 to E.4 show the graphs used to fit model parameters to the experimental data.

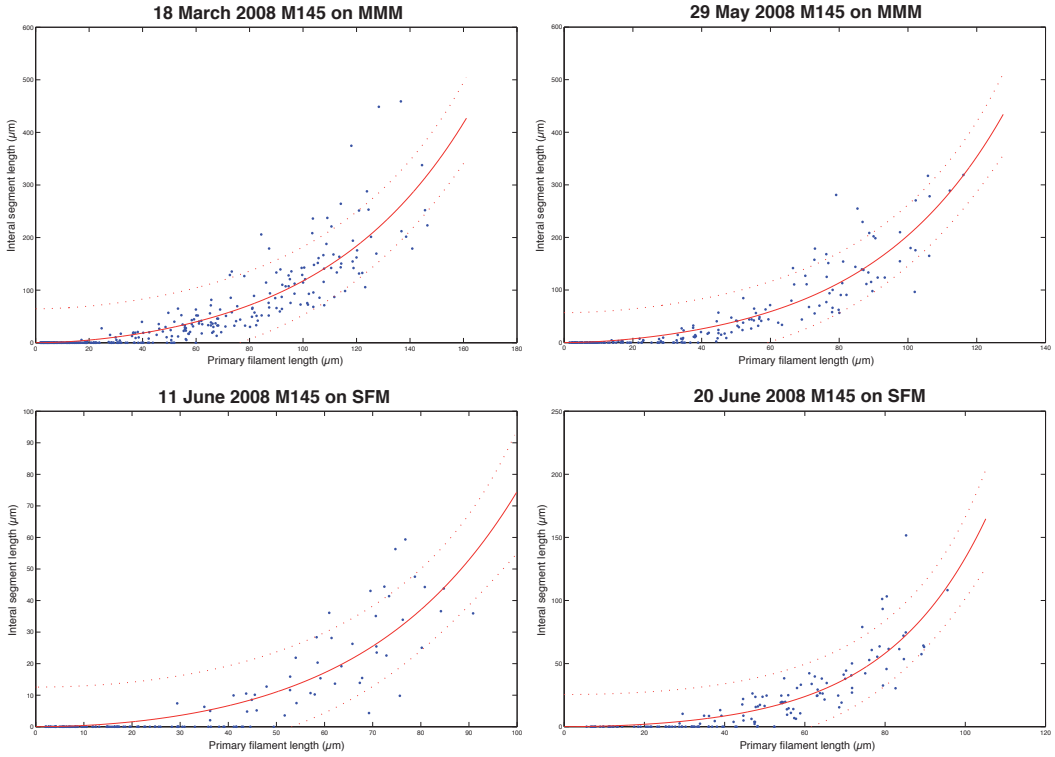

Figure E.1: Population balance model parameter fit graphs for M145 on MMM and SFM.

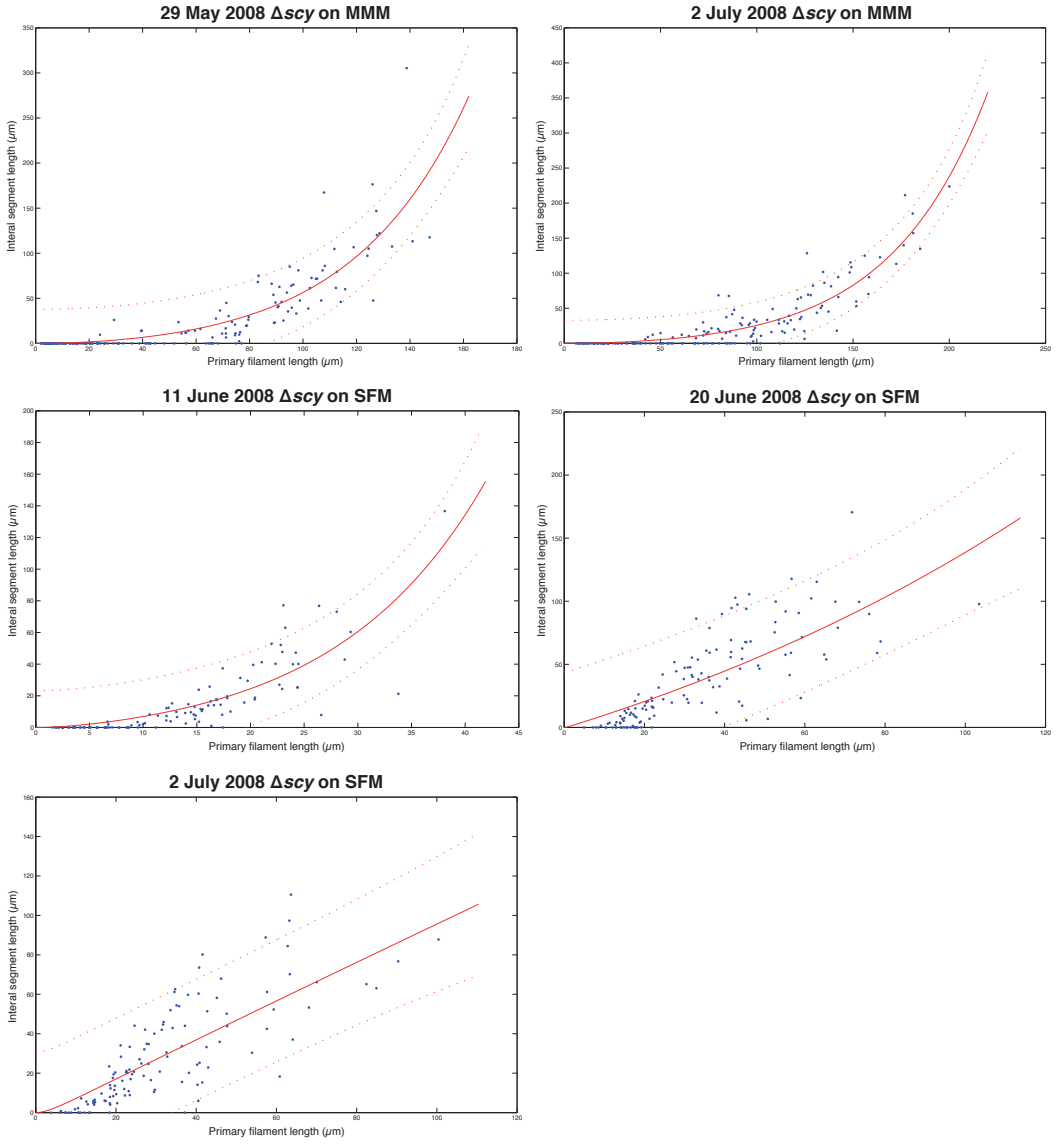

Figure E.2: Population balance model parameter fit graphs for Δ*scy* mutant on MMM and SFM.

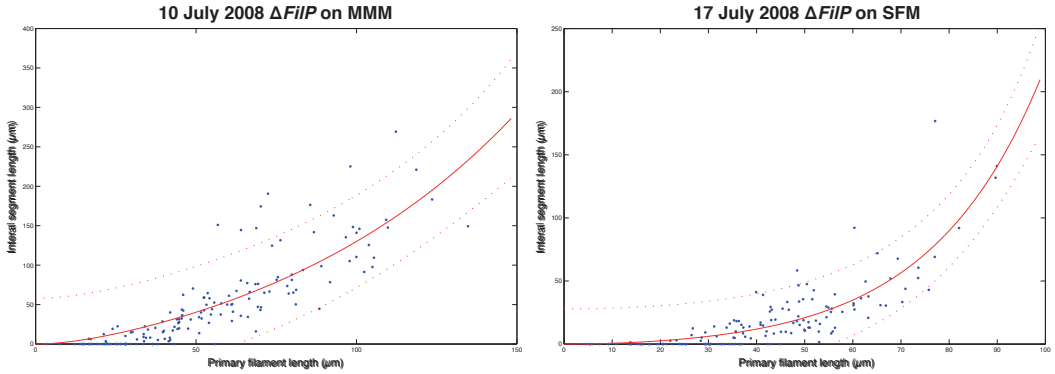

Figure E.3: Population balance model parameter fit graphs for Δ*filP* mutant on MMM and SFM.

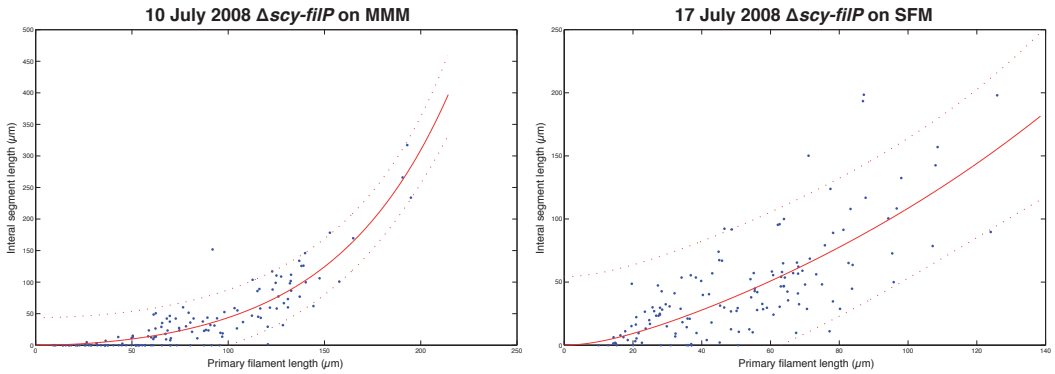

Figure E.4: Population balance model parameter fit graphs for Δ*scy-filP* mutant on MMM and SFM.